CONDUCTING POLYMER FIELD EFFECT TRANSISTORS AND GAS SENSORS

By

Purushottam Jha

(Enrolment No.: PHYS 01201004012)

Under the guidance of

Prof. D. K. Aswal

A thesis submitted to the
Board of Studies in Physical Sciences
In partial fulfillment of requirements
For the Degree of
DOCTOR OF PHILOSOPHY
of
HOMI BHABHA NATIONAL INSTITUTE

November, 2013

Homi Bhabha National Institute

Recommendations of the Viva Voce Board

As members of the Viva Voce Board, we certify that we have read the dissertation prepared by **Purushottam Jha** entitled **"Conducting polymer field effect transistors and gas sensors"** and recommend that it may be accepted as fulfilling the dissertation requirement for the Degree of Doctor of Philosophy.

Chairman: Prof. S. K. Gupta Date: 11.06.2014

Guide/Convener: Prof. D. K. Aswal Date: 11.06.2014

Member: Prof. N. K. Sahoo Date: 17.06.2014

External Member: Prof. S. S. Major Date: 11.06.2014

Aman Mahajan

External Examiner: Prof. Aman Mahajan Date: 11.06.2014

CERTIFICATE

I hereby certify that I have read this dissertation prepared under my direction and recommend that it may be accepted as fulfilling the dissertation requirement.

Date: 11. 6. 2014
Place: Mumbai

(Prof. D. K. Aswal)
(Guide)

STATEMENT BY AUTHOR

This dissertation has been submitted in partial fulfillment of requirements for an advanced degree at Homi Bhabha National Institute (HBNI) and is deposited in the Library to be made available to borrowers under rules of the HBNI. Brief quotations from this dissertation are allowable without special permission, provided that accurate acknowledgement of source is made. Requests for permission for extended quotation from or reproduction of this manuscript in whole or in part may be granted by the Competent Authority of HBNI when in his or her judgment the proposed use of the material is in the interests of scholarship. In all other instances, however, permission must be obtained from the author.

Purushottam Jha

Purushottam Jha

DECLARATION

I, hereby declare that the investigation presented in the thesis has been carried out by me. The work is original and has not been submitted earlier as a whole or in part for a degree / diploma at this or any other Institution / University.

Purushottam Jha

Purushottam Jha

Dedicated to my parents

List of Publications

[1] **P. Jha**, S. P. Koiry, V. Saxena, P. Veerender, A. K. Chauhan, D. K. Aswal, S. K. Gupta, Growth of free-Standing polypyrrole nanosheets at air/liquid interface using J-aggregate of porphyrin derivative as in-situ template, *Macromolecules*, 44 (2011) 4583-4585.

[2] **Purushottam Jha**, Niranjan S. Ramgir, Preetam K. Sharma, N. Datta, S. Kailasaganapathi, M. Kaur, S. P. Koiry, V. Saxena, A. K. Chauhan, A. K. Debnath, Ajay Singh, D. K. Aswal, S. K. Gupta, Charge transport and ammonia sensing properties of flexible polypyrrole nanosheets grown at air–liquid interface, *Materials Chemistry and Physics*, 40 (2013) 300–306.

[3] **Purushottam Jha**, Shankar P. Koiry, Vibha Saxena, Putta Veerender, Abhay Gusain, Anil K. Chauhan, Dinesh K. Aswal, Shiv K. Gupta, Incorporation of non-conjugated polymer chain in conjugated polymer matrix: A new single step strategy for free standing non-volatile polymer memory, *Organic Electronics*, 14 (2013) 2896–2901.

[4] Ajay Singh, Zakaria Salmi, Nirav Joshi, **Purushottam Jha**, Ashwini Kumar, Hélène Lecoq, Stephanie Lau, Mohamed M Chehimi, Dinesh K. Aswal, Shiv K. Gupta, Photo-induced synthesis of polypyrrole-silver nanocomposite films on N-(3-trimethoxysilylpropyl) pyrrole-modified biaxially oriented polyethylene terephthalate flexible substrates, *RSC Advances*, 3 (2013) 5506-5523.

[5] **P. Jha**, S.P. Koiry, Vibha Saxena, P. Veerender, Abhay Gusain, A. K. Chauhan, A. K. Debnath, D. K. Aswal, S. K. Gupta, Air-stability and bending properties of flexible organic field-effect transistors based on poly[N-9'-heptadecanyl-2,7-carbazole-alt-5,5-(4',7'-di-2-thienyl-2',1',3'-benzothiadiazole)], *Organic Electronics*, 14 (2013) 2635–2644.

ACKNOWLEDGEMENTS

The first and foremost, I take a highly esteemed privilege to express my deep sense of gratitude to my research guide and mentor **Prof. D. K. Aswal**, for his continuous guidance during the thesis work. I feel motivated and encouraged every time I meet him. His support and enthusiasm encouraged me to work in the field of flexible conducting polymer thin films field effect transistors and gas sensors. I owe completely to him for his enormous effort for timely submission of this dissertation. I express my deep gratitude to **Dr. S.K. Gupta,** Head, Technical Physics Division, for his encouragement and support.

I am greatly indebted to **Dr. A.K. Chauhan, Dr. Vibha Saxena and Dr. S. P. Koiry,** for their help in carrying out experiments, learning various characterization techniques, continuous support and encouragement during the course of the work. I am extremely grateful to **Dr. Ajay Singh** for photopolymerisation experiments and low temperature charge transport data analysis and **Dr. Niranjan S Ramgir** for help in gas sensing measurements. I sincerely thank **Dr. S Bhattacharya** for help in taking SEM images.

I owe my deepest gratitude to **Dr. K.P. Muthe, Dr. A. K. Debnath, Shri R. Prasad, Dr. Manmeet Kaur, Dr. S. Samanta, Dr Ranu Bhat, Mrs Ranita Basu, Mrs Niyanta Dutta, Mrs K Ganapati and Shri K.N. Meshram** for extending support and help at various stages of the thesis work. I am also thankful to **Veerender, Manoj, Preetam, Nirav, Arvind, Vishal, Abhay and Aswini** for their help during the course of the work.

Last but not least, I would like to offer my whole-hearted indebtness to my **family and friends**, who have always motivated and supported me.

Perhaps, I forgot someone… so, just in case: thank you to whomever it concerns!

Purushottam Jha

CONTENTS

SYNOPSIS

Polymers have long been used as insulating materials e.g. metal cables are coated in plastic to insulate them. Polymers, owing to their light weight and greater ease of fabrication, have replaced and are continuing to replace metals in several areas of applications. Traditional polymers, such as, polyethylene or polypropylene, are insulators because the valence electrons are bound in sp^3 hybridized covalent bonds. Such "sigma-bonding electrons" have low mobility and do not contribute to the electrical conductivity of the material. Conducting polymer is a class of polymers which are conjugated, that is, possess an extended π-conjugation along the polymer backbone (e.g. contiguous sp^2 hybridized carbon centers), and therefore, exhibit semiconducting behavior. Conducting polymers gained attention after the discovery of high conductivity in oxidized iodine-doped polyacetylene in 1977 by Alan J. Heeger, Alan MacDiarmid and Hideki Shirakawa, for which they were awarded the 2000 Nobel Prize in Chemistry. The polyacetylene though did not find practical applications, but drew the attention of scientists and encouraged the rapid growth of the field of conducting polymers in several directions, such as, synthesis of new conducting polymer compound, reproducible synthesis of conducting polymers, environmental stability, preparation of thin films, investigation of charge transport and applications. In particular, conducting polymers are promising candidates for large area and ubiquitous electronic applications, such as displays, sensor arrays and smart cards, etc. Unlike inorganic semicondcutors, conducting molecules pack up through weak van der Waals forces and π–π interactions rather than rigid covalent bonds. The weak intermolecular interaction not only makes conducting polymers potentially soluble and easy to be processed in solution, but also endows conducting polymer electronic devices the nature of flexibility. However, most conducting polymer electronic devices reported so far are fabricated on inorganic substrates, such as glass sheets and silicon wafers, which have limited the intrinsic flexibility of conducting polymers. Therefore the motivation of current thesis work is to prepare flexible conducting polymer films and study their suitability in devices, such as, gas sensors, field effect transistors and memory devices.

In order to prepare the flexible conducting polymer (polypyrrole and PCDTBT) films we have adopted two different strategies: (i) synthesis of flexible freestanding conducting polymer films by interfacial polymerization at liquid/air interface, and (b) deposition of conducting polymer films as well as nanocomposite films on flexible biaxially oriented polyethyleneteraphthalate (BOPET) substrate. We have investigated the charge transport properties of the flexible conducting polymer films by measuring the temperature dependence of resistivity and current-voltage characteristics. In addition, organic field effect transistors (OFETs) and gas sensors were fabricated and studied using the flexible polypyrrole and PCDTBT films. This thesis is organized into following six Chapters.

Chapter 1: Introduction

In this Chapter, we begin by providing a brief overview of conducting polymers, types of conducting polymers with details on the synthesis for polypyrrole and PCDTBT: the two conducting polymers investigated in this thesis. We describe the basics of charge transport mechanisms in conducting polymers. A brief summary of the various techniques employed for the preparation of conducting polymer thin films is presented. The various applications of conducting polymers are listed and, in particular, the advancements made in the area of field effect transistors and gas sensors are discussed. The Chapter is concluded by bringing out the aim of the thesis work, which is focused on the preparation of flexible PPy and PCDTBT films and their application in field effect transistors and gas sensors.

Chapter 2: Experimental techniques

In this Chapter, we describe the details of the experimental work on the preparation of the flexible PPy and PCDTBT films using interface polymerization and spin coating. Fabrication process of FET and sensors devices is described. The overview of various techniques used for the characterization of polymer films, such as, Fourier transform infrared spectroscopy (FTIR), UV-Visible Spectroscopy, Raman spectroscopy, X-ray photoelectron spectroscopy (XPS), Atomic force microscopy (AFM), Scanning electron microscopy (SEM), electrochemical characterization etc. have been presented. The details of the electrical measurements of the conducting polymer films have been described. The details of the experimental set ups used for the measurements of OFET and gas sensing characteristics are described.

Chapter 3: Freestanding polypyrrole films

In this Chapter we describe the results of freestanding polypyrrole films synthesised by interfacial polymerization i.e. at liquid/air interface. These films were investigated for their temperature dependent conductivity and applications in OFET, memory effect and gas sensors.

In particular, we present a novel strategy for the one-pot fabrication of free-standing polypyrrole nanosheets by dropping 200 µL solution, consisting of 1mM porphyrin-derivative (TPPOH) and 0.01-1M pyrrole (Py), to 0.1M aqueous $FeCl_3$ solution kept in a beaker. TPPOH/PPy bilayer is found to form spontaneously at the air/$FeCl_3$ interface, which after washing in dichloromethane yielded in free-standing PPy nanosheets. UV/Vis and FTIR studies show that TPPOH quickly forms J-aggregate films at air/$FeCl_3$ interface, which acts as in-situ template for the growth of PPy nanosheets. The charge transport in these nanosheets has been investigated, and the results show that variable range hopping is the conduction mechanism. These nanosheets have been utilized for fabrication of ammonia gas sensors and OFETs.

In addition, we describe another single step strategy for the synthesis of free-standing polypyrrole films in which non-conjugated polymer chains are incorporated as trap states during synthesis. The PPy film was synthesized by the acidic oxidation of 2,2’:5’2”-terpyrrole at the air/water interface. The free-standing PPy films show large hysteresis along with current peaks in opposite directions during current voltage characteristics. Hysteric behaviour has been utilized to show rewritable memory effect. The memory effect of these films is attributed to the conformational changes of non-conjugated polymer chains in the PPy matrix.

Chapter 4: Flexible Ag/polypyrrole nanocomposite films for gas sensors

In this chapter, we describe synthesis of polypyrrole-silver (PPy–Ag) nanocomposite films on a N-(3-trimethoxysilylpropyl)pyrrole modified biaxially oriented polyethylene terephthalate (BOPET) substrate by photopolymerisation of pyrrole using $AgNO_3$ as a photo-initiator. The films were prepared for a fixed molar concentration of pyrrole (0.5 M), varying molar concentrations of $AgNO_3$ (0.05–0.7 M) and different UV exposure times (15 min–180 min). With increasing $AgNO_3$ concentration or with increasing polymerisation time, the film morphology shows a transition from two dimensional lamellar to granular structures. The films are adherent, flexible and exhibit a maximum room temperature electrical conductivity of ~15 S cm^{-1} (for $AgNO_3$ ~ 0.5 M, 120 min of UV exposure). However, the films directly prepared on pristine BOPET show granular morphology and their conductivity value is ~0.5 S cm^{-1}. The high conductivity of PPy–Ag films is attributed to the high conjugation length, the incorporation of Ag nanoparticles between the polypyrrole chains and the ordered structure due to the templating effect of the silanised pyrrole layer, as confirmed by GIXRD, FTIR, Raman and temperature dependent conductivity measurements. The metallic state of the embedded Ag nanoparticles in the polypyrrole matrix is confirmed by XRD and XPS. The films with the least amount of Ag ($AgNO_3$ ~0.1 M) only show a reversible conductivity change in the opposite manner on exposure to ppm levels of H_2S and NH_3 gases. The mechanism has been proposed to explain these antagonistic responses for reducing gases.

Chapter 5: Flexible OFETs based on PCDTBT

In this Chapter, we demonstrate fabrication of flexible field-effect transistors (FETs) using poly[N-9'-heptadecanyl-2,7-carbazole-alt-5,5-(4',7'-di-2-thienyl-2',1',3'-benzothiadiazole)], PCDTBT, as an active channel, poly(methyl methacrylate) (PMMA) as gate dielectric and biaxially oriented polyethyleneterephthalate (BOPET) as supporting substrate. The output and transfer characteristics of the devices were measured as a function of channel length. It has been observed that various OFET parameters viz. on-off ratio (~10^5), mobility (μ~10^{-4} $cm^2V^{-1}s^{-1}$), threshold voltage (V_{th}~ -14 V), switch-on voltage (V_{so}~ -6 V), subthreshold slope (S ~7 V/decade) and trap density (Nit ~10^{12} $cm^{-2}V^{-1}$) are almost independent of the channel length, which suggested a very high uniformity of the PCDTBT active layer. These devices were highly stable under atmospheric conditions (temperature: 20-35°C and relative humidity: 70-85%), as no change in mobility was observed on a continuous exposure for 70 days. The studies on the effect of strain on mobility revealed that devices are stable up to a compressive or tensile strain of 1.2%. These results indicate that PCDTBT is a very promising active layer for the air stable and flexible FETs.

Chapter 6: Summary

In this chapter, we present a summary of the main results of the current thesis work, and highlight the future scope of the work.

LIST OF FIGURES

Figure 3.11 (a) Photographs of the evolution in colour of acid/pyrrole in dichloromethane (DCM) interface during polymerization with time. (b) The scheme of the reaction mechanism of polymerization which is a two steps process.

Figure 3.12 (a) UV-Vis spectra of aqueous phase recorded after 5 minutes and polypyrrole film after 5 days. (b) Variation of thickness as a function of concentration of HCl.

Figure 3.13 (a) Photograph of ~ 1 inch free-standing polypyrrole film. II and III are the SEM and AFM images. IV. UV-Vis spectrum of polypyrrole film showing characteristics absorption peaks. (b) Raman spectrum of the film. The inset shows the FTIR spectrum. The characteristics peaks are marked on the spectra.

Figure 3.14 (a) Water contact angle and (b) XRD spectrum of the PPy film.

Figure 3.15 (a) Electrical characterization of polypyrrole film. Left inset (top) shows the measurement setup and the right inset (bottom) shows the I-V plot measured in inert and dark environment. Arrows indicate the direction of voltage cycle. (b) Read current density measured at 6V during SET- read- RESET- read sequence.

Figure 3.16 (a) Cyclic voltammetry of polypyrrole film recorded at 0.1 $\mathrm{Vs^{-1}}$ and 0.05 $\mathrm{Vs^{-1}}$. Inset shows the I-V characteristics recorded across the film using Al bottom contact and gold as top contact and the device structure. Arrows indicate the direction of potential and voltage scans. (b) Measured and fitted Nyquist plots of imaginary impedance (Z”) vs real impedance(Z′) at 0 V. Top inset shows the equivalent circuit and bottom inset is the visualization of nonconjugated polymer chain in PPy matrix.

Figure 3.17 FTIR spectra (range 3100 to 2800 $\mathrm{cm^{-1}}$) of the PPy film at SET and RESET states. Right inset shows FTIR spectra in the range 3100 to 3500 $\mathrm{cm^{-1}}$. Left inset shows UV-Vis spectra of the film at SET and RESET states. Characteristics peaks are assigned on the spectra.

LIST OF TABLES

Chapter -1

Introduction

In this Chapter, we begin by providing a brief overview of conducting polymers, types of conducting polymers with details on the synthesis for polypyrrole and PCDTBT: the two conducting polymers investigated in this thesis. We describe the basics of charge transport mechanisms in conducting polymers. A brief summary of the various techniques employed for the preparation of conducting polymer thin films is presented. The various applications of conducting polymers are listed and, in particular, the advancements made in the area of field effect transistors and gas sensors are discussed. The Chapter is concluded by bringing out the aim of the thesis work, which is focused on the preparation of flexible PPy and PCDTBT films and their application in field effect transistors and gas sensors.

1.1 An overview of conducting polymers

Traditionally polymers are used as insulating materials in various applications, such as, coating of metal cables for insulation, electric switch boards [1]. Polymers, such as, polyethylene or polypropylene, are insulators because the valence electrons are bound in sp^3 hybridized covalent bonds. Such "sigma-bonding electrons" have low mobility and do not contribute to the electrical conductivity of the material. Polymers, owing to their light weight and greater ease of fabrication, are used in several applications, including the automotive and aerospace industries, packaging, agriculture, home appliances, office equipments, communication, electronics, electrical technology, biomedicine etc.: as often remarked “from buckets to rockets” [1, 2].

In parallel, for over a century, persistent efforts were made to induce the conductivity in the polymers, which are now known as conducting polymers. Conducting polymer is a class of polymers which are conjugated, i.e. possess an extended π-conjugation along the polymer backbone, and therefore, exhibit semiconducting behaviour. Conducting polymers have backbones of contiguous sp^2 hybridized carbon centers. One valence electron on each center resides in a p_z orbital, which is orthogonal to the other three sigma-bonds. All the p_z orbitals combine with each other to a molecule wide delocalized set of orbitals. The electrons in these delocalized orbitals have high mobility when the material is "doped" by oxidation, which removes some of these delocalized electrons. Thus, the conjugated p-orbitals form a one-dimensional electronic band, and the electrons within this band become mobile when it is partially emptied. A brief history on the evolution of conducting polymers is summarized below.

- In the mid-19th century, Henry Letheby, investigated the electrochemical and chemical oxidation products of aniline in acidic media and observed that reduced polyaniline form was colourless while oxidized forms were deep blue [3].
- The first highly-conductive organic compounds were the charge transfer complexes were reported in the 1950s, with resistivities as low as 8 ohms-cm [4].In the early 1970s, researchers demonstrated salts of tetrathiafulvalene show almost

metallic conductivity, while superconductivity was demonstrated in 1980 [5-7]. Though charge transfer salts are not polymers, conductivity in these compounds suggested that polymers can carry current.

- In 1963, Bolto, Weiss and coworkers reported resistivity of ~1 Ω-cm in derivatives of polypyrrole [8, 9]. Subsequently, DeSurville and co-workers reported high conductivity in a polyaniline, and later reported that polyaniline films serving as electrodes [10, 11].
- In 1977, Alan J. Heeger, Alan MacDiarmid and Hideki Shirakawa reported high conductivity in oxidized iodine-doped polyacetylene, for which they were awarded the 2000 Nobel Prize in Chemistry [12].

The polyacetylene though did not find practical applications, but drew the attention of scientists and encouraged the rapid growth of the field of conducting polymers. The research on conducting polymers grew in several directions, such as, synthesis of new conducting polymer compound, reproducible synthesis of conducting polymers, environmental stability, preparation of thin films, investigation of charge transport and applications [13-21].

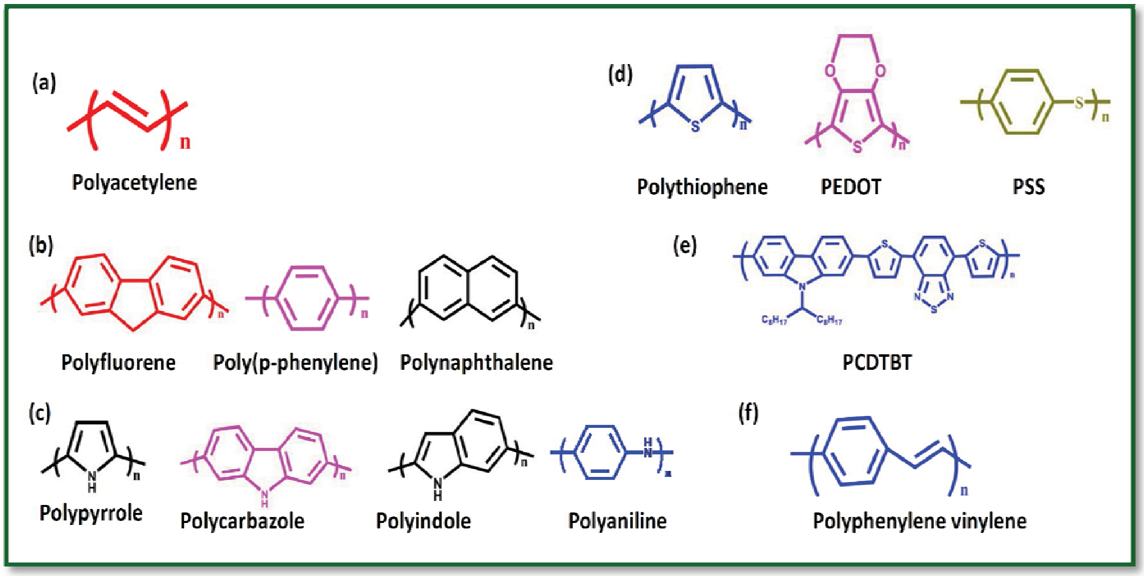

Fig. 1.1: Molecular structures of various conducting polymers.

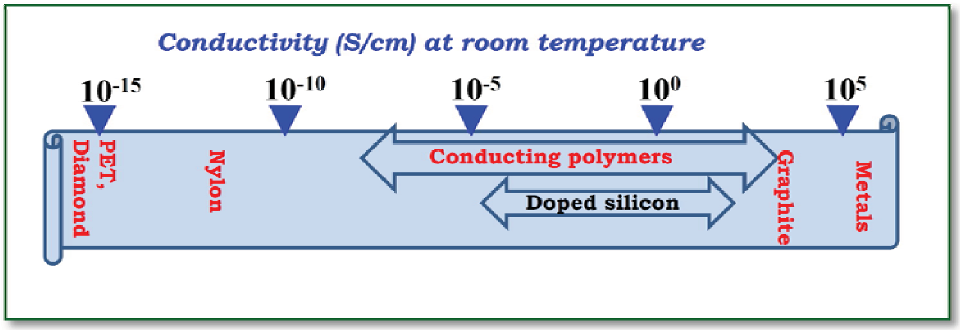

Fig.1.2: Schematic representation of the range of the condctivity of condcuting polymers upon appropriate doping. For comparisong the range of doped silicon is also shown.

1.2 Types of conducting polymers

1.2.1 Broad classification

Till date a large numbers of conducting polymers have been reported and many of them are commercially available. As of now there is not a set pattern of classifying the conducting polymers. However, depending upon the nature of conjugation in the backbone, they can be divided into following three categories (see Fig. 1):

(i) **Backbone with double bonds**: polyacetylene, see Fig. 1.1(a)

(ii) **Backbone with aromatic rings**: This category can be further divided into three parts depending upon heteroatoms present in the main chain.

  (a) *No heteroatom*: Polyfluorene; polyphenylene; polypyrene; polyazulene; polynaphthalene, see Fig. 1.1(b)

  (b) *Nitrogenheteroatom*: polypyrrole (PPy), polycarbazole (PCz), polyindole, polyazepine, polyaniline (PANI), see Fig. 1.1(c)

  (c) *Sulfurheteroatom*: poly(thiophene), poly(3,4-ethylenedioxythiophene) (PEDOT), poly(p-phenylene sulfide) (PSS), see Fig. 1.1(d)

  (d) *Both nitrogen and sulfur heteroatom*: poly[N-9'-heptadecanyl-2,7-carbazole-alt-5,5-(4',7'-di-2-thienyl-2',1',3'-benzothiadiazole) (PCDTBT) see Fig. 1.1(e).

(iii) **Aromatic cycles and double bonds**: Poly(p-phenylene vinylene) (PPV), see Fig. 1.1(f)

Due to the large number of conducting polymers available, it is not possible to describe the synthesis and physical properties of all of them. However, it may be noted the conductivity of conducting polymer can be varied in a wide range upon appropriate doping, as schematically shown in Fig. 1.2. This range is much wider than that of doped silicon.

In the following, we describe the synthesis and physical properties of the two conducting polymers namely, polypyrrole and PCDTBT, which are used in the present thesis work.

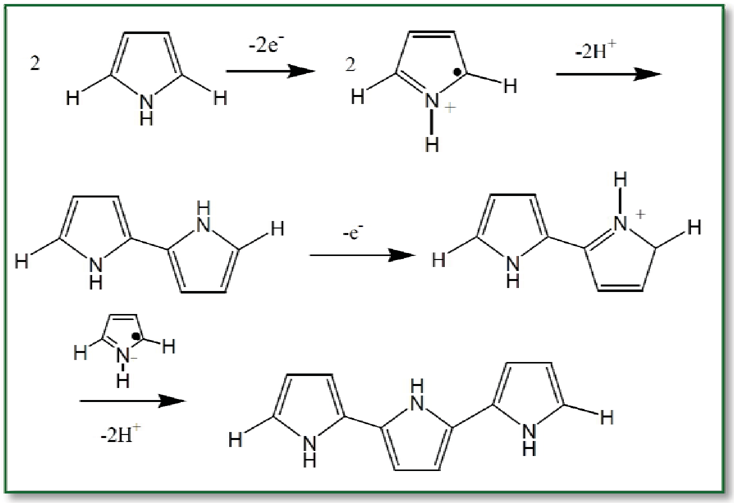

Fig. 1.3: The formation mechanism of polypyrrole from oxidized pyrrole monomers.

1.2.2 Polypyrrole

Polypyrrole (PPy) is one of the most investigated conducting polymers. PPy can be synthesized chemically or electrochemically through oxidative polymerization of pyrrole monomer (C_4H_4NH), as shown in Fig. 1.3 [22]. Oxidative polymerisation of pyrrole to polypyrrole proceeds via a one electron oxidation of pyrrole to a radical cation, which subsequently couples with another radical cation to form the 2,2'- bipyrrole. This process is then repeated to form long conjugated backbone of the PPy, as depicted in Fig. 1.4. The PPy, in the neutral state, has resonance structures that resemble the aromatic or quinoid forms, and is not conducting. PPy becomes conducting only when it is oxidized. The charge associated with the oxidized state is typically delocalized over several pyrrole units and can form a radical cation (polaron) or a dication (bipolaron). In the following we briefly describe the chemical and electrochemical synthesis of PPy.

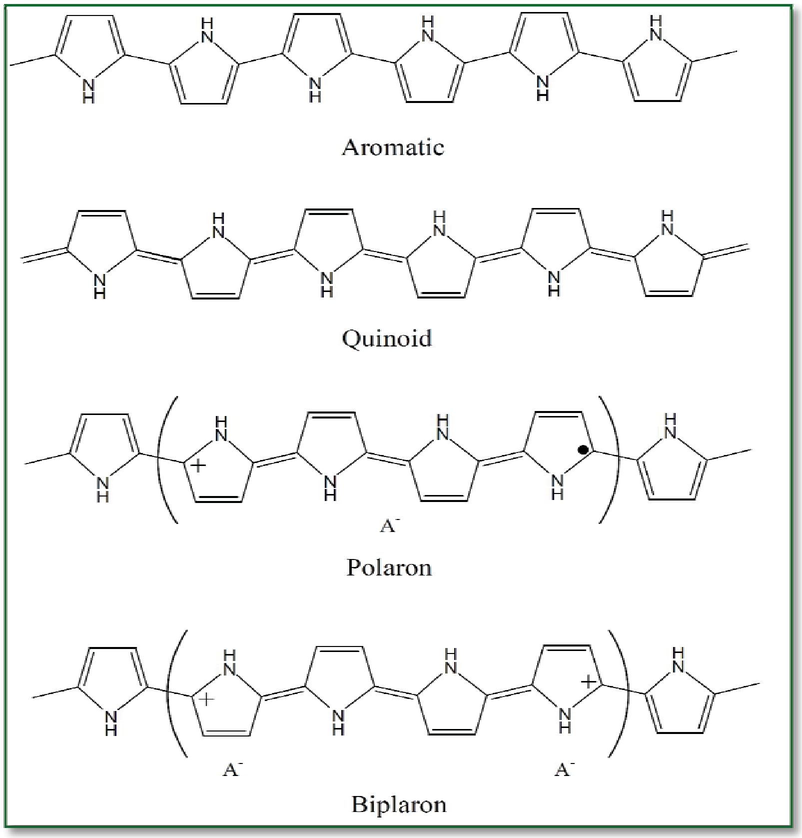

Fig. 1.4: Chemical structures of polypyrrole in neutral (aromatic and quinoid forms) and in oxidized (polaron and bipolaron forms).

The chemical synthesis of PPy is carried out via the oxidation of pyrrole with an oxidant, such as, ferric chloride, which leads to the formation of PPy powder [23]. In the case of electrochemical oxidation of pyrrole, PPy film is formed at the working electrode of the electrochemical cell. In both the case the formation mechanism of PPy is similar to that described in Fig. 1.3. Some of the literature findings on the various properties of PPy are summarized below [24-28].

(i) The PPy obtained from the chemical polymerization is usually in oxidized form, and therefore, is conducting with $FeCl_4^-$ ions acting as counter-ions.

(ii) The conductivity of PPy is related to the Fe^{2+}/Fe^{3+} redox potential. The solvent used in the reaction influences the redox potential. For example, the Fe^{2+}/Fe^{3+} redox potential is lower in water than acetonitrile. If the redox potential is too high, an irreversible dissolution of PPy can occur, as for ferric perchlorate in acetonitrile. Methanol has been found to produce the best PPy with high conductivity. The solvent also has an influence on the dopant ion that remains in the PPy e.g. in ether using $FeCl_3$ as oxidant leaves $FeCl_4^-$ as the dopant ion, while in methanol, the dopant is mainly Cl^- with some $FeCl_4^-$. In case water is present in solvents, water gets trapped in the PPy with formation of pyrrolidinone rings at chain terminations. Any ions present in solution will also get incorporated into the PPy. Dopants whose bonds are labile, such as, Cl-O, B-F, P-F, should be avoided for sake of polymer stability.

(iii) Polymerisation of pyrrole in the presence of surfactants such as dodecylbenzyl sulphonic acid or a salt like sodium dodecyl sulphate, leads to an increase in mass yield due to incorporation of the salt/surfactant into the polymer. Cationic surfactants are found to inhibit the polymerization of pyrrole. Polymerisation of pyrrole in the presence of polystyrene sulphonate (PSS) produced particles (non-colloidal) with the size being inversely proportional to the concentration of ferric chloride oxidant. The size effect is due to the affinity of pyrrole and the ferric ion to PSS. The acid concentration affects the polymerisation process.

(iv) The conductivity of PPy increases as the synthesis temperature is reduced. This is thought to be due to a reduction in the number of side reactions.

(v) PPy derivatives have been prepared and their properties studied. It has been shown that by blocking the 3,4- positions on the pyrrole ring, unwanted side reactions at these sites can be eliminated. This has been resulted in a higher conductivity, particularly in the case of poly 3,4-dimethoxypyrrole.Various alkylenedoxypyrroles have been synthesized and studied, including a series of soluble species. N-substituted pyrroles tend to induce twisting relative to adjacent pyrrole rings, thus limiting the conjugation length and conductivity.

(vi) Good solvents for electropolymerisation include water, acetonitrile, butanone, propylene carbonate, dimethylformamide (DMF) and ethanol though the presence of a bit of water (1 v/v %) enhances the polymer formation. Water can also result in chain termination. Potentiostatic, potential cycling, and galvanostatic methods can be used to electropolymerise pyrrole. Potentiostatic methods (constant potential) and cycling the potential yield the most consistent films of about the same quality. Galvanostatic deposition (constant current), does not produce as good a quality film as the other methods, but is useful for controlling film thickness. Electrochemical oxidation of a 5-member pyrrole oligomer shows two reversible one-electron oxidation processes at E_o = -0.28 and -0.08 V vs Ag/Ag^+. These correspond to the formation of the radical cation and dication, respectively, which are stable and do not polymerize. Another oxidation peak at E_p= 0.75 V marks the start of polymerization. Extrapolation of the E_o value to infinite chain length for the first one electron oxidation gives a value of –0.59 V, compared to the measured value of –0.57 V for PPy from the pentamer.

(vii) PPy has a wide range of conductivity (10^{-7} Scm^{-1} to 10^4 Scm^{-1}) depending on the extent of doping, nature of dopant and method of synthesis. The neutral (undoped) PPy is insulating with the gap of ~4 eV. The high conductivity PPy films are reported to be synthesized at low temperature. The conductivity of free-standing PPy films, synthesized by freezing interfacial polymerization method, has been reported to 2×10^3 Scm^{-1}, which is highest value reported till date. The conductivity of PPy (as well as its nanocomposites with metal oxides) as a function of temperature indicate that it can fall into metallic, critical or insulating regions of a typical Mott-insulator transition. Bipolarons appear to be the charge carriers and conductivity is linked to the loss or decomposition of the dopant ions.

(viii) Elevated temperatures in air reduce the quinoid content and oxidise the 3,4-positions. Dodecyl sulphate dopant is less stable than p-toluene sulphonate at elevated temperatures. Under argon the dodecyl sulphate doped PPy become brittle indicating cross linking at elevated temperatures.

(ix) The polymer produced by chemical synthesis is generally an intractable solid or powder. Generally PPy is insoluble in organic solvents and water. To make it soluble in organic solvents, it is doped with dopant with long alkyl chains or pyrrole is derivatised with alkyl groups prior to polymerization. For example, PPy doped with p-dodecylbenzene sulphonic acid (DBSA) is soluble in m-cresol or chloroform in the presence of excess DBSA. PPy doped with β-naphthalenesulphonic acid (NSA) or 5-n-Butylnaphthalene sulfonic acid (BNSA) is soluble in m-cresol.

(x) The colour of PPy depends on the degree of oxidation or doping. The colour of the PPy changes from yellow to the blue and, ultimately, black with the increasing doping level.

(xi) Neutral PPy is known to be very unstable in water or air. In basic solutions the PPy gets doped with hydroxide ions and other anions in acidic solutions.

(xii) Doped PPy is relatively stable in air. Thermal stability of PPy depends on dopant anion, and is stable upto 150^{o}C. Thermal decomposition is accompanied with the decomposition of dopant anion or deprotonation of pyrrole ring at higher temperatures. The thermal stability of electrochemically synthesized films can be improved by the treatment with sulphuric acid, sodium sulphate or sodium bisulphate. It has been found that these treatments do not change the morphology of PPy films.

(xiii) Generally PPy is redox active which is associated with its doping and dedoping process. Cyclic voltametry (CV) is used for study of its redox property. Doped-PPy has positive charges on its oxidized chain segments which are counterbalanced by incorporated dopant anions. During CV when PPy is reduced dopant anions leave the PPy matrix and comes in electrolyte solution and when again oxidized it gets back to PPy matrix. The oxidation and reduction gives rise to peaks in cyclic voltagram. The anodic peak in cyclic voltagram is related to the oxidation of PPy, the cathodic one, to its reduction to the neutral form. The redox potential of PPy depends on the conditions of measurements and the method of PPy synthesis.

(xiv) PPy is amorphous and usually gives a broad hump at 2θ ~23-25^{0} in XRD pattern. The electron diffraction showed that there are up 15% (of total volume) of crystalline domains in the bulk of amorphous PPy. The degree of crystallinity varies according to method of synthesis and is compared on the basis of full width at half maxima (FWHM) of the hump.

1.2.3 PCDTBT

Poly[N-9'-heptadecanyl-2,7-carbazole-alt-5,5-(4',7'-di-2-thienyl-2',1',3'-benzothiadiazole)], known as PCDTBT is new donor polymer material and has the molecular formula of $(C_{43}H_{47}N_3S_3)nC_{12}H_{10}$. Its structure is shown in Fig. 1.1 (e). PCDTBT has been synthesized by Leclerc and coworkers via copolymerization of the monomers 2,7-bis(4’,4’,5’,5’-tetramethyl-1’,3’,2’- dioxaborolan-2’-yl)-N-9”-hepta-decanylcarbazole and 4,7-di(2- bromothien-5-yl)-2,1,3-benzothiadiazole, as shown in Fig. 1.5 [14, 29].

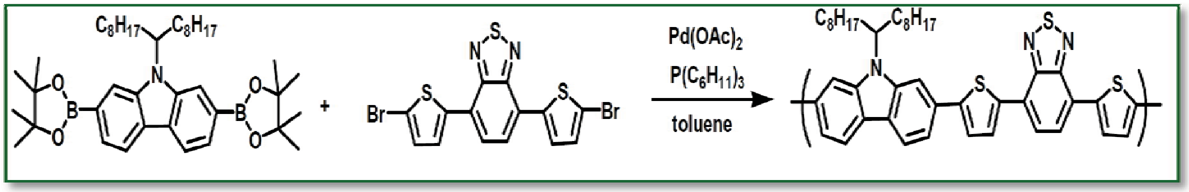

Fig. 1.5: The chemical reaction for the synthesis of PCDTBT.

Some of the salient features of the PCDTBT are:

(i) PCDTBT is a donar-acceptor copolymer having N-9-heptadecanylcarbazole as donar unit and 4,7-di-2-thienyl-2,1,3-benzothiadiazole (DTBT) as acceptor unit. It has highest occupied molecular orbital (HOMO) and lowest unoccupied molecular orbital (LUMO) levels at ~-5.4eV and -3.6eV, respectively. The low energy band gap (1.8 eV) and the location of HOMO/LUMO levels makes it a very suitable candidate for donor in bulk heterojunction solar cells [29, 30].

(ii) PCDTBT is soluble in chloroform, dichlorobenzene and toluene, which depends on the molecular weight. The high solubility makes PCDTBT suitable for making its thin films by spin coating, and therefore, is suitable for several applications [31, 32].

(iii) PCDTBT has very good air stability. It is stable upto a temperature of 150^oC in air and upto 350^oC in nitrogen atmosphere. The glass transition temperature (T_g) of PCDTBT is 130^oC [32].

(iv) PCDTBT films are amorphous in nature even after annealing at high temperatures [32].

1.3 Charge transport in conducting polymers

As shown in Fig. 1.4, the PPy can be neutral and in the oxidized forms can have polaron and bipolaon in the backbone chain. One of the early explanations of conduction in conducting polymers was based on the band theory [33, 34]. According to this, half-filled valence band would be formed from a continuous delocalized π-system, which would be an ideal condition for conduction of electricity. However, it turned out to be that polymer can lower its energy by bond alteration (alternating short and long bonds), which introduces an energy gap of ~1.5 eV, making it a high energy gap semiconductor, as shown in Fig. 1.6. The polymer therefore can be transformed into a conductor by doping it with either an electron donor or acceptor. This is analogous to the doping of silicon with either arsenic or boron. However, while the doping of silicon produces a donor energy level close to the conduction band or an acceptor level close to the valence band, this is not the case with conducting polymers.

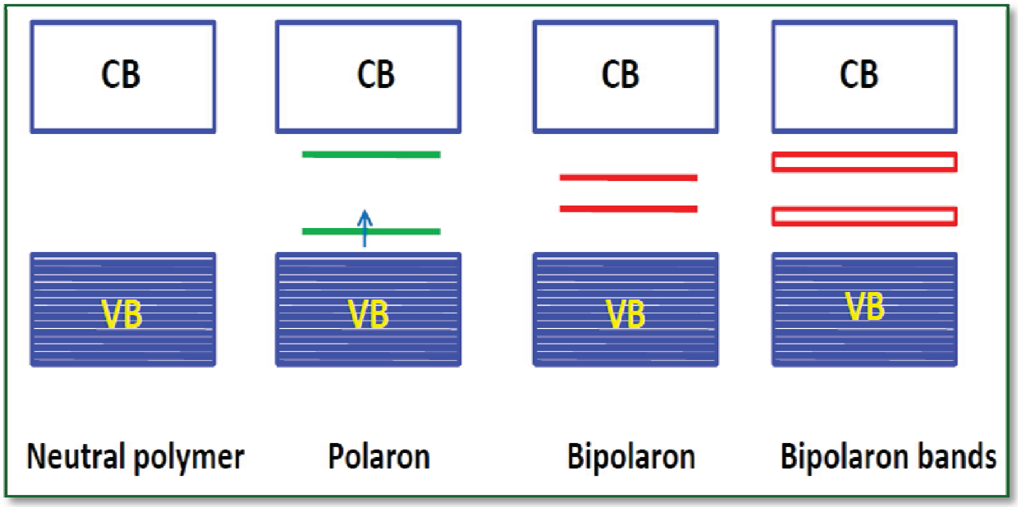

Fig. 1.6: The band structure of the neutral polymer and the polaron and bipolaron states in the oxidized state.

The oxidative doping of PPy proceeds in the following way. An electron is removed from the π-system of the backbone producing free radical and a spinless positive charge. The radical and cation are coupled to each other via local resonance of the charge and the radical. The distortion produced by this is of higher energy than the remaining portion of the chain. The creation and separation of these defects costs a considerable amount of energy. This limits the number of quinoid-like rings that can link these two bound species together. In the case of polypyrrole it is believed that the lattice distortion extends over four pyrrole rings. This combination of a charge site and a radical is called a polaron, which creates a new localized electronic state in the gap, with the lower energy states being occupied by a single unpaired electron. The polaron states of PPy are symmetrically located about 0.5 eV from the band edges, see Fig. 1.6. Upon further oxidation the free radical of the polaron is removed, creating a new spinless defect called a bipolaron, which has lower energy than the creation of two distinct polarons. At higher doping levels it becomes possible that two polarons combine to form a bipolaron. Thus at higher doping levels the polarons are replaced with bipolarons. The bipolarons are located symmetrically with a band gap of 0.75 eV for PPy, see Fig. 1.6. This eventually, with continued doping, forms into a continuous bipolaron bands. Their band gap also increases as newly formed bipolarons are made at the expense of the band edges. For a very heavily doped polymer it is conceivable that the upper and the lower bipolaron bands will merge with the conduction and the valence bands respectively to produce partially filled bands and metallic like conductivity.

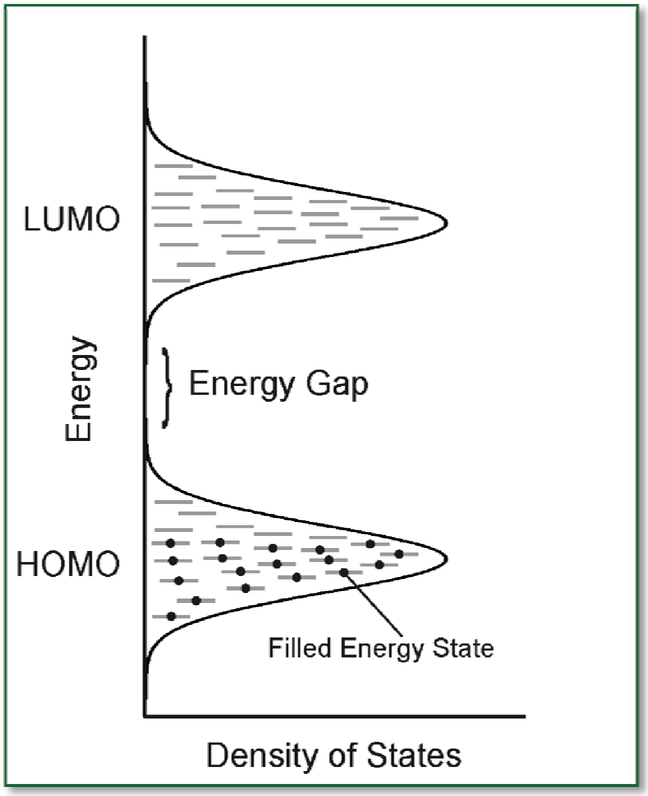

Fig. 1.7: Schematic representation of the energy levels of the highest occupied molecular orbital (HOMO) and the lowest unoccupied molecular orbital (LUMO) in an organic semiconductor. The levels are not well defined, but form a Gaussian distribution of localized states.

Although solitons, polaron and bipolarons are known to be the main source of charge carriers, the precise conduction mechanism in conducting polymers is not yet fully understood. The problem lies in attempting to trace the path of the charge carriers through the polymer. All of conducting polymers are highly disordered, which contains a mixture of crystalline and amorphous regions. In addition, it is necessary to consider the transport along and between the polymer chains as well as the complex boundaries established by the multiple numbers of phases. In particular, the kinks and twists of the polymer chains and chemical defects the conjugation is often broken, resulting in conjugated segments of different lengths [35]. Because of the variation in the conjugation length and the interaction energies, a semiconducting polymer cannot have well defined energy bands, as shown in Fig. 1.6. Instead a charge carrier, electron or hole, will be localized within conjugated segments with varying energy levels. The distribution of the energy levels is usually approximated by a Gaussian function, as shown in Fig. 1.7.

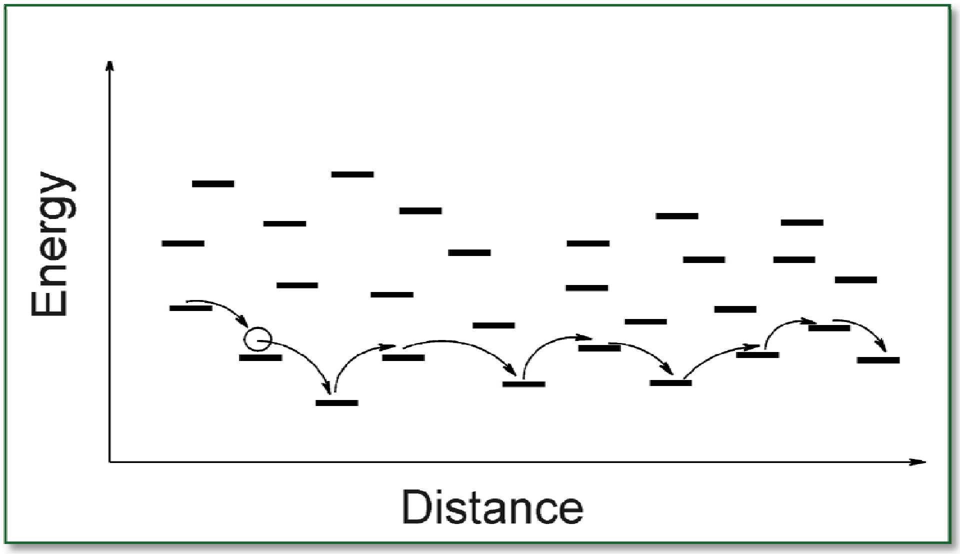

Fig. 1.8: Schematic depicting the localized energy levels versus distance. In hopping transport the charge carrier is localized due to disorder, defects or self-localization and hops from site to site with the essential help of lattice vibrations (phonons). The mobility of the carriers for this type of transport increases with the increase of temperature and increase of charge carrier density.

The main conduction mechanism through conjugated polymers is hopping transport, that is, phonon-assisted tunneling of a charge carrier from an occupied localized state to a nearby unoccupied localized state[16]. This is schematically represented in Fig. 1.8. The transition rate (W_{ij}) from an occupied localized state i with an energy ε_i to an unoccupied state j with an energy ε_j is described by Miller and Abrams, assuming a single-phonon jump from site to site and a low rate of doping [36]:

$$W_{ij} = \nu_0 \exp(-2\gamma R_{ij}) \begin{cases} \exp\left(\dfrac{\varepsilon_j - \varepsilon_i}{k_B T}\right) & \varepsilon_i < \varepsilon_j \\ 1 & \varepsilon_i \geq \varepsilon_j \end{cases}$$

where υ_0 is the attempt-to-jump rate, γ is the inverse localization length, T is absolute temperature, k_B the Boltzmann constant and R_{ij} is the distance between states i and j. The tunneling probability between each state is determined by the first exponential term and depends on the spatial distance between the two states. The second exponential term describes the temperature dependence of the tunneling rate when an energy barrier is present for the tunneling jump, equal to ε_j- ε_i, if $\varepsilon_j>\varepsilon_i$. When this model is applied to polymer semiconductors it is assumed that the conjugated segments play the role of nearly isolated localized states. Hence, unlike in band transport, where the charge carriers are scattered by the phonons present in the system, in hopping transport phonons aid the charge carriers to overcome the energetic barriers between different sites. This is clearly observed in the decrease in charge carrier mobility with decreasing temperature. The hopping model by Miller and Abrams was further extended into the 'variable range hopping' (VRH) model, which assumes that the localized states are spread over the entire energy gap. In order to investigate the nature of conduction mechanism, the conductivity of the polymer as a function of level of doping, temperature, magnetic field and the frequency of the current have been studied [37, 38]. The majority of data show that movement of charge carriers takes place by thermally activated hopping or VRH.

1.4 Conducting polymer thin films: preparation methods

Conducting polymers in the form of thin films are essential for investigating the physical properties and using them for various applications. Thin films of conducting polymers can be prepared by different methods, which are briefly discussed below [39].

(a) Electrochemical deposition

Electrochemical deposition is the most convenient method to deposit conducting polymer films on the conducting substrates using a electrochemical cell [40, 41]. In this case, the thickness of the film can be controlled by the total charge passed through the electrochemical cell during film growing process.

(b) Dip-coating

In this case, the substrate is dipped into a chemical polymerization solution, whereby part of the polymer gets deposited onto its surface. The thickness of the film is usually controlled by dipping time. Another similar process involves alternatively immersing a substrate into the monomer and oxidant solutions. The adsorbed monomer will be polymerized on the surface of substrate.

(c) Spin-coating

Spin-coating is a simple method for preparing films from soluble conducting polymers. In this process, the conducting polymer solution is spread on a rotating substrate. After evaporation of solvent, a thin film was formed. Repeating above process is feasible, which can control the thickness of the film. Concentration of the solution and rotating rate of the substrate play important roles in adjusting the thickness of the formed film. This method can coat conducting polymers on both conducting and insulating substrates.

(d) Langmuir-Blodgett (LB) technique

LB technique is a popular method to produce monolayer and thin film of conducting polymer. The operation of LB technique is based on lifting the Langmuir film produced at the liquid/air interface formed after the compression, and its details can be found elsewhere [42, 43].

(e)Thermal evaporation

This technology can be realized by heating conducting polymer under vacuum, and the evaporated conducting polymer deposits on the target substrate. The thickness of the film is determined by the evaporation duration.

(f) Vapor deposition polymerization

This technology consists of two steps: prepare an oxidant film and then place the film into monomer vapour. The monomer diffuses into the film and polymerized on it. This technique is useful not only in preparing a pure conducting polymer film, but also in coating composite films of different conducting polymers.

(g) Drop-coating

A polymer solution is drop dried or some drops of the monomer and oxidant solutions are dropped and reacted on a substrate. This method is rather simple, however the resulting film is usually not uniform.

(h) Inkjet printing

In this method, a conducting polymer solution is dispelled from a micrometre-scale nozzle onto the substrate through the use of a printer. In this method, processing parameters such as the viscosity of solution, the boiling point of the solvent, inkjet latency time and deposition temperature all play a significant role in determining the quality of film[44].

(h) Interfacial polymerization

In the technique of interfacial polymerization, two reactive monomers are dissolved separately in immiscible liquids, which are then stacked in a beaker. A rapid reaction occurs only at the interface between these two solutions, creating a thin polymer film. For example, in the case of ferric chloride and pyrrole, a PPy film is created [45]. As the polymerization reaction proceeds, the interfacial film becomes a barrier that slows further reaction; hence interfacial polymer films can be exquisitely thin (10 - 100 nm). This method though simple, has not been widely used.

1.5 Applications of conducting polymers

As mentioned in the previous section, one of the biggest advantages of conjugated polymers is that they can be processed from solution at low temperatures. High throughput processing techniques such as spin-coating or roll-to-roll printing are easy and inexpensive ways of device fabrication, in contrast to the more complicated and expensive evaporation methods for inorganic materials. Literature suggests that conducting polymers are rapidly gaining attraction in new applications owing to improved electrical and physical properties and lower costs [1, 15, 17, 19]. Some of the promising applications are listed below:

- organic field effect transistors
- organic light emitting transistors
- organic light-emitting diodes
- printed electronic circuits
- organic solar cells
- radio-frequency identification (RFID) tag
- actuators
- electrochromism
- supercapacitors
- chemical sensors and biosensors

- flexible transparent displays
- electromagnetic shielding
- replacement for the popular transparent conductor indium tin oxide
- microwave-absorbent coatings, particularly radar-absorptive coatings on stealth aircraft

In this Chapter, we do not attempt to discuss all the above mentioned applications. Among the various conducting polymer shown in Fig. 1.1, PEDOT and polyaniline have gained some large scale applications. PEDOT is mainly used in antistatic applications and as a transparent conductive layer in form of PEDOT:PSS dispersions (PSS=polystyrene sulfonate). PANI is widely used for printed circuit board manufacturing – in the final finish, for protecting copper from corrosion and preventing its solderability. In addition, the electroluminescence - a property in which light emission is observed when a voltage is applied to a thin layer of a conductive polymer film – is being used to generate lights at low voltages and this property has led to the development of flat panel displays using organic light emitting diodes. Despite of the many commercial applications as mentioned above, the progress in the conducting polymer based other devices have been slow. The limiting factors for this are: (i) requirement of oxidative doping, which often diminishes their solubility in organic solvents and water, and hence, their processability; (ii) the charged organic backbone is often unstable towards atmospheric moisture and oxygen.

In the following we describe the literature survey on conducting polymer field effect transistors and gas sensors, which are the key targets of this work.

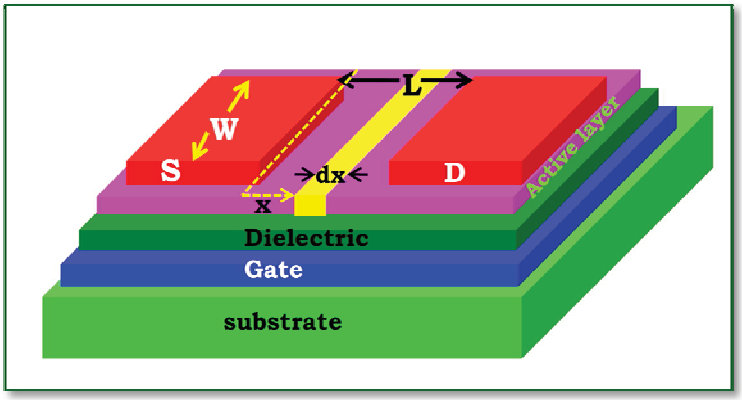

Fig. 1.9: Schematic depiction of a typical field effect transistor. The active layer (inorganic semiconductor or conducting polymer) is separated by gate electrode through an insulator. In this device, the current between Source (S) and Drain (D) is modulated by varying the gate voltage.

1.5.1 Organic field effect transistors

(a) Basic principle of organic field effect transistor

The idea of a field-effect transistor (FET) was first conceived in 1930 and further developed by Shockley and Pearson in 1948. However, the first practical applications began only in 1960. The most widely used FET is the metal-insulator-semiconductor FET (MIS-FET), in which the gate electrode is electrically insulated from the conducting channel by an insulating layer, as schematically shown in Fig. 1.9. The most typically used configuration is the metal-oxide-semiconductor FET (MOSFET) in which the silicon oxide is used as insulator. The fundamental function of the FET is the modulation of the current flow between the source (S) and the drain (D) electrodes, by applying a bias to the gate electrode.

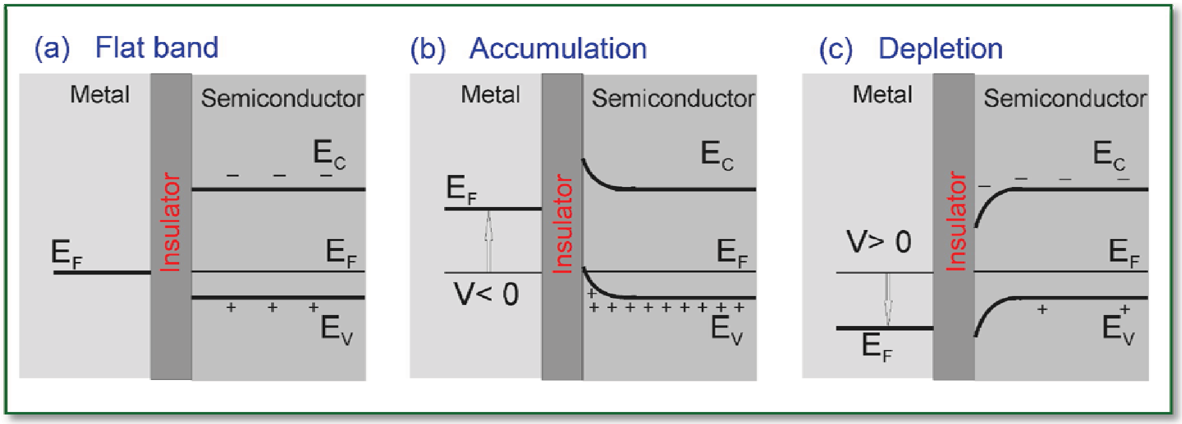

Fig. 1.10: Ideal energy band diagram at the metal-insulator-semiconductor interfaces of an FET. The figure depicts three situations for a p-type semiconductor: (a) The flat-band condition, with no applied bias, hence no band-bending. (b) Accumulation regime where a negative bias is applied on the gate causing the bands of the semiconductor to bend 'upwards' which causes accumulation of holes at the semiconductor-insulator interface. (c) Depletion regime where a positive bias is applied to the gate, which causes a depletion of holes in the semiconductor.

By varying the voltage on the gate electrode, accumulation or depletion of charge carriers can be induced in the semiconductor layer close to the semiconductor/insulator interface. In order to understand the operation of MIS-FET operates, it is important to understand on what happens at the semiconductor-insulator interface when different biases are applied to gate electrode with respect to a ground. Here we will discuss the case for a p-type semiconductor, as both of the conjugated polymers (PPy and PCDTBT) investigated in this thesis are of p- type. Depending upon the bias following three cases can arise

(i) *Flat band condition*: When the bias on the gate electrode (V_{GS}) is equal to the flat-band bias (V_{FB}). In this case there is no band bending and the Fermi levels of the semiconductor and the gate electrode are aligned. The only charge carriers present in the semiconductor are the carriers that occur by 'natural' means, such, as thermal excitation or doping, as shown in Fig. 1.10 (a).

(ii) *Accumulation region*: when a negative bias is applied on the gate electrode (more negative than V_{FB}), then its Fermi energy level will be raised. Consequently, the bands of the semiconductor will bend upwards in energy causing an accumulation of positive charges in the valence band at the interface to compensate for the negative charges on the gate, see Fig. 1.10 (b). In this regime the accumulation of charges present at the interface with the insulator (the S/I-interface) forms a channel between the source and drain electrodes, allowing a hole current to flow between them.

(iii) *Depletion region*: when a positive bias (more positive of V_{FB}) is applied to the gate electrode, see Fig. 1.10 (c), which causes lowering of its Fermi level. In this case the bands of the semiconductor will bend downwards causing a depletion of positive charges in the valence band and a slight accumulation of negative charges in the conduction band. In this regime there will be a very low charge density, hence the current between the source- and the drain electrodes will be very low, usually several orders of magnitude lower than of accumulation region. However, when a higher positive voltage is applied, the bands of semiconductor will bend further downward, which results in induction of excess negative carriers (electrons)at semiconductor-insulator interface i.e. the minority carriers are larger than majority carriers and this case is known as *inversion region*.

Unlike in the inorganic semiconductors, an inversion regime does not occur in OFETs. There are two main reasons: (i) injection of minority carriers (electrons in the case of p-type semiconductor) is blocked due to the large injection barrier present at the source electrode; and (ii) the minority carriers present in the organic semiconductor are not mobile due to the trapping in the material.

(b) Types of OFET structures

As described in Fig. 1.9, the organic field effect transistor consists of following components: a thin active layer (conducting polymer), which is separated from a gate electrode by the insulating gate dielectric (oxides or polymers); source and drain electrodes (Au, Al or Ag) of width W (channel width) separated by a distance L (channel length) that are in contact with the active layer. Most of the reported devices are fabricated on rigid surface e.g. silicon or glass. The characteristics of the CP-FETs depend not only on the morphologies of the active and gate dielectric and nature of metallic electrodes, but also on the type of device structures employed.

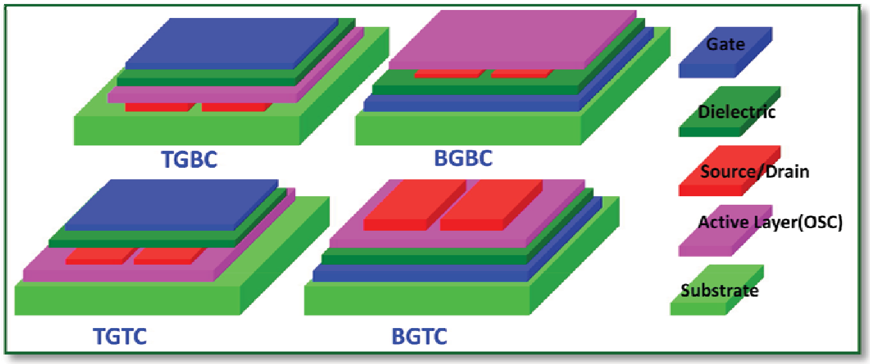

Fig. 1.11: Different types of geometries employed for the fabrication of conducting polymer FETs. TGBC: top gate bottom contact; BGBC: bottom gate bottom contact; TGTC: top gate top contact; BGTC: bottom gate top contact.

In literature, four types of device structures for CP-FETs, as shown in Fig. 1.11, are employed: (i) top gate bottom contact (TGBC), (ii) top gate top contact (TGTC), (ii) bottom gate bottom contact (BGBC) and (iv) bottom gate top contact (BGTC) structures. Each of these device structures has certain advantages and disadvantages[21, 46, 47]. One of the major differences between these device geometries arises from the position of the injecting electrodes in relation to the gatebecause of the presence of an energy barrier between the organic semiconductor and the source and drain contacts. Experiments and simulations have shown that for the same energy barrier height, OFETs with a staggered structure (BGTC, TGBC) have the advantage of being less affected by this energy barrier than OFETs with a coplanar structure (BGBC,TGTC). However, in case of the BGBC, the effect of the energy barrier on the carrier exchange efficiency can be substantially reduced by modifying the surface of the source and drain contacts with a thin organic monolayer carrying an appropriate dipole moment or with a thin metal oxide. Other differences between transistor structures arise from the dielectric/semiconductor and electrode/semiconductor interfaces, such as different morphologies at the top and bottom surfaces of a semiconductor film (molecular orientation, roughness) or introduction of trap states during metal evaporation on organic semiconductors for top contact transistors. An important advantage of the BGBC structure is that the gate dielectric layer and the source and drain contacts are prepared before the organic semiconductor is deposited. The reason why this is important is that many high mobility organic semiconductors, especially vacuum-deposited small-molecule materials, but also many high-mobility polymers, adopt a thin-film microstructure that is very sensitive to external perturbations. For example, vacuum-deposited pentacene films undergo an irreversible phase transition, associated with a substantial drop in carrier mobility, when exposed to organic solvents, such as those employed for the solution-based deposition of polymer gate dielectrics and in photolithographic contact patterning processes. With the BGBC structure, methods involving solvents and/or thermal treatments can be safely employed to prepare the gate dielectric and the contacts without harming the semiconductor layer.

(c) Literature review of CP-FET

Conducting polymers are promising materials for organic field effect transistors due to their excellent solution processibilty on large area substrates, and tunnablity of electronic properties. Since the first FET made of conducting polymers there is huge progress towards the enhancement of CP-FET characteristics, in particularly those fabricated on the rigid substrate. The main results are summarized in Table 1.1. The mobility value has been increased by 6 orders of magnitude from $10^{-5}cm^2V^{-1}s^{-1}$ to $10cm^2V^{-1}s^{-1}$ in last 3 decades for CP-FETs. Among various CPs thiophene is the most promising building blocks for polymer semiconductors. Though the first conducting polymers based field effect transistors was fabricated by Ebisawa et al in 1983 utilizing the undoped polyacetylene with a very low transconductance of $13n\Omega^{-1}$ [48], there was no progress on

Table 1.1 : Summary of literature on CP-FET on rigid substrates

CP	**Dielectric**	**Substrate**	**Geometry**	**On-off ratio**	**Mobility ($cm^2V^{-1}s^{-1}$)**	**Ref.**
Polythiophene	SiO_2	Si	BGBC	10^2-10^3	μ_h :10^{-5}	[49]
P3HT	SiO_2	Si	BGBC	—	μ_h :10^{-5} —10^{-4}	[50]
Polythiophene	SiO_2	Si	BGBC	10^5	μ_h :$2×10^{-4}$	[51]
P3HT	SiO_2	Si	BGBC	10^3	μ_h : 0.045	[52]
P3HT	SiO_2	Si	BGTC	10^6	μ_h : 0.05—0.1	[19]
P3HT	SiO_2-HMDS	Si	BGBC	~10^5	μ_h : 0.3	[53]
PQT-12	SiO_2-OTS	Si	BGTC	10^7	μ_h : 0.14	[54]
PBTTT- C12/C13/C14	SiO_2-OTS	Si	BGBC	10^6-10^7	μ_h : 0.3—0.72	[55]
PBTTT-C-14	SiO_2-OTS	Si	BGBC	—	μ_h :1	[56]
PCDT-BTZ	SiO_2-HMDS	Si	BGBC	10^5-10^6	μ_h :3.3	[57]
PCDTPT	SiO_2-DTCS	Si	BGBC	~10^5	μ_h :6.7	[58]
PDVT-10	SiO_2-OTS	Si	BGBC	10^5-10^7	μ_h : 4—8.2	[59]
DPP-DTT based polymer	(i)SiO_2-OTS /ODTS (ii) PAN-PMSQ-ODTS	(i)Si (ii) PET	(i)BGTC/BGBC (ii)BGBC	(i) 10^5-10^8 (ii) 10^5-10^7	(i)μ_h:1.5—10.5 (ii) μ_h:1.7—5.3	[60]
PDPP-FBF	SiO_2-OTS	Si	BGTC	10^3	μ_h : 0.23 μ_e : 0.56	[61]
PTDPPSe-Si	SiO_2-OTS	Si	BGTC	10^4-10^6 10-10^4	μ_h : 0.59–3.97 μ_e : 0.05–2.20	[62]
PTDPPSe	SiO_2-OTS	Si	BGTC	10^4-10^6 10^2-10^4	μ_h : 0.05–2.53 μ_e :0.006–0.43	[62]
PCDTBT	SiO_2-PPcB	Si	BGTC	~10^2–10^3 ~10^2	μ_h : 0.003 μ_e : 0.0058	[31]
PCDTBT	SiO_2-OTS	Si	BGTC	10^6	μ_h :0.02—0.03	[32]

PAc based FETs. The first FET based on polythiophene (PTh) was fabricated by Tsumura et al using electrochemically synthesized PTh [49]. These devices shows very low mobility of $1\times10^{-5}cm^2V^{-1}s^{-1}$ and PTh was insoluble in organic solvents. For large area processing CPs soluble in organic solvents was required. By attaching alkyl chain solution processable poly(3-hexylthiophene) (P3HT) has been synthesized and in 1988 Assadi et al have fabricated OFET by spin coating of poly(3-hexylthiophene) (P3HT) on Si/SiO_2[50]. However, the carrier mobility for these devices were also found to be low i.e. 10^{-5}-10^{-4} $cm^2V^{-1}s^{-1}$.

Thereafter P3HT based OFETs were extensively studied by many research groups and it was found that the mobility can be increased by using regioregular P3HT to 0.1 $cm^2V^{-1}s^{-1}$ [19]. The increase in mobility has been attributed to improvement in molecular ordering. Further studies on modification of dielectric-active layer interface and selection of proper device geometry leads to enhancement of mobility to $0.3cm^2V^{-1}s^{-1}$ for P3HT-FET[53]. The stability of these devices in ambient atmosphere was found to be very poor which limits its application. But the fundamental understanding on P3HT-OFETs has contributed in understanding of the charge transport mechanism and design of CPs with high nobilities and air-stability. To address low mobility and poor air-stability problems associated with P3HT, new polythiophenes were developed by Ong et al. (PQTs) and McCulloch et al (PBTTTs) [54, 55]. These CPs based OFETs showed quite high hole motilities of 0.14 $cm^2V^{-1}s^{-1}$ and 0.3–0.72 $cm^2V^{-1}s^{-1}$, respectively. Chabinyc et al. investigated the effects of humidity on PQT FETs and found the poor stability of in ambient atmosphere [63].Then, Hamadani et al reported increased hole mobility of 1 $cm^2V^{-1}s^{-1}$ for PBTTT-C14 by employing Pt instead of the commonly used Au as the contacting electrode which results in significant reduction in the metal/polymer contact resistance [56]. Apart from these polymers other CPs such has PTAA, F8BT, etc has also been studied [17, 21].

The revolution in this area has come with the donor-acceptor based copolymers (D-A copolymers) in which monomer units contain donor and acceptor groups. A ground-state partial charge-transfer state may be created in conjugated alternating D-A polymer which would help in charge injection at the electrode/active layer interface. It also assists in charge carrier transport in active layer which leads to increase in mobility. A field effect mobility of 3.3cm^{2}V^{-1}s^{-1} has been achieved by Tsao et al for PCDT-BTZ which is a D-A copolymer [57]. This is higher mobility than the amorphous Si (μ~1 cm^{2}V^{-1}s^{-1}). A much higher hole mobility (6.7 cm^{2}V^{-1}s^{-1}) was demonstrated for regioregular PCDTPT by Tseng et al [58]. They have found that rr-PCDTPT shows anisotropic charge transport and higher mobility (~ 6 times) in parallel direction to the polymer backbone than perpendicular direction. Further enhancement of mobility to 8.2 cm^{2}V^{-1}s^{-1} by Chen et al was obtained in new D-A CP (PDVTs) with diketopyrrolopyrrole moieties (DPP) as acceptor unit [59]. The formation of hydrogen bonds between oxygen atoms in the DPP units and β - hydrogen atoms of the neighbouring thiophene in the polymer backbone enhance co-planarity of the main chain, resulting in strong intermolecular π–π stacking. Also environmental stability under 20% air humidity has been studied and it was found that the mobility decreased about 33% in the first 7 days and there were negligible changes in the subsequent 100 days. Recently, for CP-FET hole mobility of an order of magnitude higher than amorphous silicon been reported by Li et al [60]. They have designed and synthesized a very high molecular-weight conjugated alternating D-A polymer with dithienylthieno[3,2-b]thiophene (DTT) as donor and N-alkyl diketopyrrolo-pyrrole (DPP) as acceptor moieties. They have demonstrated the stability of OFET performance in ambient conditions over one year. Using this CP PMOS inverter devices and functional oscillator circuits have also been fabricated. However, for practical applications ambipolar TFTs with a dual-nature single semiconductor are superior to dual unipolar component systems, i.e., bilayers, or bulk-heterojunction blends due to their simplicity of circuit design and fabrication processes [21]. The D-A CPs are fundamentally ambipolar transport semiconductors [13]. There are many reports for ambipolar CP-FETs and highest hole and electron mobilities of 3.97cm^{2}V^{-1}s^{-1} and 2.20cm^{2}V^{-1}s^{-1} has been achieved for PTDPPSe-Si [62].

These results show a significant achievement in CP-FET development and are milestones for technological translation of OFETs from laboratory to marketplace.

However, for flexible electronic devices and long term air-stability, studies for electromechanical properties and long term stability of CP-FET have to be investigated.

1.5.2 Conducting polymer gas sensors

Using conducting polymers, various types of sensors, such as chemiresistive, diode, FET, surface acoustic wave (SAW), optodes and amperometric, have been widely fabricated[64]. In this section, we will focus only on chemiresistive and FET sensors as they are the main goal of the current thesis work.

(a) Chemiresistive sensor

A chemiresistive sensor essentially is a “resistor” whose electrical resistance is very sensitive to the chemical environment [64, 65]. In its simplest form, a chemiresistive sensor consists of a film of organic semiconductor to which two electrical contacts are made for resistance measurements, as shown in Fig. 1.12 (a). Electrical contacts are usually made by thermally evaporating metals (e.g. Au and Ag) on organic semiconductor film. A change in electrical resistance of the chemiresistive is measured as a function of time for a known amount of exposed gas. The resistance can be measured by a simple ohmmeter. Alternatively, a constant potential is applied to the sensor and the change in current is measured. An equivalent circuit diagram of the chemiresistive sensor is presented in Fig. 1.12(b), which consists of the contact resistances (R_c), bulk resistance of the organic semiconductor film (R_B) and resistance of the substrate-film (R_{s-f}) and film-air (R_{f-a}) interface layers. A change in any of these resistances will cause a consequential change in the overall resistance of the sensor. For an organic semiconductor, bulk conductivity is a product of the density of charge carriers, their mobility and the charge of an electron/hole. Therefore, a change in conductivity on exposure to gas will not only depend on a change in density of the charge carriers but also on the crystallinity of the film. This is because better crystallinity of the film will have better mobility. Thus, the sensing behaviour of organic semiconductor films largely depends on their quality.

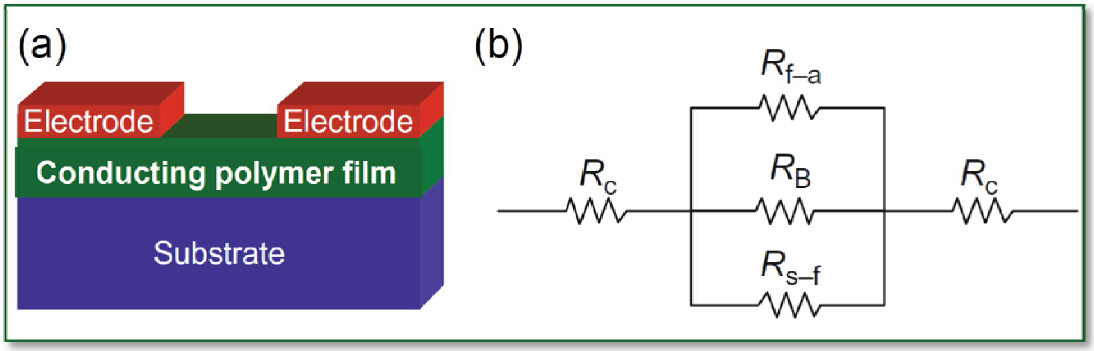

Fig. 1.12: (a) Schematic diagram showing the configuration of a chemiresistive sensor and (b) its equivalent circuit [67].

A chemiresistive sensor is characterized by the following five parameters: (i) sensitivity, (ii) response time, (iii) recovery time, (iv) selectivity, and (v) long-term stability. The sensitivity (S) of a sensor can be defined in many ways, including (a) a ratio of resistance in air to that in gas, i.e. $S=R_{air}/R_{gas}$, (b) $S(\%)=100\times(R_{air}-R_{gas})/R_{air}$ (a positive value of S implies film resistance decreases on gas exposure and vice versa) or (c) $S(\%)=(C_{gas}-C_{air})/C_{air}\times100$, where C_{gas} and C_{air} are the conductance in gas and air, respectively. The response time is the time interval over which resistance attains a fixed percentage (usually 90%) of final value when the sensor is exposed to full-scale concentration of the gas. The recovery time is the time interval over which sensor resistance reduces to 10% of the saturation value when the sensor is exposed to full-scale concentration of the gas and then placed in the clean air. A good sensor should have small response and recovery times so that the sensor can be used repeatedly. Moreover, the sensor should be selective only to a particular gas and it should not degrade with continuous operation for long durations.

As discussed earlier, doping can easily modify the electrical conductivity of the conducting polymers. Because the doping level of conducting polymers can easily be changed by chemical reaction with many gases, conducting polymers can be effectively used for their sensing. The doping and dedoping of conducting polymers are performed using redox reactions; i.e. the doping level can be altered by transferring the electrons from or to the analytes [66-70]. For instance, electronacceptor gases, such as NO_2 and Cl_2, can remove the electrons from the conducting polymers, which results in an enhancement of the conductivity of a p-type conducting polymer. On the other hand, for reducing gases like NH_3 and H_2S, the conductance of p-type conducting polymers will decrease. Exactly the opposite will take place for n-type conducting polymers. In the literature, significant efforts have been made to use conducting polymers for chemiresistive sensors. Various strategies have been used to improve the sensitivity, response and recovery times, and stability of conducting polymer-based chemiresistive sensors. These include the following:

(i) *Modifying the molecular structures of the polymers*. Conducting polymers have been modified by attaching side chains. For example alkyl, alkoxy, amine, sulphonic acid and carbon nanotubes have been attached to the backbone of polypyrrole, polyaniline, polythiophene, etc [71-76]. The grafting of side chains to the backbones of conducting polymers has two effects. First, side chains are known to increase the solubility of conducting polymers in organic solvents. This allows preparation of conducting polymer films using solution-processing-based techniques. Second, some functional chains can modify the properties of conducting polymers, such as the space between molecules [77]or dipole moments [78], or bring additional interactions with analytes. These changes can enhance the response, shorten the response and recovery time, or produce new sensitivity to other gases.

(ii) *Changing dopant*. Dopants can strongly affect the electrical properties of conducting polymers as the doping levels and the properties of counterions directly determine the conductivity of conducting polymers [74, 79, 80]. For example, the conductivity of ClO_4^{2-}doped PPy is higher than that of p-toluenesulphonate doped PPy. As a result, conducting polymers doped with different ions may give distinct responses to a specific gas. For instance, PANI doped with inorganic ions showed a resistance increase to ammonia, whereas acrylic-acid-doped PANI exhibited an inverse response [79].

(iii) *Hybrid conducting polymer*. Incorporating a second component into the conducting polymer has been widely used to develop new chemiresistive gas sensors. The advantage of this technique over modification of molecular structure of conducting polymers is that it avoids complicated chemical synthesis. Hybrid/composite polymers have been prepared using insulating polymers, molecular semiconductors, C_{60}, carbon nanotubes, metal clusters and metal oxides [81-90]. The functions of a second component in hybrids can be different, depending upon its nature. The second components play an important role in the sensing process by either improving the properties of the sensing film, e.g. its morphology and mechanical properties, or assisting in electron or proton transfer, or directly interacting with gas.

(b) Conducting polymer FET sensors

As discussed earlier, OFET consists of active layer separated by gate electrode by dielectric layer and current between the source and drain can be controlled by application of gate bias. Exposure of gas to OFET may bring change in OFET characteristics and may be studied in two configurations: (i) if the active layer of OFET is CP and (ii) if CP (e.g. PANI) is used as gate [91, 92]. The studies on 2nd case are based on the change of work function of the gate which mainly shifts the threshold voltage (V_{Th}). Though there are studies done by many groups using CP as gate electrode [93-96], here our discussion will be focused on the 1st case where the CP his used as active layer of the OFET i.e. CP-FET due to following advantages[92]: (i) in CP-FET exposure of gas brings greater changes in mobility, source-drain current, and V_{Th}. So, response may be monitored using any of these parameters depending upon relatively larger changes in these parameters. (ii) There are many CPs which can be used as active layer but for gate electrodes choices are very few. (iii) It is easy to process CPs as active layer by solution processing. For CP-FET only two geometries (BGTC and BGBC) can be used for gas sensing the active layer is exposed to ambient gas.

Table 1.2: Summary of literature on CP-FET based sensors.

Active Layer	**Geometry**	**Substrate**	**Analyte Gas**	**Detection range (Conc. in ppm)**	**Ref.**
P3HT	BGBC	Si	Ammonia (NH_3)	100%	[97]
P3HT	BGBC	Si	Nitrous oxide (N_2O)	1000	[84]
poly(3-butylthiophene)			Water vapor, Chloroform gas		[98]
Poly DDT	BGBC	Si	1-Hexanol	700-1500	[78, 100]
Poly DPOT	BGBC	Si	Ethanol, 1-Hexanol	700-1500	[78, 100]
Chiral glucose substituted poly(phenyleneethynylene)	BGBC	Si	Menthol	50-300	[101]
PEDOT	BGTC	Glass	Moisture	0-55% (RH)	[102]
P3HT	BGTC	Si	Ammonia	10—100	[103]
P3HT	BGBC	Si	Ammonia	0.1-25	[104]

A literature survey on CP-FET based sensors is summarized in Table 1.2. After the initial reports on fabrication of CP-FETs in 1980s, studies for its gas sensing properties has been started by Assadi et al [97]. They have studied first time the effect of ammonia gas on the field effect mobility of P3HT based OFET. They found the reversible change in mobility for shorter period of exposure (100% ammonia), but change was irreversible if exposed for longer period (more than 20minutes). Whereas Ohmori et al. observed that enhancement in the source–drain currents of P3HT-FET on exposure of water vapor and chloroform gas [98]. The research on CP-FET gas sensors was accelerated after year 2000. In 2001, Crone et al fabricated arrays of gas sensors OFETs based on CPs, small molecules and oligomers [99]. They have measured the change in I_{DS} by exposing variety of gaseous analytes (alcohols, ketones, thiols, nitriles, esters, and ring compounds) and recorded a pattern associated with each analyte. This shows the potential of field-effect sensors for use in electronic noses.

Torsi et al. investigated the effects of the molecular structure of the active material for CP-FET sensors by taking two different types of active layers having same polythiophene backbone but substituted with alkyl and with alkoxy side chains i.e. PDDT and PDPOT respectively [78, 100]. It was found that for ethanol vapor PDDT-FET showed no response whereas PDPOT-FET shows an appreciable response. However for 1-hexanol both the CP-FETs have shown good sensitivity. The responses of PDDT-FET with alkyl side chains were correlated with the alkyl chain length of the analyte, whereas responses of PDPOT-FET with alkoxy side were correlated with the dipole moment of the analyte. They have measured the change in I_{DS} and found decrease in I_{DS} upon exposure to analyte gas. This behavior was attributed to enhancement of the barriers between the grains by physisorption of the analytes at the polymer grains which leads to the decreased I_{DS}. They have compared the CP-FET sensor response with the QCM (quartz crystal microbalance) sensor results and found the parallel trend in sensor's responses in both the cases. Based on this they proposed that signal is originated by the analyte physisorption on the active layer. These results shows that selectivity can be enhanced by tuning of chemical structure of active layer i.e. CPs. This strategy was further extended by Tanese et al. by using chiral glucose substituted poly(phenyleneethynylene)-FET for sensing of menthol enantiomers [101]. Kang et al studied the effect of moisture on PEDOT-FET [102]. They observed decrease in σ_{dc} and I_{DS} under a positive gate bias at a finite humidity, and no change in σ_{dc} in vacuum. This was explained by moisture assisted dedoping and the redoping processes of the PEDOT channel upon applying and removal of positive gate bias. Bufon and Heinzel fabricated PPy-FETs and demonstrated sensitivity of these FETs towards oxygen [105]. Jeong et al has studied the ammonia gas sensing characteristics for bottom gate-top contact OFETs made from spin-coated P3HT on a thermally grown SiO_2/Si wafer [103]. The gas response characteristics were studied by measuring the change in drain-source current with ammonia exposure (10-100ppm). The response characteristics of the OFET sensor show that there is a shift in the threshold voltage as well as a change in mobility after exposure to ammonia gas. Tiwari et al have reported detection of lower concentrations (0.1-25ppm) of ammonia using P3HT based bottom gate- bottom contact OFET as sensor [104]. However, all the above studies were done on rigid substrates and for flexible sensors there is need for studies of gas sensing characteristics of flexible CP-FETs.

1.6 Motivation and outline of the thesis

As discussed in the previous section, conducting polymers are promising candidates for largearea and ubiquitous electronic applications, such as displays, sensor arrays and smart cards, etc. In the past decade, great efforts from both, academy and industry, have been made to boost organic electronics into commercial market. Unlike inorganic semicondcutors, conducting molecules pack up through weak Van der Waals forces and π–π interactions rather than rigid covalent bonds. The weak intermolecular interaction not only makes conducting polymers potentially soluble and easy to be processed in solution, but also endows conducting polymer electronic devices the nature of flexibility. However, most conducting polymer electronic devices reported so far are fabricated on inorganic substrates, such as glass sheets and silicon wafers, which have limited the intrinsic flexibility of conducting polymers.

In this thesis, we focus on:

(i) Preparation and characterization of flexible thin films of polypyrrole and PCDTBT conducting polymers. For this purpose we have adopted two different strategies: (a) synthesis of flexible freestanding conducting polymer films by interfacial polymerization at either the liquid–liquid or the liquid–air interface, and (b) deposition of conducting polymer films as well as nanocomposite films on flexible biaxially oriented bi-axially oriented polyethylene teraphthalate (BOPET) substrate.

(ii) Investigation of charge transport in these flexible conducting polymer films, by measuring the temperature dependence of resistivity and current-voltage characteristics and

(iii) Fabrication of FETs and gas sensors using the prepared flexible polypyrrole and PCDTBT films.

The experimental work carried out and the results obtained during the thesis work are arranged into following Chapters.

Chapter 2 describes the details of the experimental work on the preparation of the flexible PPy and PCDTBT films using interface polymerization and spin coating. Fabrication process of FET and sensors devices is described. The overview of various techniques used for the characterization of polymer films, are presented. The details of the experimental setups used for the measurements of OFET and gas sensing characteristics are described.

In ***Chapter 3*** we describe the results of interfacial polymerization at liquid/air, and liquid/liquid for preparing the freestanding polypyrrole films. The charge transport properties of these films are investigated. The use of these freestanding films for fabrication of sensors, field effect transistors and memory are described.

In ***Chapter 4***, we describe synthesis of flexible polypyrrole-silver (PPy–Ag) nanocomposite films on a N-(3-trimethoxysilylpropyl)pyrrole modified biaxially oriented polyethylene terephthalate (BOPET) substrate by photopolymerisation of pyrrole using $AgNO_3$ as a photo-initiator. The charge transport in these films is investigated. In addition, the gas sensing characteristics of these films are investigated.

In ***Chapter-5*** we demonstrate fabrication of flexible FETs using poly[N-9'-heptadecanyl-2,7-carbazole-alt-5,5-(4',7'-di-2-thienyl-2',1',3'-benzothiadiazole)], PCDTBT, as an active channel, poly(methyl methacrylate) (PMMA) as gate dielectric and biaxially oriented polyethyleneterephthalate (BOPET) as supporting substrate. The output and transfer characteristics of the devices were measured as a function of channel length. The studies on the air stability and effect of strain on the mobility have been investigated.

In ***Chapter 6***, we present a summary of the main results of the current thesis work, and highlight the future scope of the work.

Chapter -2

Experimental Techniques

As mentioned in Chapter -1, our main focus of the current thesis work is to synthesize the flexible thin films of polypyrrole and PCDTBT conducting polymers. For this purpose we have adopted two methodologies: (i) interfacial polymerization, which yields thin freestanding sheets of the conducting polymers; and (ii) deposition of the conducting polymer films onto the flexible BOPET substrates. In this chapter, first we describe the details of experimental methods for obtaining the flexible polypyrrole films, and followed by the methodologies used for the fabrication of gas sensors and field-effect transistors. The grown flexible conducting polymer films have been characterized by a number of techniques, and a brief description of these techniques is also presented. Finally we describe the setups used for the measurements of gas sensing and OFET characteristics'.

2.1 Deposition of flexible polypyrrole films

2.1.1. Materials

The sources of various materials used in the present thesis work are summarized below.

Pyrrole: Pyrrole (98%) was procured from Aldrich and distilled over calcium hydride under reduced pressure prior to use.

$FeCl_3$: Anhydrous $FeCl_3$ (LR grade) was purchased from Thomas Baker.

Solvents: The organic solvents used were of analytical grade, and Millipore water was used for washing and solution preparation.

TPPOH: 5-(4-hydroxyphenyl)-10,15,20-triphenylporphyrin (TPPOH) was synthesized using following method[106]: To a solution of benzaldehyde (27.9 g, 0.262 mol) and 4-hydroxybenzaldehyde (10.7 g, 0.0876 mol) in propionic acid (800 ml), a solution of pyrrole (23.9 g, 0.356 mol) in propionic acid (200 ml) was added drop wise under vigorous stirring. The brown solution was then refluxed for 1h and cooled to ambient temperature. The precipitate thus obtained was collected and washed with methanol to get a purple colored solid. The solid was purified by silica gel column chromatography using dichloromethane-hexane as eluent to furnish TPPOH as purple crystals (1.8 g, 3.2 % yield).

$AgNO_3$: Silver nitrate (Sigma-Aldrich, purity ~ 99.9%) was of analytical grade and was used as received.

BOPET: Biaxially-oriented polyethylene terephthalate (BOPET) sheets of thickness ~ 100 μm were procured from DuPont. These sheets were cut into size of 10 mm ×10 mm using a pair of scissor for the experiments. It may be noted that flexible BOPET sheets are manufactured from molten polyethylene terephthalate (PET), which are then biaxially oriented by drawing and "heat set" under tension at temperatures >200°C to prevent the sheet from shrinking back to its original un-stretched shape and locking the molecular orientation in the sheet plane. This leads to the semicrystalline nature of the BOPET sheets [107]. These sheets were used as flexible substrates for the preparation of conducting polymer films and devices.

Silane:	N-(3-trimethoxysilylpropyl)pyrrole (purity ≥ 98%) used for surface modification of BOPET, was procured from Flurochem.
PCDTBT:	Poly[N-9'-heptadecanyl-2,7-carbazole-alt-5,5-(4',7'-di-2-thienyl-2',1',3'-benzothiadiazole)], (PCDTBT), Mw = 36.5 kDa, was purchased from Ossila and used as an active layer in field effect transistors.
PMMA:	Poly(methyl methacrylate), PMMA, Mw = 996 kDa, was purchased from Aldrich, and used as dielectric material in field effect transistors.

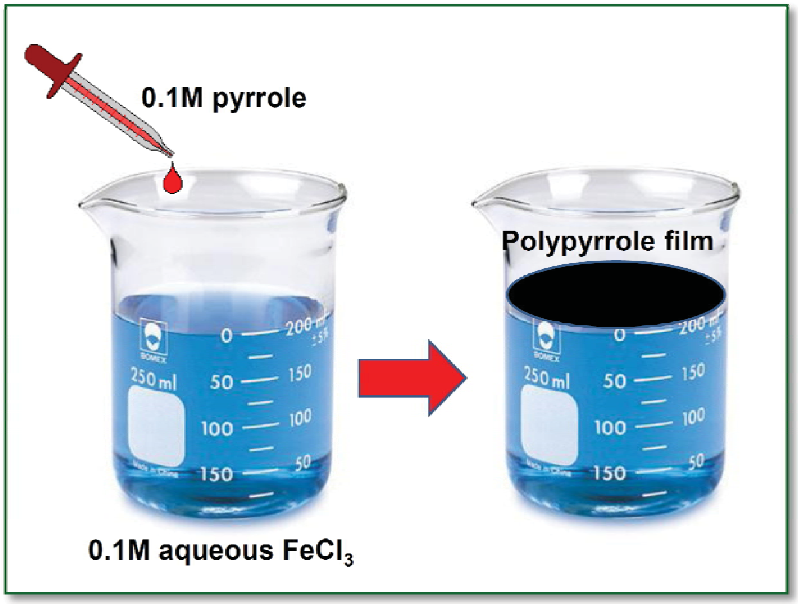

Fig. 2.1: Schematic representation of the interfacial polymerization at the liquid/air interface.

2.1.2 Freestanding films by interfacial polymerization

Free-standing polypyrrole films were synthesized under ambient conditions using interfacial polymerization. The details of the experimental conditions on the interfacial polymerization are discussed in Chapter 3. Here we describe the concepts of interfacial polymerization at air/liquid interface, which we have used in the present thesis work.

The schematic of the interfacial polymerization at the air/liquid interface is shown in Fig. 2.1. In this case, a certain quantity is of oxidant $FeCl_3$ is taken in a beaker, and then the solution of pyrrole monomer is dropped slowly using a micropipette. The polypyrrole film formation takes place at the air/liquid interface. The thickness and quality of the polypyrrole films depends upon several factors, such as the quantity of the pyrrole solution and its concentration. In addition, we have used the acidic interfacial polymerization which is discussed in detail in Chapter 3.

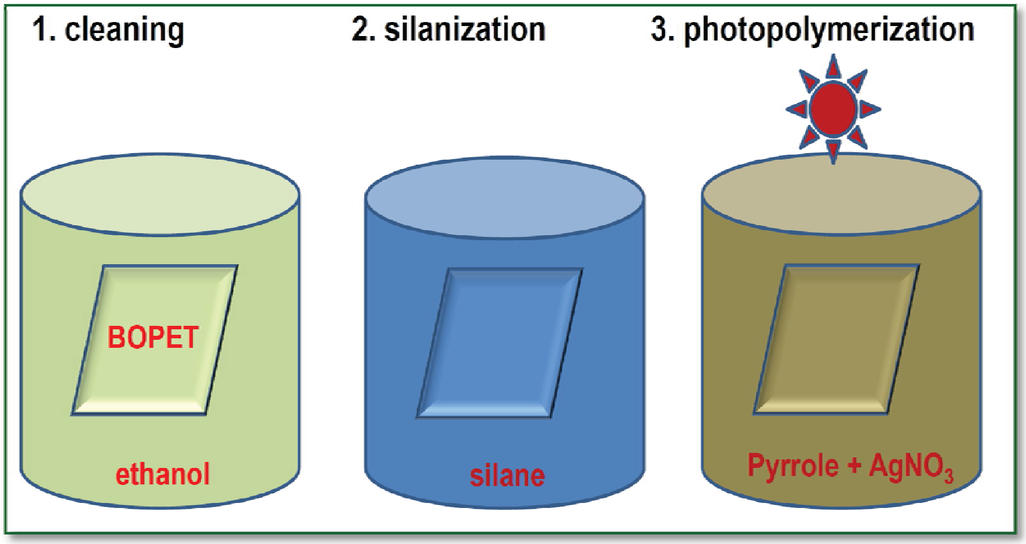

Fig. 2.2: Schematic representation of three step process for the deposition of adherent polypyrrole/Ag films onto the flexible BOPET substrates.

2.1.3 Photopolymerization of PPy/Ag nanocomposites on flexible BOPET substrates

This is another approach of preparing the flexible films, whereby conducting polymer film is grafted onto to the flexible substrate. It is almost difficult to prepare adherent polypyrrole or poypyrrole/Ag nanocomposite films onto the native surface of the flexible BOPET surface, as the polypyrrole does not form the covalent bonding with BOPET. In order to improve the adhesion of the polypyrrole films onto the BOPET surface, we have devised in a new process, as schematically shown in Fig. 2.2. Briefly, the process is done in three steps: (i) Cleaning: ultrasonic cleaning of BOPET sheets using organic solvents, (ii) Silanization: a self-assembled monolayer terminated with pyrrole is deposited onto the hydroxylated BOPET sheet; and (iii) Photopolymerization: the silanized BOPET is dipped in the solution of pyrrole and $AgNO_3$ under UV radiation. The details of experimental results are presented in Chapter 4.

2.2 Fabrication of the flexible devices

2.2.1 Gas sensors

Fabrication of chemiresistive gas sensors is very simple. For this purpose, pair of Au electrodes (size: 3 mm x 2 mm, thickness ~1 μm) separated by 12 μm gap are thermally deposited onto freestanding polypyrrole films or flexible polypyrrole/Ag composite films on BOPET. For freestanding PPy nanosheets interdigited gold electrodes were deposited using shadow mask. Gold was chosen as the electrode materials due to: (i) Au has a matching work function (~5.2 eV) with polypyrrole, and therefore, yields an ohmic contact and (ii) Au being a noble metal does not react with most of the test gases.

2.2.2 FET fabrication

Before we describe the fabrication process of the field effect transistors, we would line mention here that due to the requirement of very clean interfaces, as discussed in Chapter 1, the entire fabrication of FET was carried out in a Glove Box (MBraun). The photograph of this glove box is shown in Fig. 2.3.

This glove box is on slight positive partial pressure of Ar and has moisture and oxygen levels <1ppm. It has two boxes: the Box-1 has spin coater for deposition of conducting polymer thin film deposition, and the Box-2 has thermal evaporation system for the metallization. The entire field-effect transition fabrication, as schematically represented in Fig. 2.4, can be carried out in this glove box, without exposing the samples to atmosphere. Briefly, a Cleaned BOPET substrate was coated with thermally evaporated Al film (to be used s gate electrode) in Box-2, this sample was then transferred to Box-1 for the deposition of PMMA dielectric (followed by annealing) and PCDTBT active layer depositions by spin coating. The samples was then transferred back to Box-1 fordeposition of the source-drain pairs of Au using thermal evaporation though a steel shadow mask. The details of this process are presented in Chapter 5.

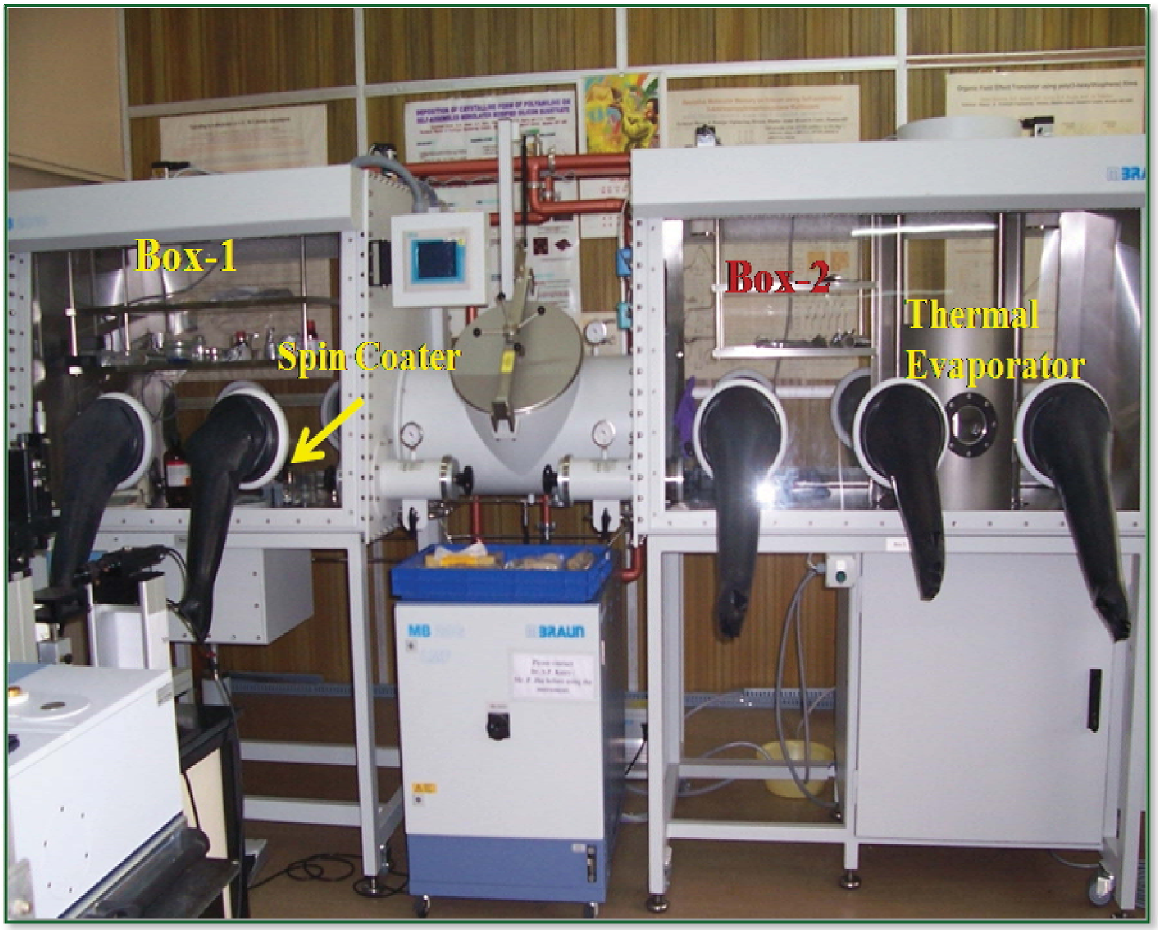

Fig. 2.3: The photograph of theMBraun modular glove box system.

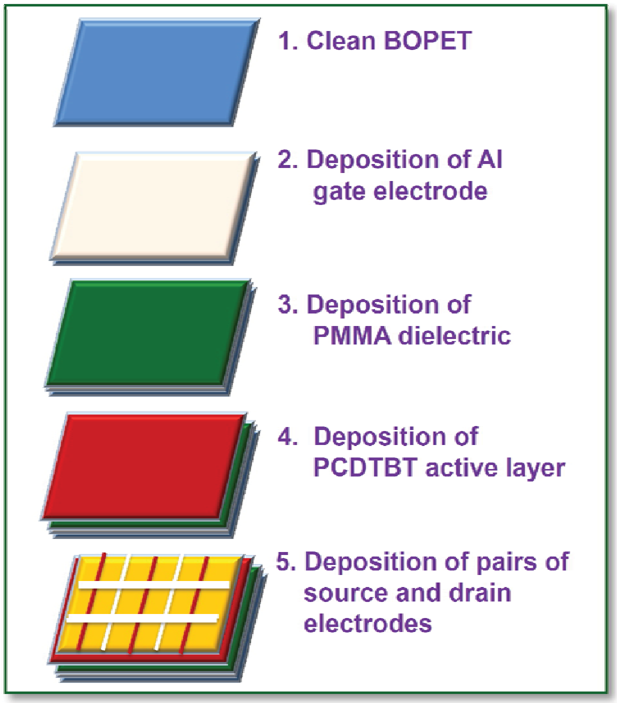

Fig. 2.4: Schematic representation of different steps in the fabrication of the PCDTBT based filed effect transistors.

2.3 Techniques for film characterization

All the films prepared in the thesis work were characterized by a host of techniques, which includes spectroscopic characterization, morphological characterization, surface hydrophobicity measurement and electrochemical characterization.

2.3.1 Spectroscopic characterization

For spectroscopic characterization of films UV-Visible spectroscopy, Fourier transform infrared spectroscopy (FTIR), Raman spectroscopy and X-ray photoelectron spectroscopy (XPS) were used. These techniques are described below.

(a) UV-Visible Spectroscopy

UV- visible spectroscopy was used to characterize is the electronic transitions in PPy and PCDTBT films. This technique was also used for the mechanistic study of the interfacial polymerization of PPy and effect of bending on PCDTBT films on flexible substrate which will be described in Chapters 3 and 4.

In this spectroscopic technique the absorption of ultraviolet/visible radiation results from transition among the electronic energy levels which involve bonding electrons (σ, π or even non bonding electrons) [108].Therefore, the wavelength of absorption peaks can be correlated with the type of bonds in the absorption particularly extent of multiple bonds or conjugation within the molecule. UV-Visible spectrum also provides information about the effect of substituent on the conjugation of the molecule/polymer as it shifts the molecular orbital energy level. The shift of position of VU-Vis band towards longer wavelength is known as bathochromic shift or red shift and towards the lower wavelength is known is hypsochromic shift or blue shift. There may be also the change in intensity due to the conformation change in the molecule/polymer. The increase in intensity of absorption is called hyperchromic effect whereas decrease in intensity hypochromic effect.

Quantitive estimation of chromophore can also be done using UV-Visible spectroscopy. It is done using Beer-Lampbert law:

$$A = \varepsilon C L$$

where A is absorbance, ε is absorption coefficient, C is the concentration of chromophore and L is the path length of the cell. First we have to calculate the calibration curve (A vs C) of chromophore for a known concentration range and then knowing the value of absorbance the concentration can be calculated. From the calibration curve absorption coefficient of the chromophore can also be calculated [108]. For our experiment we have use JASCO V-530 spectrophotometer (Fig. 2.5).

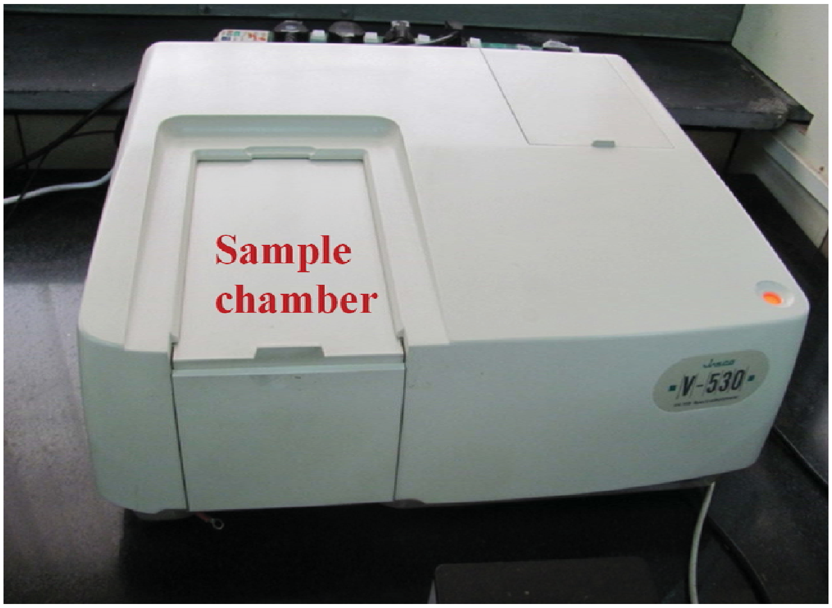

Fig. 2.5: Photograph of UV-Visible spectrophotometer.

The schematic of the double beam single monochromator spectrometer is shown in Fig. 2.6.In this spectrometer the intensity (I) of the beam passing through the sample is compared with a reference beam(I_0) and in the output we get absorbance($A=\log_{10}I/I_0$) vs wavelength.

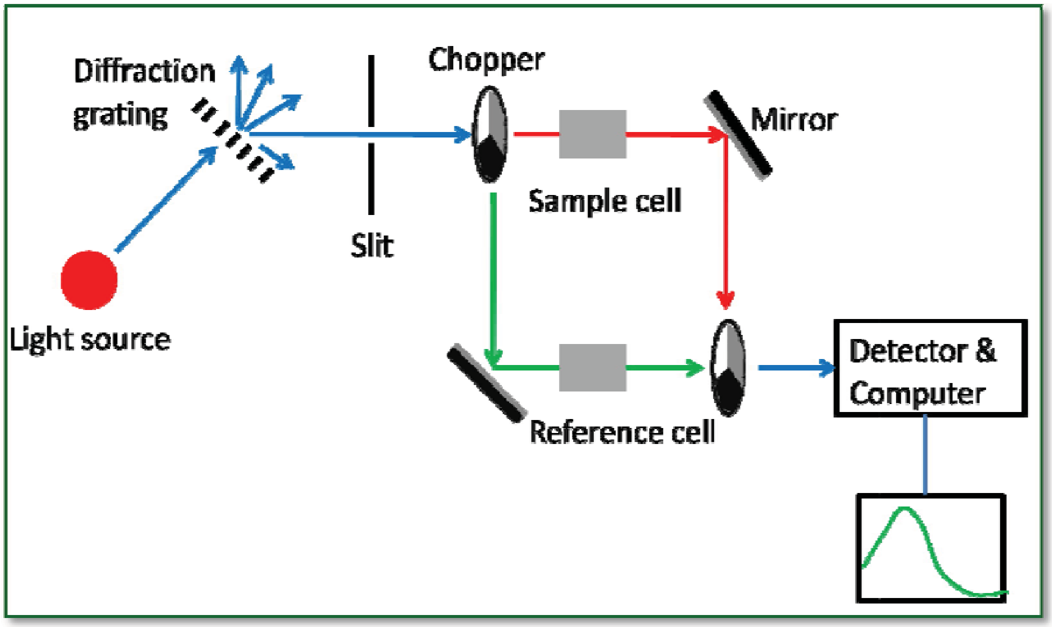

Fig. 2.6: Schematic of the double beam single monochromator spectrometer

(b) Fourier Transform Infrared Spectroscopy

Fourier Transform Infrared spectroscopy (FTIR) provides the information of different vibrational frequencies related to chemical bonds. The frequencies and intensities of the vibrational modes observed in FTIR provide detailed information about the nature of the chemical functional groups present in the organic molecule [109]. FTIR spectra were recorded using Bruker system (vertex 80V), the photograph is shown in Fig. 2.7. The necessary condition for the infrared absorbance is the presence of permanent dipole moment or change in dipole moment of the chemical bond (between two atoms) when it interacts with IR. The absorption of IR leads to transition in vibration levels. So IR absorption helps to identify the characteristic vibrational frequencies of organic functional group. Most of the organic molecules have vibrational frequencies in the mid infrared range of 4000 to 400 cm^{-1}.

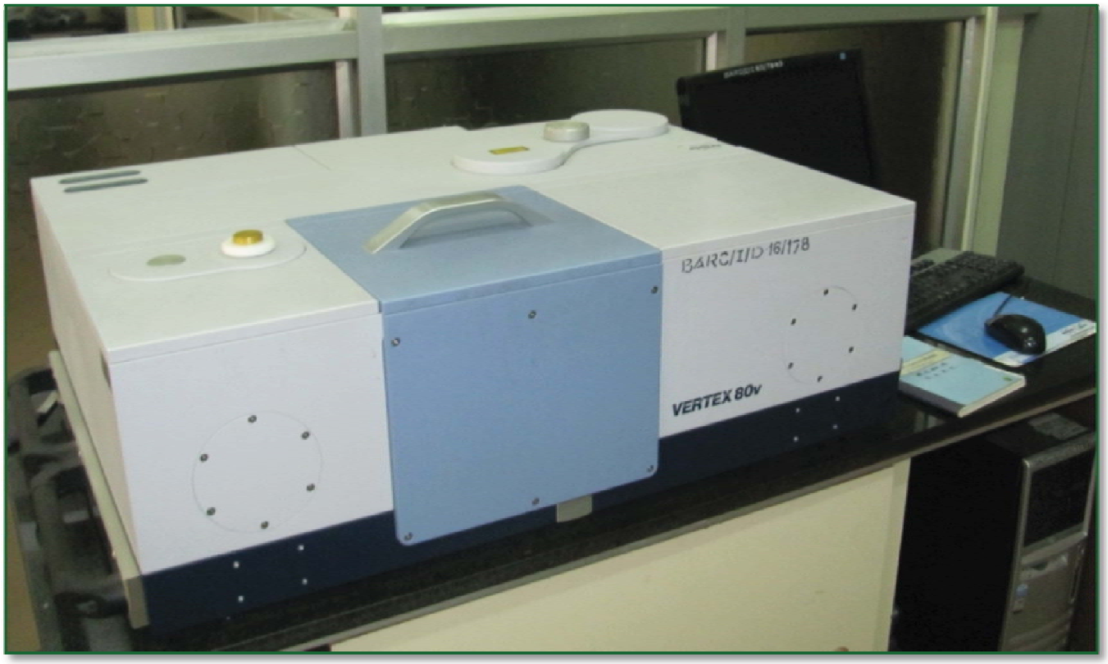

Fig. 2.7: FTIR Bruker system (vertex 80V)

FTIR works on the principle of interferometer that gives an interferogram, a plot of light intensity versus optical path difference. The ray diagram of formation of interferogram is shown in the Fig. 2.8. This interferogram is finally Fourier transformed to give a spectrum of infrared radiation intensity versus wave number.

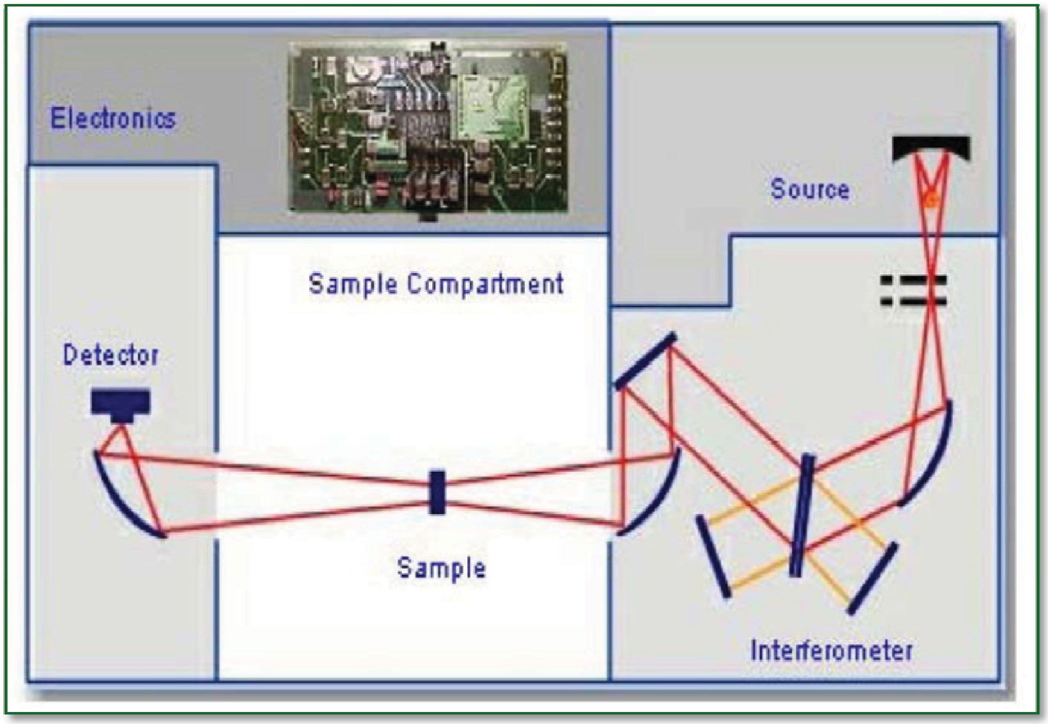

Fig. 2.8: Schematic diagram of interferogram formation.

For our experimental purpose, FTIR spectra were recorded in two different spectroscopy modes: attenuated total reflection (ATR) and diffuse reflectance mode. In the ATR mode, an infrared beam is directed onto an optically dense crystal with a high refractive index at a certain angle. This internal reflectance creates an evanescent wave that extends beyond the surface of the crystal into the sample held in contact with the crystal. This evanescent wave protrudes only a few microns (0.5 - 5 μ) beyond the crystal surface and into the sample. Consequently, there must be good contact between the sample and the crystal surface. In regions of the infrared spectrum where the sample absorbs energy, the evanescent wave will be attenuated or altered. The attenuated energy from each evanescent wave is passed back to the IR beam, which then exits the opposite end of the crystal and is passed to the detector in the IR spectrometer. The system then generates an infrared spectrum. This mode is very good technique to measure FTIR spectra of the film.

In diffuse reflectance (DR) mode, the IR beam enters the sample, it can either be reflected off the surface of a particle or be transmitted through a particle. The IR energy reflecting off the surface is typically lost. The IR beam that passes through a particle can either reflect off the next particle or be transmitted through the next particle. This transmission-reflectance event can occur many times in the sample, which increases the path length. Finally, a spherical mirror that is focused onto the detector collects such scattered IR energy. The detected IR light is partially absorbed by particles of the sample, bringing the sample information.

(c) Raman Spectroscopy

Raman spectroscopy is non-destructive and non invasive technique [109]. When a sample (organic/inorganic compounds) is irradiated with a monochromatic intense exciting light source (in our case laser beam), the scattered light consists of additional discrete frequencies along with Rayleigh line. Rayleigh line is the light with irradiated frequency. The shift in frequency from the Rayleigh line is known as Raman shift. Raman shifted photons of light can be either of higher or lower energy, depending upon the vibrational state of the molecule: (i)The stronger of the two processes is the photon is scattered at lower energy –known as the Stokes scattering, as at room temperature the population state of a molecule is principally in its ground vibrational state. (ii) a small number of molecules will be in a higher vibrational level, and hence the scattered photon can actually be scattered at a higher energy-known as Anti-Stokes Raman scattering.

The Raman shifts when plotted against their intensities gives the spectrum known as Raman spectrum. The Raman shift is related to vibrational frequencies of the molecules in the sample. Not all vibrations will be observable with Raman spectroscopy (depending upon the symmetry of the molecule). For a molecule to be Raman active the molecular rotation or vibration must be accompanied with change in polarizability. Raman spectroscopy gives information about molecular structures and bonding of the sample. Raman scattering is a relatively weak process with very small number of Raman scattered photons. For enhancement of sensitivity many techniques like SERS, use of active substrate, etc are used. We have collected Raman spectra using a microscopic confocal Raman spectrometer (HORIBA Jobin Yvon, Lab RAM HR) employing a 514 nm laser beam and using 100X and 50X objectives at room temperature (Fig.2.9). It has CONFOCAL Raman microscope design.

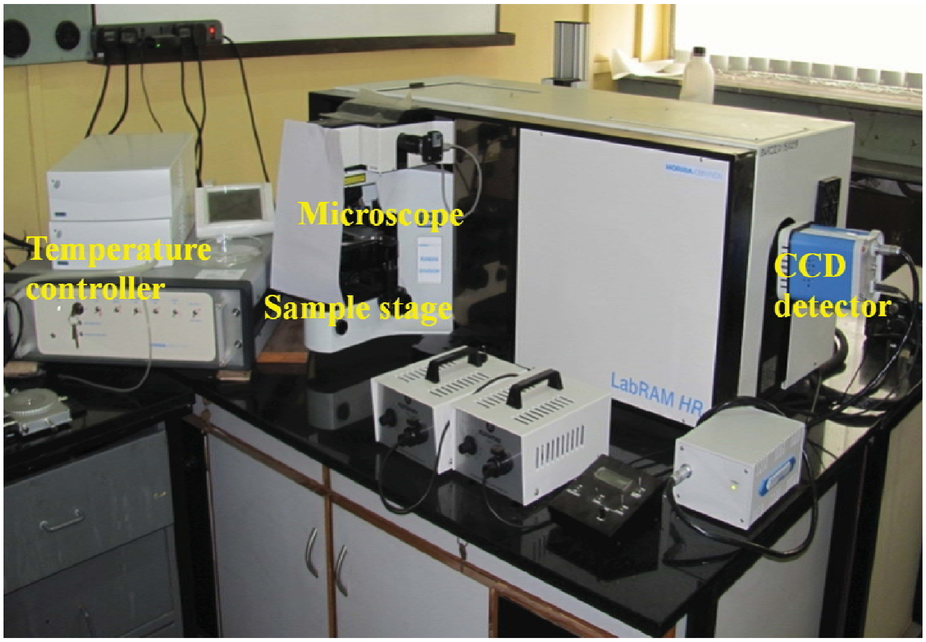

Fig. 2.9: The photograph of the Raman spectrometer.

(d) X-ray photoelectron spectroscopy (XPS)

XPS uses a soft X-ray source (Al Kα and Mg Kα) to ionize electrons (by knocking out the core-level electron) from the surface of a solid sample (top few atomic layers). The binding energies of these electrons are measured, which are characteristics of the elements and associated with chemical bonds (chemical state). The advantages of XPS technique are (i) quantitative analysis of elements and chemical states of all elements except hydrogen and helium, (ii) typical element detection limits are 0.1 atomic % from the top few nm, and (iii) samples can be conductors, semiconductors or insulators [110-112].

The XPS studies of the active layer of the OFET were carried out using an Mg Kα (1253.6eV) source and a MAC-2 electron analyser (RIBER MBE system) under a base vacuum of ~10^{-9} torr. The binding energy scale was calibrated to the Au $4f_{7/2}$ line of 84eV. Each data set was first corrected for the non-linear emission background. Peak fitting was done with the help of Casa-XPS software.

2.3.2 Morphological characterization

The surface morphology of the films was studied using atomic force microscopy and scanning electron microscopy. The instrument details and brief basic principle for both the techniques are given below.

(a) Atomic force microscopy

The surface morphology of PCDTBT and PMMA layer of OFET and PPy films synthesized by aerobic oxidation of terpyrrole at air-water interface was investigated by AFM in noncontact mode using following two systems: (i) NTMDT -Solver P47 and (ii) Multiview4000, Nanonics

The NTMDT -Solver P47 is consists of a cantilever (probe) with a sharp tip at its end that is used to scan the specimen surface. Rectangular cantilever of Si3N4 (length 200 mm and width 40 mm) having force constant of 3 N/m were employed for the measurements [113, 114]. The probe is typically silicon or silicon nitride with a tip radius of curvature of the order of nanometers. When the tip is brought into proximity of a sample surface, the Van der Waals force between the tip and the sample leads to a deflection of the cantilever according to Hooke's law. Typically, the deflection is measured using a laser spot reflected from the top of the cantilever into an array of photodiodes. A feedback mechanism is employed to adjust the tip-to-sample distance to maintain a constant force between the tip and the sample. The sample is mounted on a piezoelectric tube that moves the sample in the z direction for maintaining a constant force, and the x and y directions for scanning the sample. The resulting map of z(x, y) represents the topography of the sample.

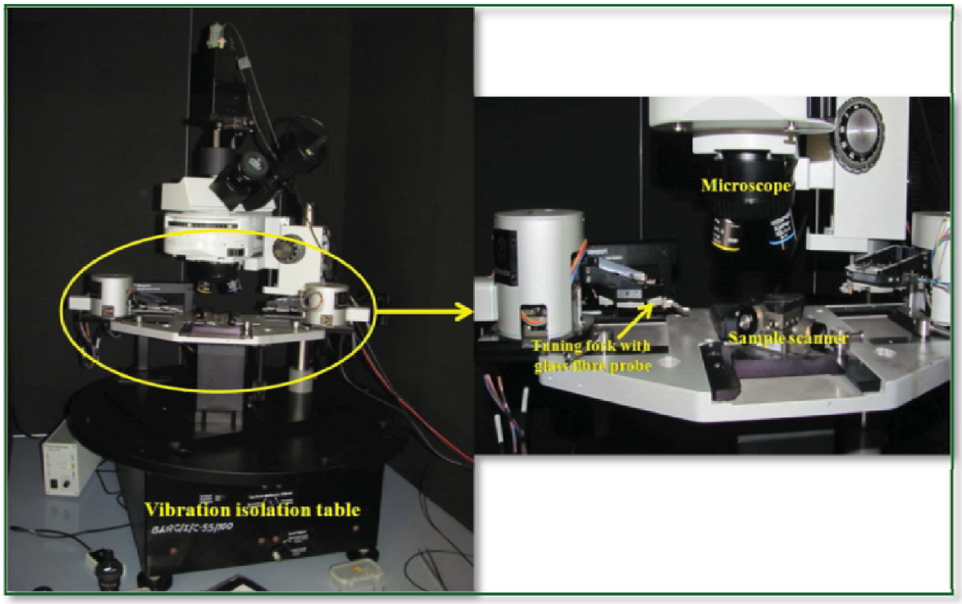

Fig. 2.10: Multiview4000, Nanonics AFM

In the case of Multiview4000, Nanonics AFM system, as shown in Fig. 2.10, the probe is made of the glass fiber tip (diameter 10nm) which is attached to tuning fork [115]. The fork is attached with pizocrystal. The image is recorded in tapping mode by oscillating the tip at resonance frequency (20-50 kHz depending on the tips). The probe was scanned at phase mode. During scan, phase changes due to tip surface interaction. The difference in signal called an error signal; this signal is sent to proportional, integrator and differentiator (PID) controller. PID sends the feedback via high voltage pizodriver to make constant phase by moving pizodriver in z direction at that x, y point. This way an image is generated. A schematic diagram of signal processing is shown in the Fig.2.11. The image so generated was processed (like smoothing, flattening etc) by NWS software [116]. This software was also used to study surface roughness by extracting line profile from the image.

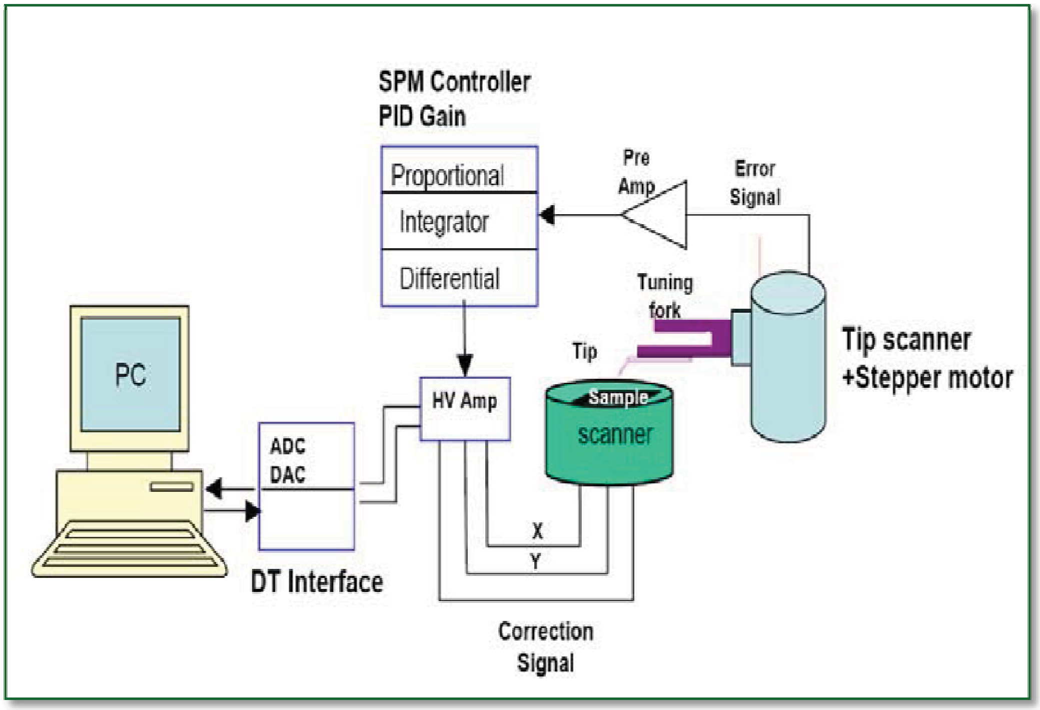

Fig. 2.11: Schematic diagram of signal processing of AFM.

(b) Scanning electron microscopy

We have used scanning electron microscope (TESCAN, TS5130MM)) to investigate the surface morphology and thickness estimation of PPy free-standing films. The scanning electron microscope (SEM) provides information relating to topographical features, morphology and phase distribution [117, 118]. The SEM set up is shown in Fig.2.12. The working principle of SEM is briefly described below.

The SEM is the focused probe of electrons accelerated to a moderately high energy and positioned on to the sample by electro-magnetic fields. These beam electrons interact with atoms of the specimen by inelastic (energy is transferred to the sample leads to secondary electrons emission) and elastic (energy is not transferred to the sample leads to back scattered electrons emission) collisions.

Fig.2.12 Photograph of the SEM instrument (TESCAN, TS5130MM)

The most widely utilized signal, produced by the inelastic interaction of the primary electron beam with the sample, is the secondary electron signal. Secondary electrons are characterized from other electrons by having energy of less than 50 eV. The secondary electron is emitted from an outer shell of the specimen atom upon impact of the incident beam. It is the most useful signal for examining surface structure and gives the best resolution image of 10 nm or better. Since the secondary electron intensity is a function of the surface orientation with respect to the beam and the secondary electron detector and thus, produces an image of the specimen morphology. The secondary electron intensity is also influenced by the chemical bonding, charging effects and back scattered electron intensity, since the back scattered electron generated secondary electrons are significant part of the secondary electric signal.

The detector is Everhart-Thornley detector composed of a scintillator, collector, light pipe, and photo multiplier tube. First electrons striking the positively biased scintillator and converted to a burst of photons, that travel through the light pipe to a photomultiplier tube which converts the photons of light into a voltage. The strength of this voltage depends on the number of secondary electrons that are striking the detector. Thus the secondary electrons produced from a small area of the specimen give rise to a voltage signal of a particular strength. The voltage is led out of the microscope column to an electric console, where it is processed and amplified to generate a point of brightness on the cathode ray tube screen. Contrast in the SEM image is the difference in intensity, or brightness of the pixels that make up the image. The difference in intensity represents difference in signal from corresponding picture elements on the sample. The back scattered electron signal can also be used to show surface topography and is often used to show atomic number contrast, in which areas of higher average atomic number produce more back scattered electrons, and thus appear brighter than lower atomic number regions. The contrast in this image is not due to color differences but is produced by different intensities of electrons back scattering from the layers with different average atomic number.

2.3.3 Contact Angle Measurement

The hydrophobicity of the films was measured by contact angle measurement system. In this method, a drop of liquid (de-ionized water or hexadecane, for instance) is expanded on the surface of the film using a syringe and the contact angle is measured. The contact angle is the angle between the tangent line drawn from the droplet to the touch of the solid surface and the solid surface, as shown in inset of Fig. We have carried out the de-ionized water contact angle measurements using Data Physics (OCA20) system, photograph is shown in Fig. 2.13. A drop of de-ionized water is spread on the surface of the film, which is then imaged by a CCD camera. The contact angle is measured using software.

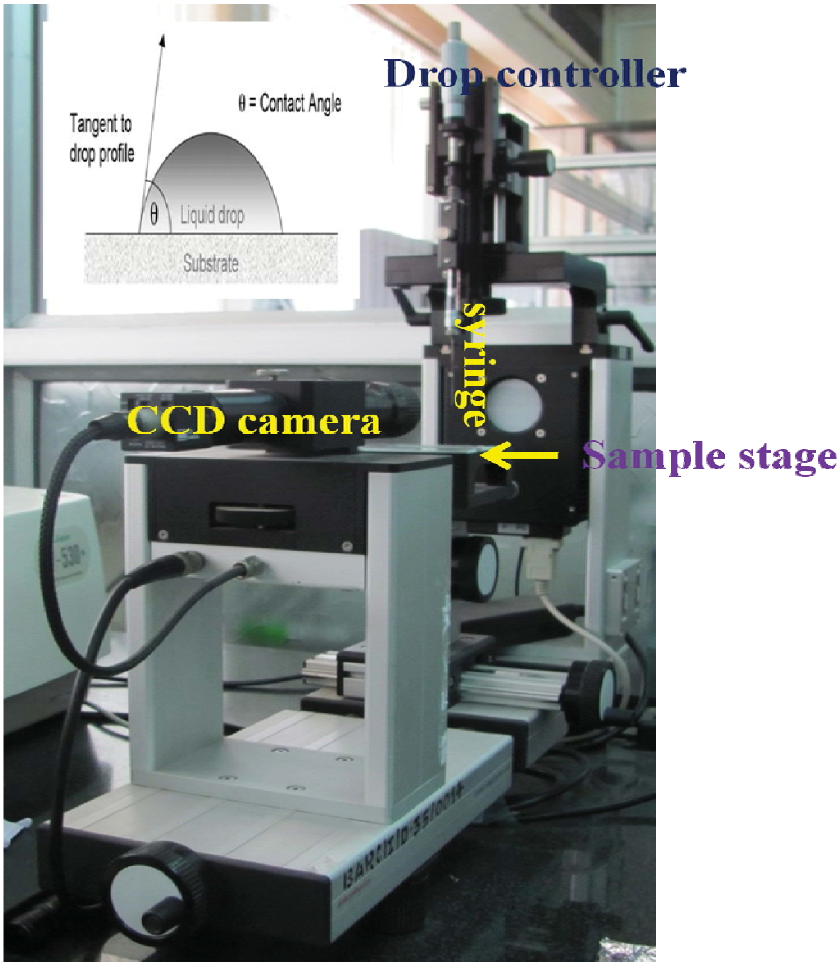

Fig. 2.13: The photograph of the contact angle measurement system.

2.3.4 Electrochemical Characterization

The cyclic voltametry studies were done using Potentiostat/Galvanostat system (model: Autolab PGSTAT 30) system (shown in Fig. 2.14. It was measured in electrochemical cell with three electrodes(working, counter and reference electrode). Free-standing PPy films on ITO coated glass were taken as working-electrode. The CE was a Pt wire. The potential (V) is measured between the reference electrode (RE) and the working electrode. No current passes through the reference electrode. Reference-electrode is an electrode, which has a stable and well known electrode potential. The high stability of the electrode potential is usually reached by employing a redox system with constant (buffered or saturated) concentrations of each participants of the redox reaction. In our case, we used pseudo RE electrode, which was prepared by depositing AgCl layer over Ag using galvanostatic method. In this method, 1 mA current was kept constant for 15 minutes between Ag wire and Pt electrode in 1 M HCl. After coating AgCl over Ag, the wire was washed thoroughly with de-ionized water to remove acid. It was then dried and used for further experiment.RE electrode was standardized with respect to redox potential of ferrocenes. The tetrabutylammonium perchlorate (TBAP) prepared in dry and deoxygenated dichloromethane (CH_2Cl_2) was used as supporting electrolytes. Frequency response analyses (FRA) for the PPy films were carried using signal of 10 mV and frequency in the range from 50 kHz to 1 mHz by FRA module in autolab PGSTAT 30.

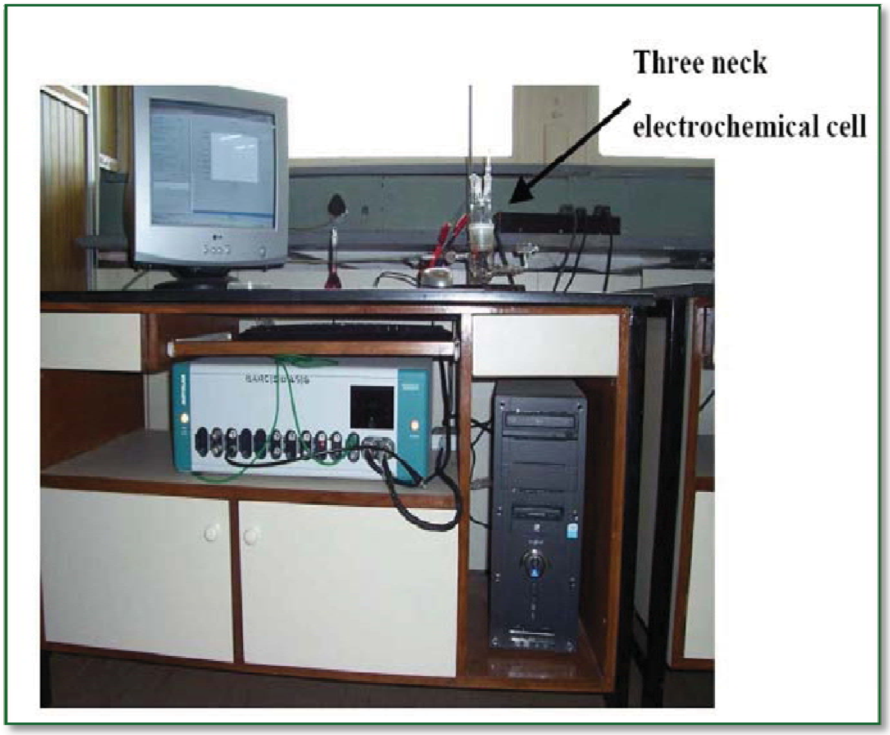

Fig. 2.14: Photograph of the Potentiostat/Galvanostat system.

2.4 Electrical measurements

Here we describe the process of metal deposition and the details of the setup used for electrical and gas sensing characterization.

2.4.1 Metal deposition

For measuring current-voltage (I-V) characteristics, capacitance and gas sensing properties of the thin films and OFETs electrode deposition was done by metal evaporation in thermal evaporation unit inside the MBraun glove box. For gate electrode and capacitance measurement aluminium was deposited with deposition rate of 0.5Å/s. For current-voltage characteristics and gas sensing studies gold electrodes were deposited using shadow mask with deposition rate of 0.5Å/s. Interdigited electrodes were deposited for gas sensing measurement of PPy free-standing films. To deposit gold electrodes, 99.99% pure gold wire is loaded on a tungsten filament which was resistively heated with external power supply. The deposition rate and thickness were monitored through a quartz crystal monitor.

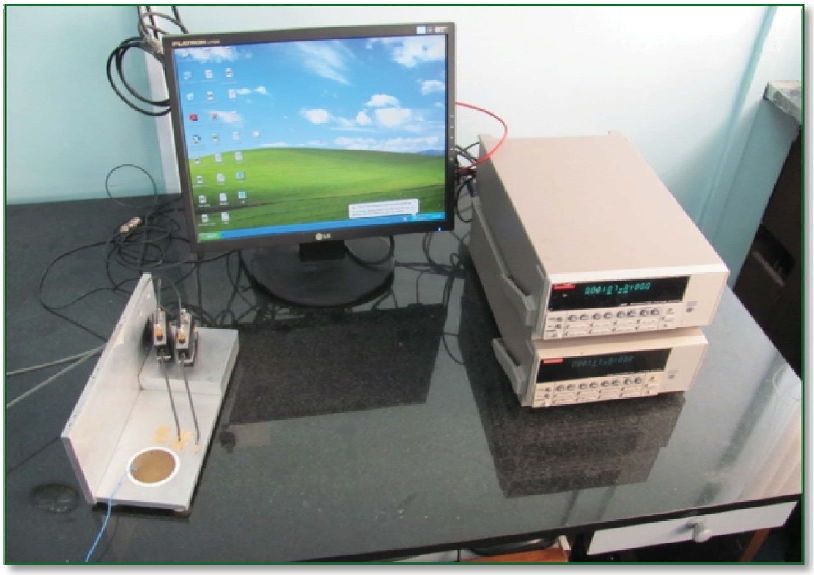

Fig.2.15: Photograph of current-voltage characteristics measurement set-up.

2.4.2 OFET characteristics and low temperature conductivity measurement

I-V characteristics and capacitance were measured under ambient atmosphere using Keithley voltage source/current meter (model 6487) and Agilent 4980A LCR meter, respectively.Micromanipulator tips were used to make contact from the electrode to source meter and LCR meter, the photograph is shown in Fig. 2.15.

For low temperature conductivity measurements two probe configuration was used. The charge transport measurements were carried out using in-plane electrode geometry. For this purpose, two planar gold electrodes of length 3 mm, width 2 mm with 12 µm electrode spacing were thermally deposited onto films using a metal mask and silver wires were attached to the gold pads with silver paint. The measurements at low temperatures (300-130K) were carried out using a closed cycle cryostat. All measurements were performed in dark to avoid the problem of photoconductivity. Conductivity measurements were carried out in a helium gas environment. The cryostat (CCR APD Cryogenics make) consists of a compressor, which compresses the Helium gas and expands it in the vicinity of the sample chamber. Because of Joule Thomson expansion of Helium gas, its temperature falls and it cools the region surrounding it. Platinum resistance sensors (Pt-100) are used to monitor the temperature. Lakeshore temperature controller (Lakeshore 330 auto tuning temperature controller) controls temperature of the sample chamber. A small manganin heater was used to heat the sample for measurements of transport properties at different temperatures.

2.4.3 Gas sensing measurement set up

Gas sensing measurements were performed in a static environment method. For PPy films a Pt wire heater was attached at the backside of the glass substrate to maintain and control the operating temperature of the sensor. The sensor films were mounted upside down in a leak tight stainless steel chamber having volume of 250 cm^3 (schematic shown in Fig.2.16). Required concentration of a test gas in the chamber was attained by introducing a measured quantity of desired gas using a syringe. For recovery of the sensor it was exposed to ambient atmosphere.

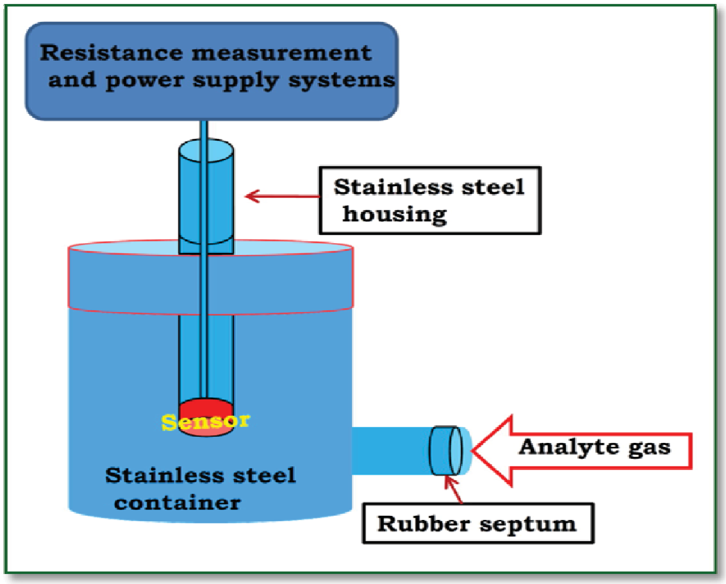

Fig.2.16: Schematic of gas sensing set-up used in the present work.

Chapter -3

Freestanding polypyrrole films

In this Chapter we describe two innovative formation methods of freestanding polypyrrole films via interfacial polymerization at air/liquid interface. The first method is based on the formation of free-standing polypyrrole nanosheets in which porphyrin-derivative is employed as an in-situ template. These polypyrrole nanosheets have been utilized for the fabrication of gas sensors and FETs. In the second method, freestanding polypyrrole films are synthesized by the acidic oxidation of terpyrrole at the air/water interface. In this case, non-conjugated polymer chains are incorporated into polypyrrole films during synthesis. These freestanding polypyrrole films show large hysteresis in current voltage characteristics along with a negative differential resistance effect. The hysteric behaviour has been utilized to demonstrate the rewritable memory effect, which has been attributed to the conformational changes of non-conjugated polymer chains in the polypyrrole matrix.

3.1. Overview of freestanding conducting films

Freestanding films are the ultrathin sheets of conducting polymers that does not require any support. In recent years there is an increasing demand for the preparation of free-standing conducting polymer films as they can provide new opportunities in several applications, such as, understanding of fundamental mechanical or electrical properties, chemical or biosensors, ion-exchange membranes, organic electronics, polymeric batteries, artificial muscles etc[119-124].As discussed in Chapter-1, among various conducting polymers, polypyrrole (PPy) is widely sought-after due to its excellent stability under environmental conditions, good conductivity, and biocompatibility [125]. The free-standing PPy films have mainly been prepared by following two methods:

(i) Deposition of PPy onto the substrates by electropolymerization or spin-coating, followed by peeling the films off the substrates [126-128] and
(ii) Synthesis by the interfacial polymerizations, that is, the film synthesized at the liquid/air or liquid/liquid interfaces are segregated [129].

The first approach either requires complicated equipment or suffers from damage during the transfer process, especially for nanometer-thick, large-area films. In addition the uniformity of the freestanding films is difficult to obtain. The second approach of interfacial polymerization is very interesting as it allows preparation of uniform freestanding films. Very recently, ultrathin free-standing PPy films have also been prepared at an air/ionic liquid interface through interface oxypolymerization [130].

In this Chapter, we report synthesis of PPy freestanding films by interfacial polymerization at air/liquid interface using following two novel strategies:

(i) Growth of free-standing PPy nanosheets at air/liquid interface by in which solution consisting of 1mM TPPOH and 0.01- 1M pyrrole) is slowly dropped into 0.1M aqueous FeCl3 kept in a beaker under steady state. Spontaneously formed TPPOH J-aggregate films at the air/ aqueous interface is found to act as an in-situ template for the growth of PPy nanosheets. The charge transport and gas sensing properties of these PPy nanosheets have been investigated.

(ii) Acidic oxidation of terpyrrole at the air/water interface, which is achieved by pouring 18% hydrochloric acid into 0.1 M pyrrole solution. This is rather a slow process and takes several days to form a freestanding film at the air/acid interface. The trimer formed at the HCl/pyrrole interface migrates towards air/liquid interface, it get polymerized by aerobicoxidation to PPy via terpyrrole. We demonstrate the memory effect in these PPy films, and the memory effect is attributed to the presence of non-conjugated chains that get incorporated into the PPy matrix during synthesis of PPy.

3.2 Freestanding PPy films at liquid/air interface using in-situ template

In this section, we present the results of a novel strategy adopted by us to grow nanosheets of the PPy at the liquid/air interface using TPPOH as in-situ template.

3.2.1 Growth process of PPy nanosheets

The concept of the air/liquid interface polymerization is shown in Fig. 2.1. The typical process employed for the growth of free-standing PPy films is as follows. In a beaker, 60 mL of 0.1M aqueous $FeCl_3$ was taken and, in a steady state, 200 µL solutions consisting of 1mM TPPOH and 0.01- 1M pyrrole prepared in dichloromethane (DCM) was slowly dropped using a micropipette. In addition, pure TPPOH and PPy films were prepared by dropping respectively 1mM TPPOH or 0.1M pyrrole solutions into $FeCl_3$. In all the cases, films were spontaneously formed at air/$FeCl_3$ interface. Pure TPPOH films were formed within 5 min, while formation of pure PPy films took more than 20 min. All the films were mechanically strong and were lifted easily onto glass substrates. Prior to the characterization, all the films were thoroughly rinsed using Millipore water. Since TPPOH dissolves in DCM, therefore TPPOH/PPy bilayers were washed using DCM to obtain free-standing PPy films. The formation kinetics of TPPOH/PPy bilayer films was studied by lifting them onto glass substrates from air/$FeCl_3$ interface after various time intervals and washing them using DCM. It was found that no residue was left on glass substrates for films lifted after □10 min and, it is only after this period, PPy films were left on the glass substrate. These results indicated that while TPPOH film is formed very quickly, the kinetics of interfacial polymerization of PPy is rather slow. The PPy films prepared without and with TPPOH would hereafter be referred as PPy-1 and PPy-2, respectively.

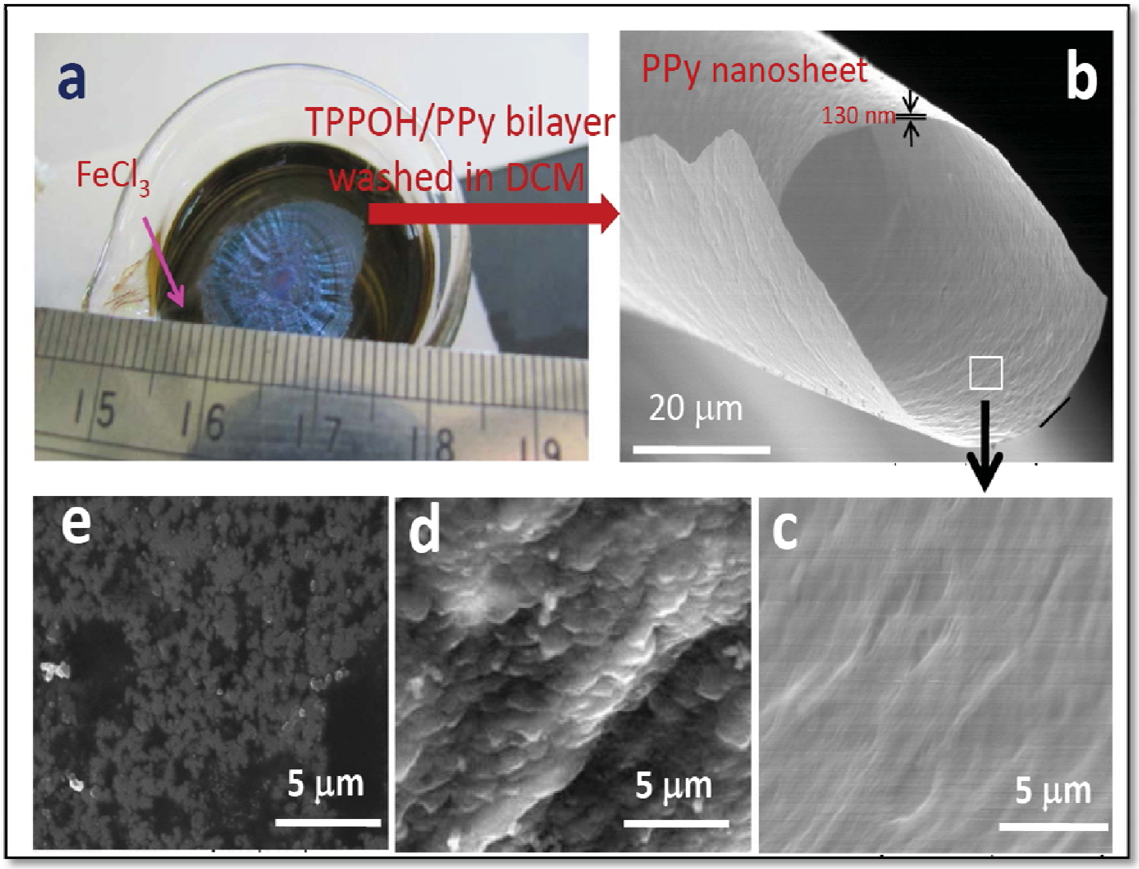

Fig. 3.1: (a) Photograph of the TPPOH/PPy bilayer formed at the air/FeCl3 interface film prepared using 0.1M PPy solution. SEM images: (b) PPy-2 film obtained after washing TPPOH/PPy bilayer in DCM; (c) Magnified image of PPy-2 film; (d) J-aggregate film of TPPOH; and (e) PPy-1 films that is formed without TPPOH.

3.2.2. Morphology of the freestanding PPy films

Fig. 3.1 (a) shows the photograph of the TPPOH/PPy bilayer formed at the air/FeCl$_3$ interface when solution of 1mM TPPOH+0.1M pyrrole was spread onto the surface of

$FeCl_3$ solution. The blue color of the TPPOH/PPy bilayer is due to the characteristic color of TPPOH. The SEM image of PPy sheet (i.e. PPy-2 films) obtained after washing TPPOH/PPy bilayer in DCM is shown in Fig. 3.1 (b). The thickness of the PPy-2 films was found in the range of 120-140 nm and the morphology, as shown in Fig. 3.1 (c), consists of densely packed long PPy nanothreads. The thickness of the nanosheet however could be tailored by changing the pyrrole concentration. It was found that by increasing the pyrrole concentration from 0.01M to 1M, the thickness of the nanosheet increases from 50 nm to 250 nm. However, at very high pyrrole concentrations, the SEM images, as shown in Fig. 3.2, indicate that the film morphology turned to granular, which overlay nanosheets. On the other hand, the morphology of pure TPPOH and PPy-1 films, as shown in Fig. 3.1 (d) and (e), respectively, are remarkably different as compare to that of PPy-2 films. TPPOH films exhibit highly dense morphology that consists of square (size: ~2 µm) and lamellar structure, whereas the morphology of PPy-1 film is porous and granular in nature. In the following we demonstrate that the dense morphology of PPy-2 films as compared to that of PPy-1 films arise due to a template action of TPPOH films.

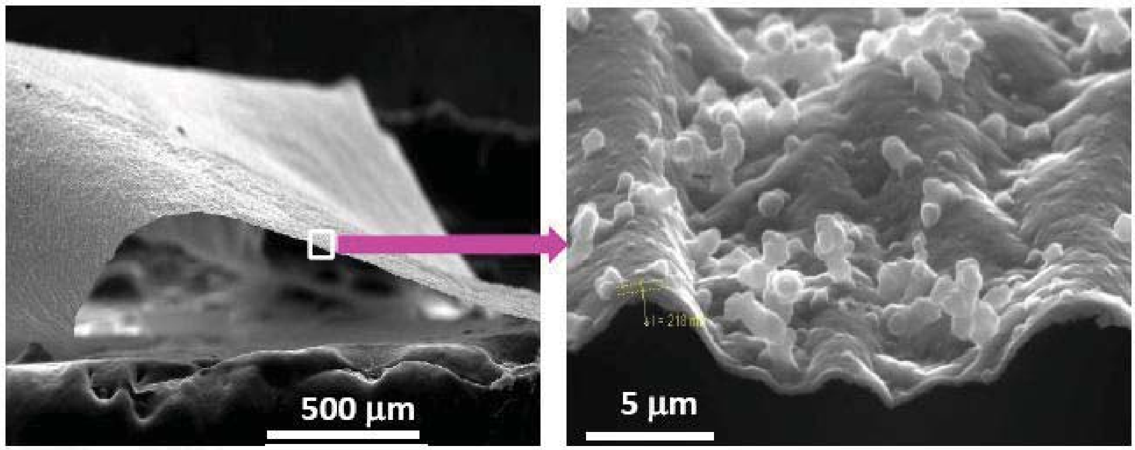

Fig. 3.2. SEM images of PPy-2 film prepared using 1M PPy solutions.

First of all we investigate the origin of dense and lamellar morphology of pure TPPOH films, see Fig. 3.1(d). Aggregation is a well-known phenomenon for molecules with a flat and extended π-electron systems like TPPOH, in which monomeric units stack into edge-to-edge (J-aggregate) and/or face-to-face (H-aggregate) configurations [131]. In order to investigate the type of aggregation in TPPOH, we have recorded the transmission absorption spectra of the TPPOH films and TPPOH monomer solution (prepared by dissolving TPPOH in DCM) and the results are shown in Fig. 3.3. It is seen that the absorption spectra for TPPOH film is relatively broad as compared to that of TPPOH solution, suggesting the occurrence of an incoherent interaction in the surroundings of the dense film. For TPPOH film, the Soret band appears at 466 nm (along with a shoulder at 436 nm) as compared to the 418 nm observed for the free base monomers. Similarly, the weak Q-bands at 514, 549, 588 and 694 nm observed for monomers are replaced by an intense single band at 705 nm. Observed red-shift of both Soret and Q bands confirms the formation of J-aggregates (Note: H-aggregation results in the blue-shift) [132].

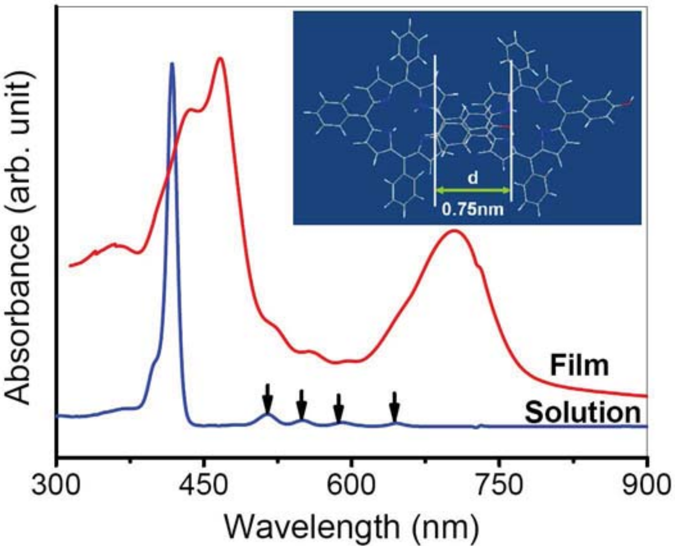

Fig. 3.3: UV-Visible spectra of TPPOH solution in dichloromethane and TPPOH film formed at air/aqueous $FeCl_3$ interface. Inset shows a schematic of the J-aggregate formation, where d is the slipping distance.

In the case of TPPOH film, the J-aggregation possibly occurs due to hydrogen bonding between the hydroxyl group of one molecule (attached at para position of phenyl ring) and N-H bonds at porphyrin core of adjacent molecule, as schematically shown in the inset of Figure 3. The presence of strong high energy absorption shoulder of the B-band (i.e. at 436 nm) - usually assigned to the orthogonal transition dipole to the aggregation axis - suggests that the slipping distance (d) is quite short [132]. Theoretically estimated value of d in the case of TPPOH is found to be 0.75 nm. Therefore, the J-aggregation of TPPOH with small slipping distance can yield lamellar structure as experimentally observed in Fig. 3.1 (d). As mentioned earlier, the TPPOH films are formed within 5 min. and this is attributed to the presence of Fe^{3+}, which is known to induce J-aggregation at a very fast rate [133]. Therefore, it is established that the J-aggregation of TPPOH films occurs at a very fast rate. Considering the experimental fact that formation of pure PPy film (i.e. PPy-1 formed without TPPOH) takes about 20 min, it is apparent that in the case of TPPOH/PPy bilayer, the quickly formed TPPOH film at air/$FeCl_3$ interface acts as an in-situ template for the growth of PPy nanosheets. The template action is obtained as the N-H group of pyrrole rings forms hydrogen bonding with porphyrin core of the J-aggregates, which provides directionality for pyrrole polymerization in the form of nanothreads, as observed in Fig. 3.1 (c). Closely packed nanothreads leads to the formation of a mechanically strong PPy nanosheets.In order to further confirm that J-aggregate film of TPPOH only acts as template and does not incorporate into PPy-2 films, we have recorded the FTIR spectra, as shown in Fig. 3.4. It has been found the FTIR spectrum of the PPy-2 nanosheets is almost identical to that of PPy-1 films, which exhibit all characteristic peaks of polypyrrole [134-136] i.e. antisymmetric (1567 cm-1) and symmetric (1483 cm^{-1}) ring stretching modes, C–N (1313 cm^{-1}), C–C (1408 cm^{-1}), C–H in-plane bending (1196 cm^{-1}), polypyrrole main chain (1040 cm^{-1}) and ring bending vibrations (778 cm^{-1} and 924 cm^{-1}). The absence of peak corresponding to OH - a characteristic of TPPOH- confirms that TPPOH does not incorporate into the PPy-2 films.

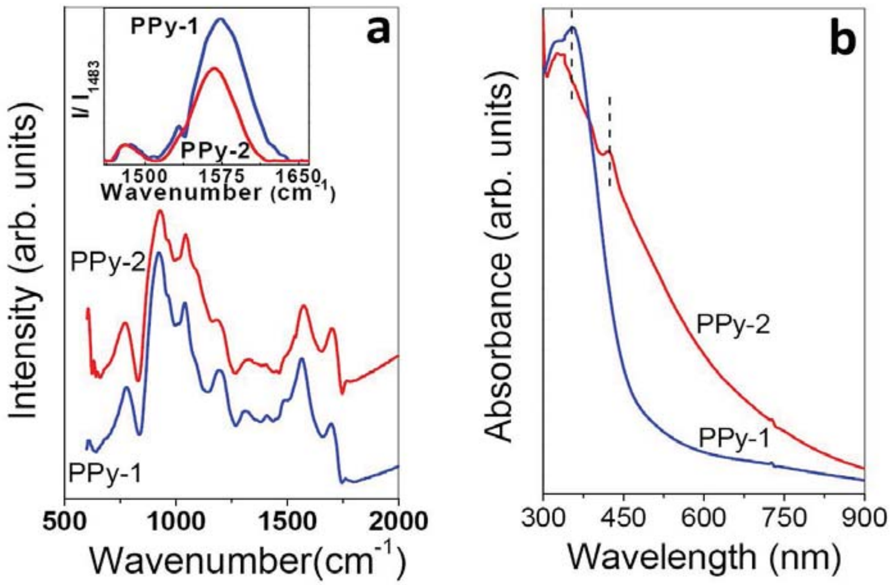

Fig. 3.4: (a) FTIR spectra of PPy-1 and PPy-2 films. Inset shows the FTIR spectra in the 1450-1650 cm^{-1} region with intensity normalized with respect to 1483 cm-1 peak. (b) UV/Vis spectra for PPy-1 and PPy-2 films.

Our experimental results show that PPy-2 films are superior to PPy-1 films in terms of improved conjugation length. First evidence to this comes from the FTIR intensity ratio (I_{1567}/I_{1483}), which is reported to be inversely proportional to the conjugation length [137]. The data presented in the inset of Fig. 3.4 (a), therefore, clearly show an enhanced conjugation for PPy-2 films, which is in accordance with their dense morphology. The second confirmation of improved conjugation length comes from the UV-Vis spectra, as shown in Fig. 3.4 (b). PPy-2 films shows absorption peak at 424 nm (corresponding to the π-π* transition of the PPy chain [138]), while for PPy-1 films the peak occurs at 355 nm. A red-shift in the absorption peak observed for PPy-2 films confirms their enhanced conjugation length. Another notable feature of the UV/Vis spectra is the absence of broad absorption peak at around 600 nm, which has been observed in doped PPy due to the polaron transition [138]. This indicates that both PPy-1 and PPy-2 films are undoped.

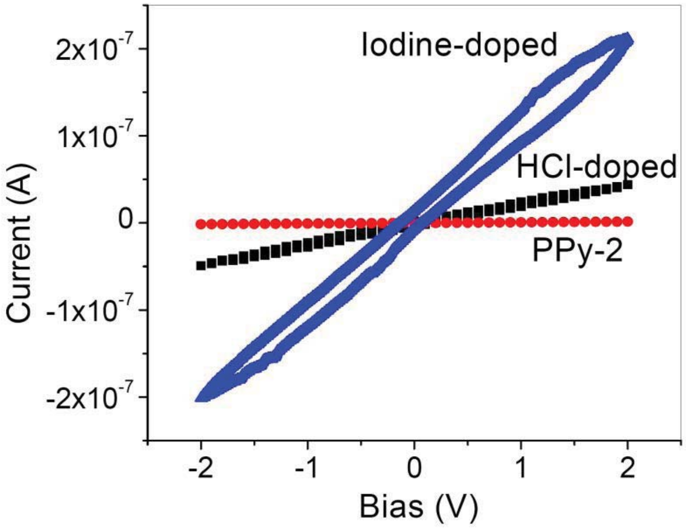

Fig. 3.5: Current-voltage characteristics recorded for the PPy-2 films in pristine state and after doping with iodine and HCl vapors for 1 hr.

3.2.3 Charge transport measurements

(a) Current – voltage characteristics

The results of UV/vis data show that PPy-2 films have higher conjugation length as compared to the Ppy-1 films. In order to further confirm it the room temperature conductivity of both the films were measured and were found 5×10^{-6} and 3×10^{-5} S/cm for PPy-1 and PPy-2 films, respectively. A slightly higher conductivity in PPy-2 films has been obtained, and henceforth, we will focus only onto the PPy-2 films. Typical current-voltage characteristics recorded for PPy-2 films in pristine state and after exposing to iodine and HCl vapors for one hour each are shown in Fig. 3.5. It has been found that the conductivity improves by 30 times on exposing to HCl and ~150 times on exposure to iodine, clearly indicating that conductivity of PPy-2 films can be tailored by appropriate doping. Most importantly, PPy nanosheets showed no change in conductivity when kept in air for more than six months, indicating their stability in air.

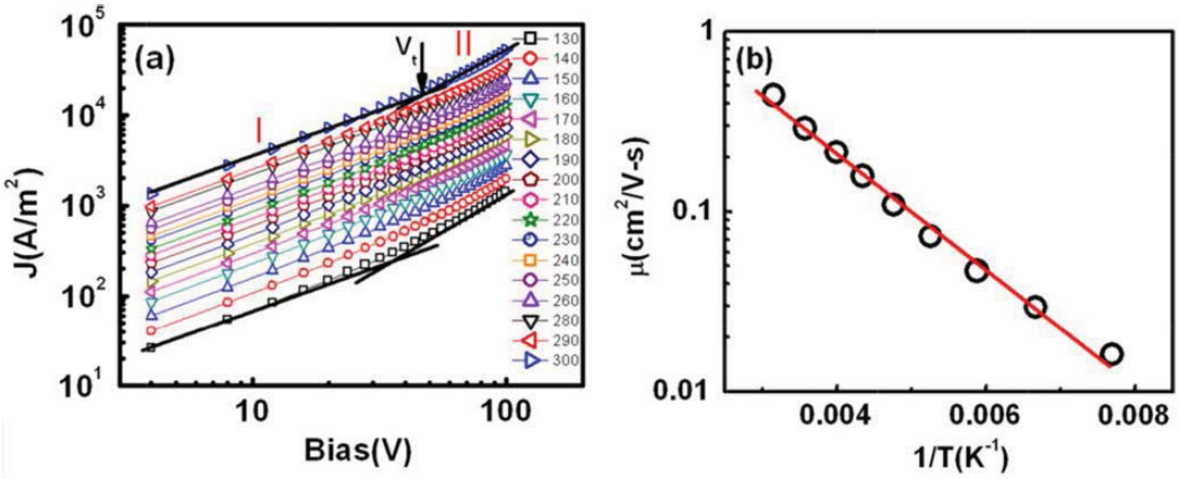

Fig. 3.6: (a) Log-log plots of J-V characteristics in the temperature range 130 - 300K and (b) plot of mobility as a function of 1/T.

In order to further gain insight into the charge conduction mechanism(s), the J – V characteristics for PPy-2 films were recorded up to a bias of 100 V, and the obtained results are plotted in log-log scale shown in Fig. 3.6 (a). Based on the nature of dependence of current on voltage, two distinct regions (marked as I to II) have been identified. In the region I, the slope of the linear fit to data is ~1, indicating an ohmic conduction. In molecular semiconductors, an ohmic conduction normally occurs if the thermally generated carriers exceed that of injected carriers through the electrode, and the J in this case is given by:

$$J = n_0 e\mu E \tag{3.1}$$

where, n_0 is the thermally generated hole concentration, e is electronic charge and µ is the hole mobility. However, the slope value in region II is ~2, indicating that the charge transport is via trap-free space-charge limited characteristics (SCLC). SCLC occurs if the injected carrier density is higher than the thermally generated carrier density and in this case J dependence on applied bias is given as per the relation:

$$J = \frac{9}{8}\varepsilon\mu\frac{V^2}{d^3} \qquad 3.2$$

Where ε is the permittivity of the film and d is the electrode separation [139]. The typical reported value of ε for PPy films is $1.2\text{x}10^{-10}$ Fm^{-1}[140]. Using data of Fig. 3.6 (a), we have calculated the values of n_o and μ. The value of n_0 is determined from the crossover voltage (V_t), as shown in Fig. 3.6 (a) and using the relationship: $V_t = 8n_0ed^2/9\varepsilon$. The estimated value of n_0 at 300K is $2.8 \text{ x } 10^{20}$ m^{-3}, which is in agreement with the reported literature of organic semiconductor films [141]. The μ values at different temperatures were calculated from the slopes of J-V^2 plots. The μvalue at 300K was found to be $5.34\text{x}10^{-5}$ $m^2V^{-1}s^{-1}$. The temperature dependence of μ is plotted in Fig. 3.6 (b), which is found to obey the Arrhenius behavior i.e. $\ln\mu \sim 1/T$.

(b) Low temperature conductivity measurements

As discussed in Chapter 1, the electronic properties of the conjugated polymers are very much dependent on the structural aspects like the orientation, conformation and the chain length. The transport properties are also affected by the defects, disorders and the presence of dopant ions. A decision about the conduction mechanism is often comprehended based on the measurement of the temperature dependence of the conductivity. The temperature dependence of electrical resistivity ρ(T) of the PPy-2 films grown is shown in Fig. 3.7 (a). It clearly shows that the ρincreases with lowering temperature indicating a critical or insulating behaviour of the films in the whole range of investigation. The temperature dependence of the reduced activation energy, described as:

$$W = -\frac{d\ln[\rho(T)]}{d\ln T} \qquad 3.3$$

is plotted in Fig. 3.7(b). Positive, zero and negative slopes of the plot corresponds to the metallic, critical and insulating regimes, respectively. A negative slope for PPy film indicates that it is in the insulating regime.

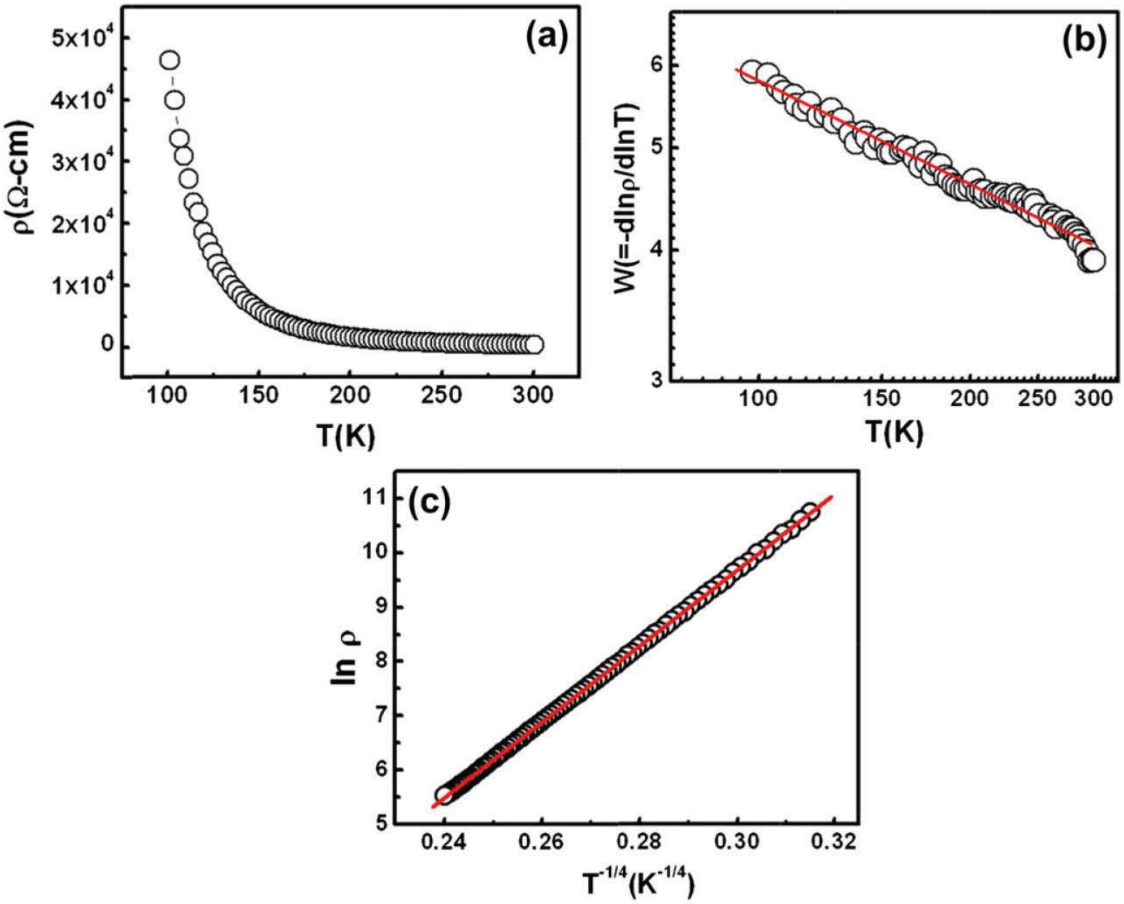

Fig. 3.7: (a) The temperature dependence of the electrical resistivity $\rho(T)$ of the PPy-2 films, i.e. grown using TPPOH template, (b) temperature dependence of the reduced activation energy, and (c) exponential temperature dependence of variable range hopping.

For the sample in the insulating regime of the metal to insulator (M-I) transitions, the low temperature resistivity follows the exponential temperature dependence of variable range hopping conduction (VRH), as observed in Fig. 3.7(c). In this model the resistivity of the disordered material is controlled by the hopping of charge carriers between local states near the Fermi level, as discussed in Chapter-1. When the coulomb interaction between charge carriers is weak and can be neglected, then the Mott-VRH model is applicable. In this case the temperature dependence of resistivity can be expressed as:

$$\rho(T) = \rho(0)\exp(T_0/T)^{\frac{1}{d+1}} \qquad 3.4$$

where, d is the dimensionality of the hopping process, T_0 is the characteristics Mott temperature and is given as:

$$T_0 = \frac{18}{L_c^{\ 3} N(E_F) k_B} \qquad 3.5$$

where, L_c is the localization length, N(EF) is the density of states at the Fermi energy. The typical value of $N(E_F)$ for moderately doped PPy is $2X10^{20}$ $eV^{-1}cm^{-3}$[142]. The average hopping distance R_{hop} is related to the L_c and T_0 by relation:

$$R_{hop} = \frac{3}{8} L_C \left(\frac{T_0}{T}\right)^{\frac{1}{d+1}} \qquad 3.6$$

As seen in Fig. 3.7(c), for pure PPy films the temperature dependence of resistivity is best described by Motts 3D-VRH model with $T_0 = 2.34x10^7$ K. Using $N(E_F)$ as is $2x10^{18}eV^{-1}cm^{-3}$, the estimated L_C and R_{hop} are 16.5 and 103 Å, respectively. The ratio R_{hop}/L_c ~ 6, indicates that in pure PPy films the carriers are strongly localized therefore making it close to the insulating behavior of M-I transition.

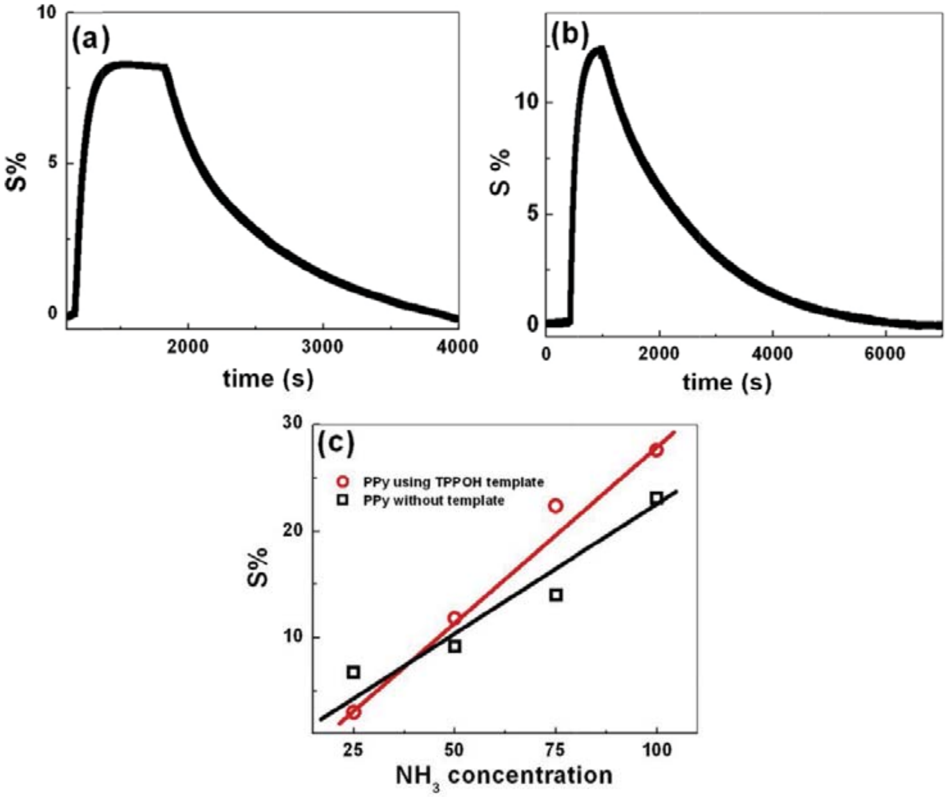

Fig. 3.8: Ammonia response curve recorded for (a) PPy-1 film grown without TPPOH template, and (b) PPy-2 film grown using TPPOH template. (c) Linear dependence of response as a function of ammonia concentration.

3.2.4. Gas sensors

(a) Gas sensing characteristics

Both PPy-1 and PPy-2 films were investigated for their NH$_3$ sensing properties. Under similar concentrations of the starting solutions the thickness of the films was identical. PPy films grown without the TPPOH template suffered from the inherent drawback of poor intergrain connectivity. Hence, it was difficult to get a continuous and uniform PPy-1 film onto the substrates for sensor fabrication as most of them ruptured during transfer. However, one of the successful attempts resulted in a reasonable transfer of PPy- 1film onto the microglass slides and accordingly was investigated along with the

PPy-2 films, which were grown using TPPOH template and had excellent mechanical strength. The response curves recorded for PPy-1 and PPy-2 films are shown in Fig. 3.8. PPy-1 films exhibited a response towards NH_3 only at room temperature. A typical response and recovery times towards 50 ppm of NH_3 were 150 s and 24 min, respectively. Besides, a linear dependence of response on gas concentration upto 100 ppm (S%~23) was observed. These films did not exhibit any response at higher temperatures greater than room temperature. On the other hand PPy-2 films exhibited an enhanced response towards NH_3. A typical response and recovery times towards 50 ppm of NH_3 were 240 s and 50 min, respectively. PPy-1 films have relatively lower response and recovery times because of their porous nature. Both the films exhibited a linear dependence of response on gas concentration upto 100 ppm. For comparison, we have also investigated the gas sensing properties of the PPy-2 films but without the removal of template. As expected these films did not exhibit a response towards NH3 due to the blocking action of TPPOH.

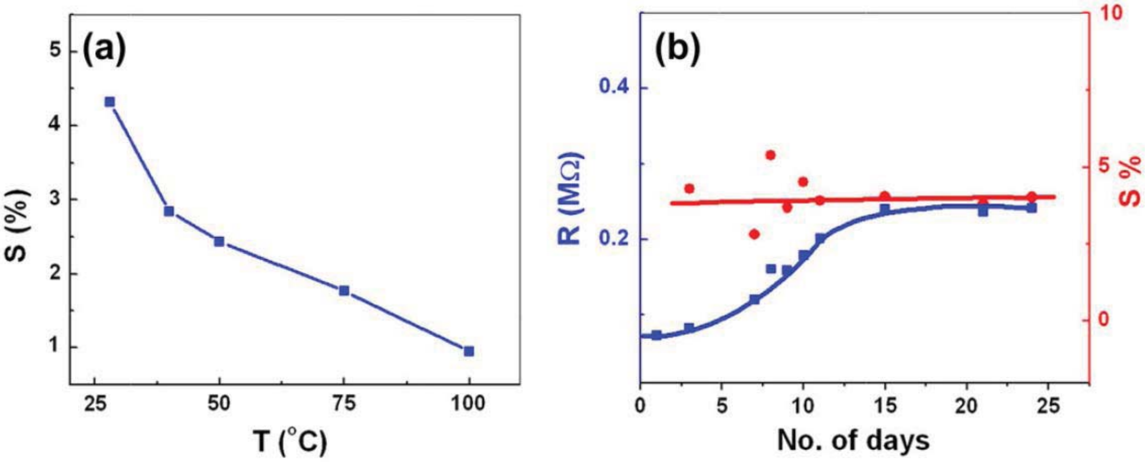

Fig. 3.9: (a) Sensor response as a function of operating temperature for PPy-1 sensor towards 25 ppm of NH_3 and (b) Long term stability measurements for PPy-1 sensors towards 25 ppm of NH_3.

Fig. 3.9 (a) shows the plot of response as a function of operating temperature for PPy-2 films towards 25 ppm of NH_3. The response of these films was found to decrease with increase in the operating temperature with maximum at room temperature. Long term stability measurements performed on these sensors, as shown in Fig. 3.9(b) indicated them to be reasonably stable for over 25 days. The base line resistance changed from 72 to 242 kΩ while no significant variation in the response values was observed.

(b) Sensing mechanism

Ammonia is a kind of electron donating gas and can donate to the initially oxidized PPy sensor film. Exposure to NH_3 has been demonstrated to result in both reversible as well as irreversible processes [143]. The interaction of PPy with ammonia is found to be reversible at low concentrations and short exposure times, whereas long exposure to higher concentrations produces irreversible effects [144]. As is evident from the response curves in the present case interaction of PPy with NH_3 takes place reversibly. The reversible changes have been assigned to compensation effects involving electron or proton transfer. For electron transfer compensation, NH_3 molecule compensates the electrical p-type charge created by the dopant anion molecule

$$PPy^{+}A^{-} + NH_3 \leftrightarrow PPy^{0} — NH_3^{+}, A^{-} \qquad 3.7$$

Similarly, for proton transfer compensation, NH_3 attacks and removes the hydrogen atom attached to the heteroatom of the pyrrole ring via formation of ammonium ion NH_4^{+}. This eventually compensates the p-type charge induced by the dopant anion molecule. The overall effect is that the number of charge carriers on the polymer surface reduces making polymer more neutral causing conductivity to reduce.Now this process is reversible when ammonium ion only binds very weakly to the negative anion facilitating the reverse reaction

$$PPy^{+}A^{-} + NH_3 \leftrightarrow [PPy(—H1^{+})]^{0} + NH_4^{+}A^{-} \qquad 3.8$$

Irreversible changes in polymers are mainly ascribed to the nucleophilic attack of NH_3 molecules on the carbon backbone. This attack introduces defects that shorten the conjugation length of the polymer chain. This leads to increase in disorder and decrease in conductivity as charge transport becomes more dominated by interchain hopping rather than charge transfer along the polymer chain.

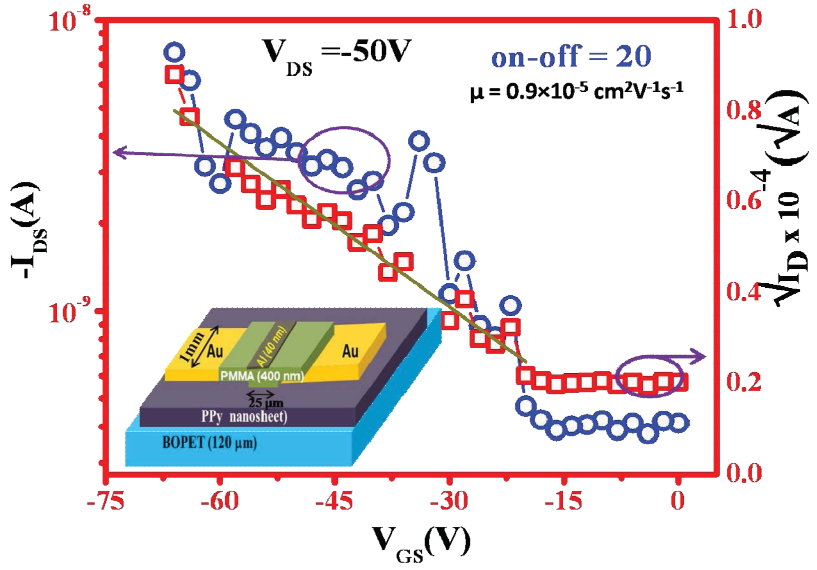

Fig. 3.10: Transfer characteristics of the flexible OFET fabricated using freestanding PPy-2 films. The inset shows the geometry of the devices.

3.2.5. Fabrication of FETs

We present here the first ever made field effect transistors using freestanding PPy-2 films using the top contact top gate geometry, as schematically shown in the inset of Fig. 3.10. For this purpose, PPy-2 nanosheet was lifted on BOPET substrate so that there is no wrinkle on nanosheet which would otherwise make poor interface with dielectric. Source-drain electrodes were deposited by thermal evaporation of gold with channel length and width of 25μm and 1mm, respectively, using shadow mask. For dielectric deposition, poly(methylmethacrylate) (PMMA) solution in PGMEA (propyleneglycolmethyletheracetate) (80mg/ml) was spin coated with 1000 rpm for 80 s on source-drain deposited PPy followed by an annealing at 130°C for 30 min. After that Al was deposited on PMMA layer by thermal evaporation for gate contact. For measurement of the capacitance of the dielectric layer, an Al/PMMA/Al(BOPET) sandwich structure was fabricated by depositing Al electrode (area: 0.025 cm2) onto PMMA coated Al(BOPET).

Typical transfer characteristics were measured at constant drain voltage of -50V, and the obtained result is plotted in Fig. 3.10. It may be noted that these transfer characteristics are not very good, and requires further optimization. The on-off ratio of the device was found to be ~20. The charge carrier mobility was calculated from the slope of the square root of the drain-source current as a function of the gate-source voltage i.e. $\sqrt{|I_{DS}|}$ vs. VGS plot, as shown in Fig. 3.10. The mobility value obtained was 0.9×10^{-5} $cm^2V^{-1}s^{-1}$. Though we were not able to measure the output characteristics the modulation in drain current by application gate voltage shows that these films can be used for OFET applications by further improving the interface with dielectric.

3.3 Freestanding PPy films via acidic oxidation of terpyrrole at air/liquid interface

In this section we discuss another innovative method offormation of PPy films at air/liquid interface via acidic oxidation of terpyrrole.

3.1 Formation mechanism

The experimental procedure followed was as follows. 20 mL hydrochloric acid (18%) solution was slowly poured into beaker containing 20 mL of 0.1M pyrrole solution in dichloromethane (DCM) kept in a 50 mL beaker. The whole reaction mixture was kept stationary and it was observed that with passage of time, the colour of acid phase progressively changed from transparent to yellowish to dark black, as shown in Fig.3.11 (a). After a period of five days a solid thin film forms at the air-aqueous interface. The interface between HCl and pyrrole liquids was kept stationary for several days, as shown in Fig.3.11 (a). It was observed that with passage of time, a solid film forms at the liquid/liquid interface, and also the color of acid phase progressively changed from transparent to yellowish to dark black, see Fig. 3.11 (a).

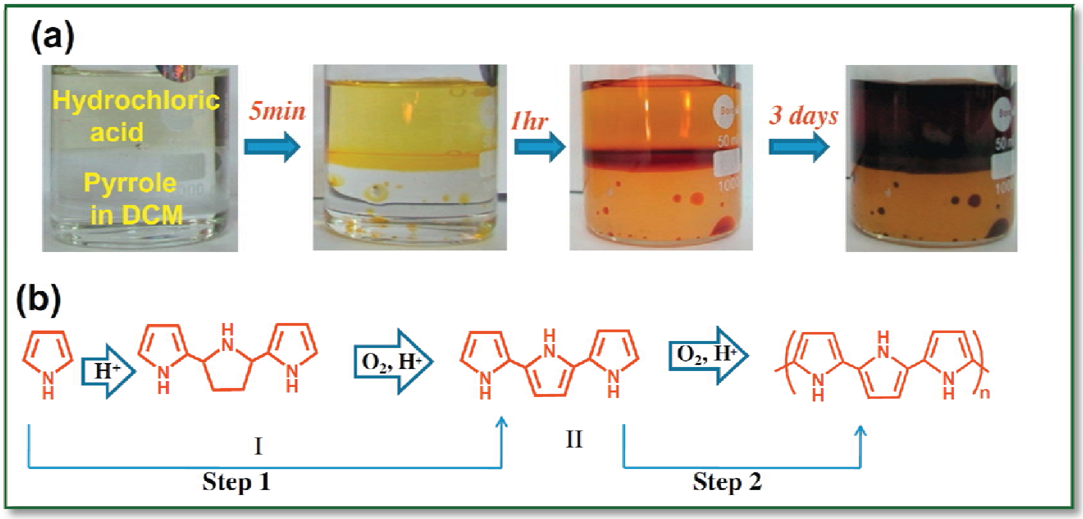

Fig. 3.11: (a) Photographs of the evolution in color of acid/ pyrrole in dichloromethane (DCM) interface during polymerization with time. (b) The scheme of the reaction mechanism of polymerization which is a two steps process.

Fig. 3.11(b) illustrates the main two steps that are involved in the interfacial polymerization and film formation. The first step is considered to be formation of the trimer (I) at the aqueous/organic interface. The mechanism of trimer(I) formation is believed to involve: (i) protonation of pyrrole at 3-position to give strong electrophilic cation first which then attacks an unprotonated pyrrole to form 2-(2,3-dihydro-1H-pyrrol-2-yl)-1H-pyrrole (dimer-I), (ii) further protonation of dimer-I and subsequent electrophlic attack on unprotonated pyrrole leads to formation of trimer (I). The formed trimer (I) migrates slowly towards air-liquid interface. In the second step, terpyrrole (II) is formed in aqueous phase by aerobic oxidative dehydrogenation of the central ring of trimer (I) and polymerized by aerobic oxidation to PPy at air-water interface.

The proposed mechanism for progress of polymerization was supported by investigation of progress of reaction by UV-Visible spectroscopy. Fig. 3.12 shows the UV-Visible spectra of aqueous phase solution (taken after 5 min) and the PPy freestanding film. The presence of absorption bands at 217nm and 319nm in reaction mixture spectrum confirms that polymerization proceeds through formation of two intermediates: 2,5-Bis(2-pyrrolyl)pyrrolidine (I) (λ_{max}=217nm) and 2,2': 5',2''-terpyrrole (II) (λ_{max}=319nm) [145]. Presence of very low intensity band at 476 nm in reaction mixture spectrum reveals that polymerization starts as soon as terpyrrole (II) is formed in presence of air dissolved in aqueous phase. After the polymerization self assembly of PPy chains at air-liquid interface leads to the formation of freestanding PPy film. Since the film formation takes nearly five days, this implies a very slow kinetics of the film formation. To prove that oxygen is essential for polymerization, reaction was carried out under argon atmosphere and it was found that there was no film formation at air-aqueous interface even after 10 days. The reaction was carried out by varying the HCl concentration and it was found that apart from thickness of the film increases with the increase in HCl concentration (shown in Fig. 3.12 (b)).

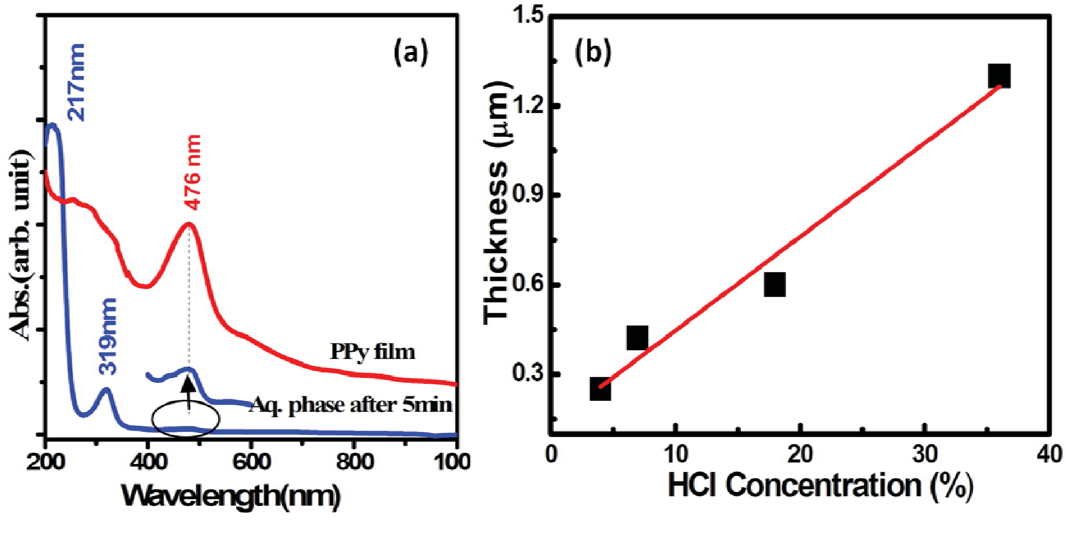

Fig. 3.12: (a)UV-Vis spectra of aqueous phase recorded after 5minitues and polypyrrole film after 5 days. (b) Variation of thickness as a function of concentration of HCl.

The inset (I) in Fig. 3.13(a) shows the photograph of PPy film. The film is about 1 inch diameter, suggesting that this method allows growth of higher diameter films. For characterization, the film formed at the interface was lifted onto a substrate, such as glass, PET, etc., then the film was rinsed with double distilled water followed by repeated cleaning using DCM to remove the traces of hydrochloric acid and unpolymerized pyrrole and oligomers, respectively. The SEM image (II), as shown in Fig. 3.13(a), indicates that the film is highly dense and gets folded. The thickness estimated from the SEM cross-sectional analysis was found to be ~ 600 nm. It was found that the thickness of the films is directly proportional to the HCl concentration. However, the dense morphology of the PPy films was not affected by the HCl concentration. Therefore, this method allows synthesis of dense freestanding PPy films with controlled thickness. The dense morphology of the film is also evident from AFM image (III) of the PPy film (inset of Fig. 3.13 (a)). The UV-Vis spectrum shows the absorption peak at 476 nm which confirms the formation of PPy, as shown in Fig. 3.13 (IV). However, the broad peak at 290 nm in the spectrum indicates the polymerization of terpyrrole along with the formation of polypyrrole.

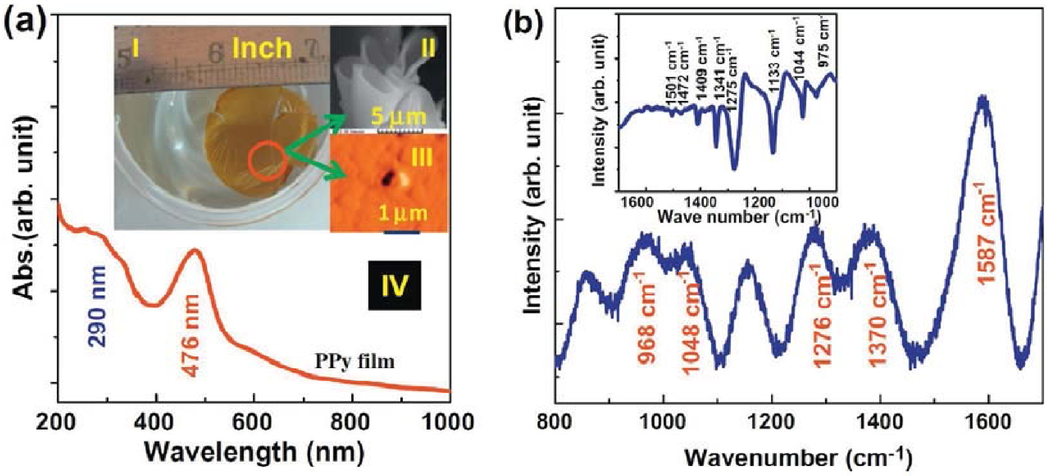

Fig. 3.13: (a) Photograph of ~ 1 inch free-standing polypyrrole film. II and III are the SEM and AFM images. IV. UV-Vis spectrum of polypyrrole film showing characteristics absorption peaks.(b) Raman spectrum of the film. The inset shows the FTIR spectrum. The characteristics peaks are marked on the spectra.

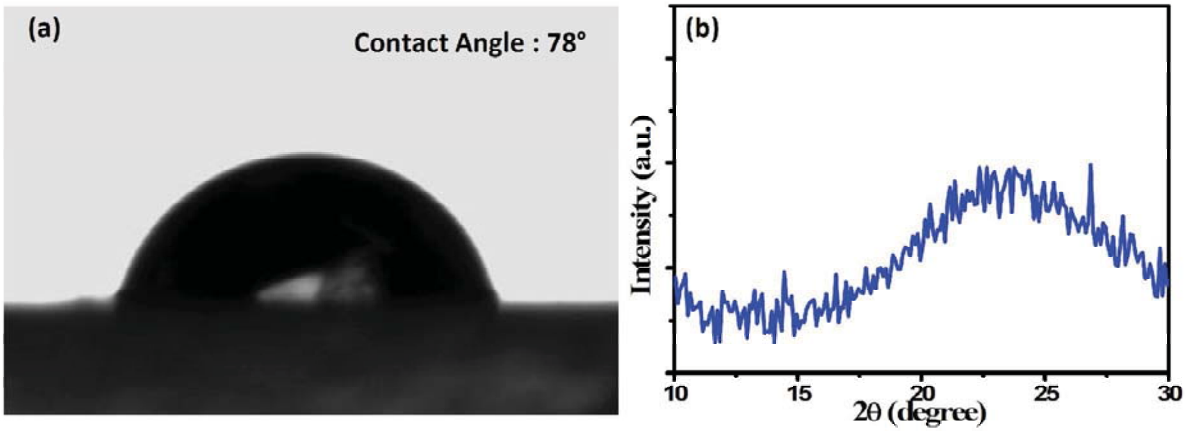

Fig. 3.14: (a) Water contact angle and (b) XRD spectrum of the PPy film.

The formation of PPy film was independently confirmed by Raman and FTIR spectroscopic studies as shown in Fig. 3.13(b). The spectra show the characteristic peaks of PPy at 1587cm^{-1}, 1501cm^{-1}, 1472 cm^{-1}, 1409 cm^{-1}, 1370 cm^{-1}, 1341 cm^{-1}, 1275 cm^{-1}, 1133 cm^{-1}, 1048 cm^{-1}, 1044 cm^{-1}, 975 cm^{-1} and 968 cm^{-1}[146]. The presence of peaks at 2990 cm^{-1}and 2882 cm^{-1}in FTIR spectra confirm the non-conjugated groups present in the polymer matrix (this will be discussed in detail later). To see the surface hydrophobicity of the film, contact angle measurement has been measured, as shown in Fig. 3.14(a), and found to be 78°. This indicates that film surface is hydrophobic in nature. The X-ray diffraction spectrum of the film, as shown in Fig. 3.14(b), shows a broad hump at ~23-24^{o} and this indicates the amorphous nature of the PPy film.

3.3.2 Current-voltage characteristics and memory effect

For current-voltage (I-V) characteristics of the PPy film, two gold electrodes with 12 micron separation were deposited by thermal evaporation. The I-V characteristics, as shown in Fig. 3.15(a), exhibit large hysteresis along with negative differential resistance (NDR) regions (i.e. decrease in current with increasing bias). It may be noted thatI-V characteristics measured in inert atmosphere and under dark condition exhibited similar hysteresis with current peaks (inset in Fig. 3.15(a)). The conductivity of the film is found to be ~10^{-7} S cm^{-1}, which almost two orders of magnitude lower than those synthesized using TPPOH template.

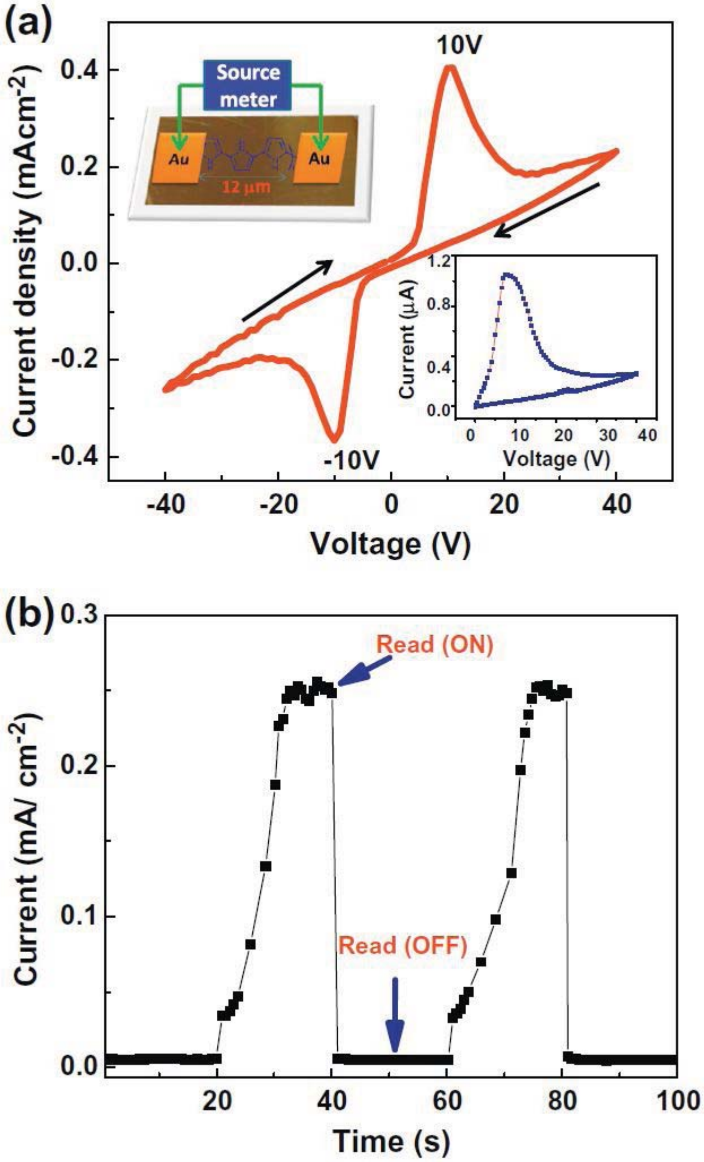

Fig. 3.15. (a) Electrical characterization of polypyrrole film. Left inset (top) shows the measurement setup and the right inset (bottom) shows the I-V plot measured in inert and dark environment. Arrows indicate the direction of voltage cycle. (b) Read current density measured at 6V during SET- read- RESET- read sequence.

The large hysteresis in the I-V characteristics implies that the current has two values (i.e. two conducting states) for a particular bias, which indicates the bistability of the films. This bistable behavior can be used for the demonstration of resistive memory effect. In Fig. 3.15(b), memory phenomenon is demonstrated under 'SET-read-RESET-read' operations. In such sequence of cycles, the high- conducting ('SET') and low-conducting ('RESET') states are induced repeatedly and the statesare monitored ('read') in between. The bias of -10V and +30V for 5 minutes were applied to SET the high conducting state and RESET to a low-conducting one, respectively and these states were monitored ('read') by measuring current at 6V for 20s. While reading the states, current increases and become constant after five second. The on/off ratio is ~50, which slightly decreases with increasing cycles. Furthermore, we also investigated the stability of SET states after applying negative write voltage. We observed that unless opposite polarity voltage pulse was applied, the film remained in SET states for months at ambient condition. However, once the peak current was measured, the current became low (RESET). Thus these behaviors match with read-once memory (ROM).In literature, the origin of current peaks in I-V characteristics is traced to redox properties of polymers which are confirmed by using CV [147, 148]. The CV of PPy free-standing film measured at 0.1 Vs^{-1} and 0.5 Vs^{-1} were capacitive in nature with no redox peaks which confirm that electrochemical phenomenon is not involved in the I-V of the PPy film (Fig. 3.16(a)). Another common mechanism of resistive memory is the changes of the conduction states under bias due to metal filaments formed during deposition of metal electrodes on the polymer [149]. However, this mechanism can be ruled out in the present case because metal electrodes were deposited in plane. Further, similar I-V characteristics were observed in sandwiched structure where bottom contact was Al and Au was the top contact (inset in Fig. 3.16(a)). Therefore, it is essential to understand the electrical components in the film which can be studied by frequency response analyses (FRA). The impedance of polymer film arises from the following elements: resistance due to metal polymer interface (Rp), diffusion of charge through the film to maintain electrical neutrality – which manifests as Warburg impedance (W) at low frequency region in FRA analysis, and capacitance of film between two metal electrodes (Cg) [150]. In present studies, the Nyquist plot of imaginary impedance (-Z′′) vs real impedance (Z′) of the PPy shows two semi circles, one at high frequency and other one at low frequency along with Warburg impedance at low frequency.

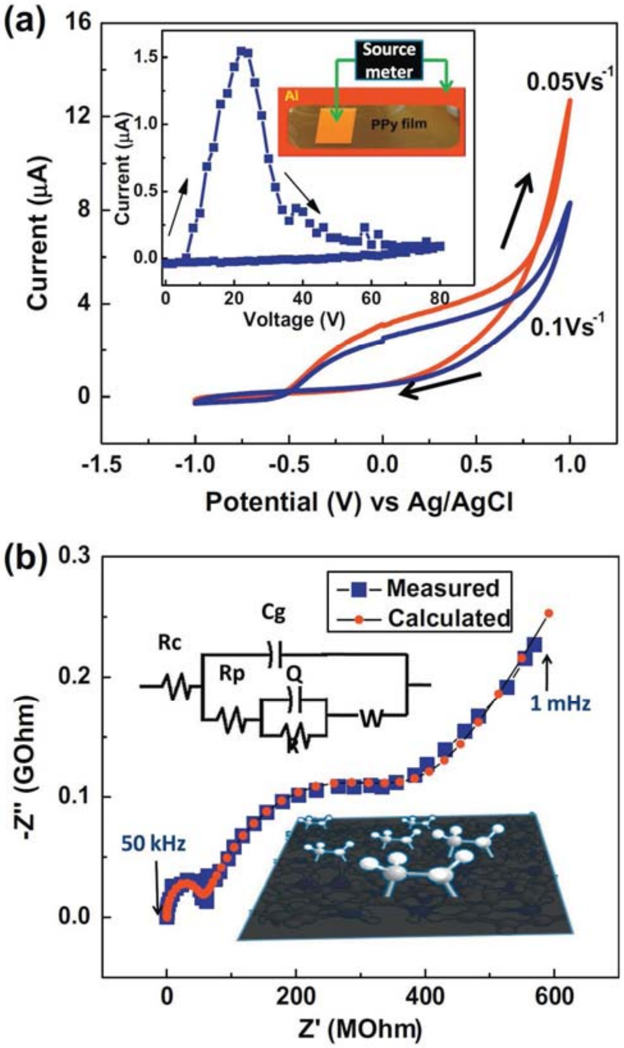

Fig. 3.16: (a) Cyclic voltammetry of polypyrrole film recorded at 0.1 Vs^{-1} and 0.05 Vs^{-1}. Inset shows the I-V characteristics recorded across the film using Al bottom contact and gold as top contact and the device structure. Arrows indicate the direction of potential and voltage scans. (b) Measured and fitted Nyquist plots of imaginary impedance (Z”) vs real impedance(Z′) at 0 V. Top inset shows the equivalent circuit and bottom inset is the visualization of non-conjugated polymer chain in PPy matrix.

Fig. 3.16(b) shows the measured and fitted Nyquist plot to the equivalent circuit (left inset), which contains contact resistance (Rc),Cg, Rp, constant phase element (CPE) (Q) , R, W. The best fitted values of these parameters to the circuit elements are presented on Table 3.1). The QR element indicates the presence of additional capacitance in the PPy matrixbecause Q is attributed to capacitance dispersion. This Q element could be related to defects that present in the PPy film. These defects in the film may be due to the existence of non conjugated terpyrrole polymer in the PPy matrix as discussed above. Since terpyrrole unit contains pyrrolidine moiety, a non conjugated unit, the moiety lies perpendicular to the PPy back bone as depicted in the right inset in Fig. 3.16(b) for visualization. As discussed earlier, such non-homogeneity in conjugated polymer matrix acts as intrinsic dynamic charge trapping. Moreover, the trapped charge causes structural disorder at the trap site for example, in n- hexane film deposited on Ag surface and in polythene film, self trapping of electrons create distortion of chain [151, 152]. The distortion of chain has been demonstrated and investigated by both experimentally and theoretically. Now if defects control the I-V of PPy film, terpyrrole polymer which act as a capacitor (Q) in the polymer matrix, would be expected to be charged during voltage cycled.

Table 3.1 The best fitted values of various parameters to the circuit elements shown in the inset of Fig. 3.15 (b).

Voltage (V)	Contact resistance (Rc), kΩ	Capacitance (Cg), nF	Resistance (Rp), MΩ	Frequency power (n)	CPE (Q), S s^n	Resistance (R), MΩ	Warburg impedance (W), S $s^{1/2}$
0	1.5	0.2	5.3	0.65	4.0×10^{-8}	30.3	3.7×10^{-7}

Since polymer is a soft matter, one would expect the effect of the charging on the conformation and the effect can be investigated using UV-Vis and FTIR spectroscopy studies. Fig. 3.17 shows FTIR spectra of the film at two states SET and REST. We observed that at SET state, the band related to pyrolidine unit at 2982 cm^{-1} which is attributed to C-H stretching is shifted by 8 cm^{-1} and the band at 3450 cm^{-1}, stretching frequency of N-H is got broad (left inset in Fig. 3.17). Furthermore, the broad peaks of C-H stretching (3000 to 2800 cm^{-1}) indicate the random distribution of terpyrrole moieties in the matrix. However, the characteristics peaks of PPy in the range from 900 to1700 cm^{-1} are not affected. The UV-Vis spectroscopy studies of the film at two states, SET and RESET, reveal that the signature peak of PPy at 476 nm peak is not affected by applied bias as expected, but the peak at 290 nm related to terpyrrole polymer gets sharpen at SET state (right inset in Fig. 3.17).

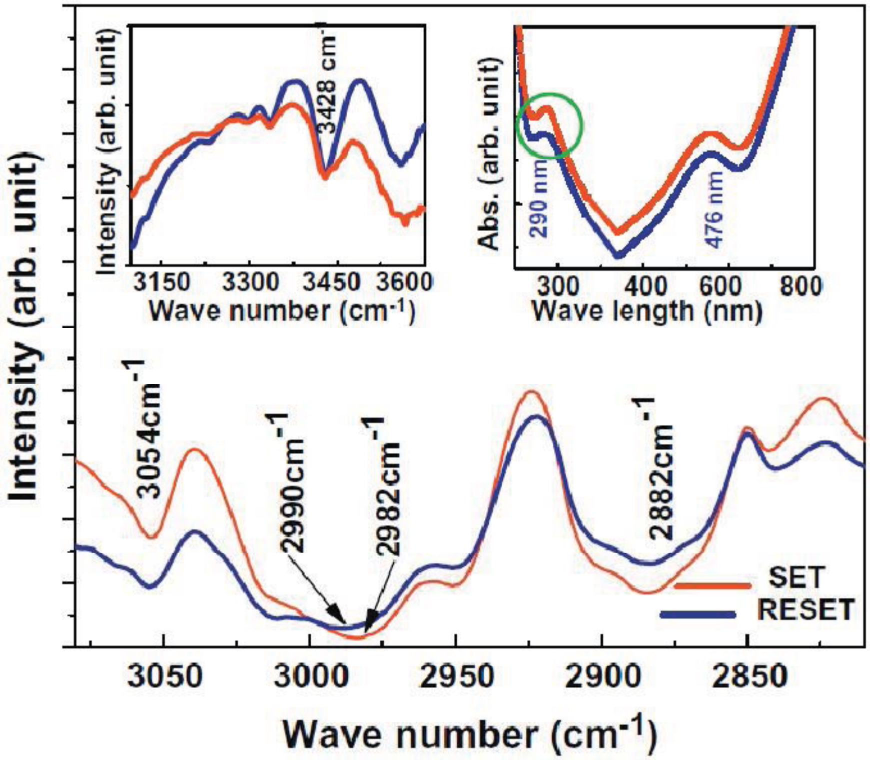

Fig. 3.17: FTIR spectra (range 3100 to 2800 cm^{-1}) of the PPy film at SET and RESET states. Right inset shows FTIR spectra in the range 3100 to 3500 cm^{-1}. Left inset shows UV-Vis spectra of the film at SET and RESET states. Characteristics peaks are assigned on the spectra.

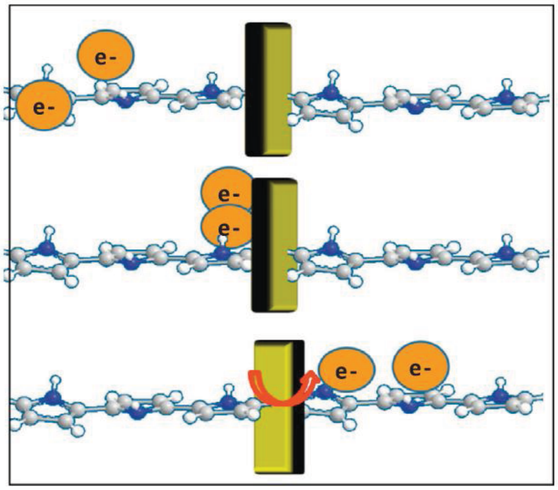

Fig. 3.18: Pictorial representation of charge trapping. (a) Orange circles represent electrons transporting through molecular network (represented polymer chain), and (b) get trapped at solid block (trap site due to nonconjugated chain). (c) De-trap of electrons under applied bias. Arrow indicates the rotation of solid block.

These studies validate that memory effect in polypyrrole film is due to the conformational changes of non conjugated chains in the polymer under bias. The effect of conformation changes were also studied by applying constant negative voltage for 600 s. The measured current shows the rise in current at the beginning but current drops afterwards which leads to peak in the current time measurements. Further, we observed that the current did not increase even the voltage applied after 600 s. This can be explained from charge transport through defect- polymer matrix. During the charge flow, the electron has to transport through conjugated chain, here PPy, then it would face block at defect states created by non conjugated terpyrrole polymer. At the defects states electrons accumulate (charging) until a change in conformation occurs (as investigated by spectroscopy technique). Once conformation is changed, electrons diffuse out (discharging) and current start decreasing and attain low current. This transport mechanism is shown in Fig. 3.18, where the molecular network represents polymer, the solid block represents the defect, solid ball represents the electrons diffusing through polymer chain and getting blocked until the solid block rotated (here by rotation we show the change of conformation). Similarly, when polarity of voltage is changed, the current rises until conformations reset. This dynamic localization of charge explains two current peaks in opposite direction in I-V characterization. We further observed that the peak current in positive direction increased with the increase of applied negative voltages up to -40 V (Fig. S6). This shows that the change in conformation depends on the applied electric field and can withstand -40 V. Moreover, as discussed above SET or RESET state was stables for months; thus, the conformational changes are not affected by ambient temperature which leads to non volatility in the memory. In addition to these, we observed that current peak positions increase with increase of the gap between two metal electrodes, for instant, current peak positions are at 10 V, and 30 V for 12 micron and 500 micron gap between metal electrodes, respectively. This explains the dependence of I-V current peak position on electrode design. Thus the proper designing of the metal electrodes would help to reduce the operating voltage. Since the PPy film is resistive to common organic solvents like acetone, isopropanol, methanol and acids, the electrode designing can be carried out using present lithographic techniques.

3.4 Conclusions

We have synthesized freestanding polypyrrole films via interfacial polymerization at air/liquid interface using two different simple innovative methods.

In the first method freestanding polypyrrole nanosheets were grown at the air/liquid interface by dropping pyrrole+TPPOH solution into aqueous $FeCl_3$ solution. Experimental results show that in which TPPOH spontaneously forms J-aggregation due to hydrogen bonding between the hydroxyl group of one molecule (attached at para position of phenyl ring) and N-H bonds at porphyrin core of adjacent molecule. These J-aggregates act as an in-situ template for the growth of dense PPy films. The conductivity of these freestanding films was of the order of 3×10^{-5} S/cm, which significantly improved after doping with iodine. The current-voltage characteristics of these films were non-hysteretic. The temperature dependent resistitivity measurements showed the variable range hopping as the mechanism of charge conduction in these films. The charge carrier mobility of at 300K was found to be 5.34×10^{-5} m^2/V-s, which exhibited an Arrhenius like temperature dependence. These freestanding PPy films were found to be responsive to the NH_3 gas. We have made an attempt to fabricate the field effect transistors using these freestanding PPy films as active channel, and demonstrated the transfer characteristics. However, the films are mechanically not so strong to sustain the device fabrication steps, and therefore, require further investigations to improve the mechanical stability of these films.

In the second method, freestanding polypyrrole films are synthesized by the acidic oxidation of terpyrrole at the air/water interface. In this case, non-conjugated polymer chains are incorporated into polypyrrole films during synthesis. These freestanding polypyrrole films show large hysteresis in current-voltage characteristics along with a negative differential resistance effect. The hysteric behaviour has been utilized to demonstrate the rewritable memory effect, which has been attributed to the conformational changes of non-conjugated polymer chains in the polypyrrole matrix.

Chapter -4

Flexible Ag/polypyrrole nanocomposite films

In this Chapter, we describe synthesis of polypyrrole-silver (PPy–Ag) nanocomposite films on a N-(3-trimethoxysilylpropyl)pyrrole modified biaxially oriented polyethylene terephthalate (BOPET) substrate by photopolymerisation of pyrrole using $AgNO_3$ *as a photo-initiator. With increasing* $AgNO_3$ *concentration or with increasing polymerisation time, the film morphology shows a transition from two dimensional lamellar to granular structures. The films are adherent, flexible and exhibit room temperature electrical conductivity of ~15 S* cm^{-1} *(for* $AgNO_3$*~ 0.5 M, 120 min of UV exposure). However, the films directly prepared on pristine BOPET show granular morphology and their conductivity value is relatively low ~0.5 S* cm^{-1}*. The high conductivity of PPy–Ag films is attributed to the high conjugation length, the incorporation of Ag nano-particles between the polypyrrole chains and the ordered structure due to the templating effect of the silanisedpyrrole layer. The films were also investigated for theirgas sensing characteristics.*

4.1. Introduction to nanocomposite films

Conducting polymer–metal nanocomposites are a new class of materials, which provide the possibility to design devices with a new functionality, where the best of both organic and inorganic can be utilized [153-155]. Different approaches have been used to prepare conducting polymer–metal nanocomposites in the form of metal nanostructures covered with a polymer shell or vice versa, or nanostructures embedded in the polymer matrix[156-158].As discussed in Chapter 1, among various conducting polymers, polypyrrole (PPy) is widely sought-after, due to its excellent stability under environmental conditions, good conductivity and biocompatibility [125, 159]. In the literature various combinations of PPy with metals such as PPy–Ag, PPy–Au, PPy–Pt and PPy–Cu etc. have been reported[160-164]. In particular, PPy–Ag nanocomposites are gaining considerable attention because of their extraordinary physicochemical properties, arising due to their high surface area and the quantum size effect, as well as potential applications in electrocatalysis, chemical sensors and electrode materials for various device applications[165, 166]. PPy–Ag nanocomposites in powder or thin film form have been prepared by several strategies:

(i) using the monomer or polymer as a reducing agent for the metal, which results in a nanocomposite powder or film [161, 167, 168]
(ii) chemical polymerization of PPy around the Ag particles or dispersion of the Ag nanoparticles in a polymer matrix [169-172]
(iii) Interfacial polymerization at the water–ionic liquid interface under ultraviolet light [173].

As discussed in the Chapter 1, our focus of the thesis is to synthesize, flexible conducting polymer films and nanocomposites. As discussed in Chapter-3, interfacial polymerization though yields good flexible freestanding PPy films, but fabricating devices like gas sensors and field effect transistors require a support, as the freestanding films are mechanically not so strong to tolerate all the fabrication steps. Therefore, in order to make mechanically strong flexible nanocomposite films, we have deposited PPy-Ag nanocomposite films on flexible bi-axially oriented polyethylene teraphthalate (BOPET) substrates using photopolymerisationprocess.

4.2. Photopolymerization of flexible nanocomposite films

Our process of fabricating the adherent PPy-Ag nanocomposite films onto BOPET consists of three steps: (i) Hydroxylation of BOPET surface; (ii) Silanization of OH-terminated BOPET surface by self-assembly; and (iii) Photopolymerizationof PPy–Ag nanocomposites onto the silanised BOPET.

4.2.1 Hydroxylation of BOPET surface

BOPET substrates were ultrasonically washed with chloroform and ethanol for 30 min, then dried for 4 h at 70°C in an oven. BOPET was hydroxylated by dipping it in the potassium hydroxide (KOH)-containing dimethyl sulphoxide (DMSO) solution (4 mg KOH dissolved in 30 ml DMSO). The sheets were left to react with KOH for 30 min, then thoroughly washed in distilled water and dried.

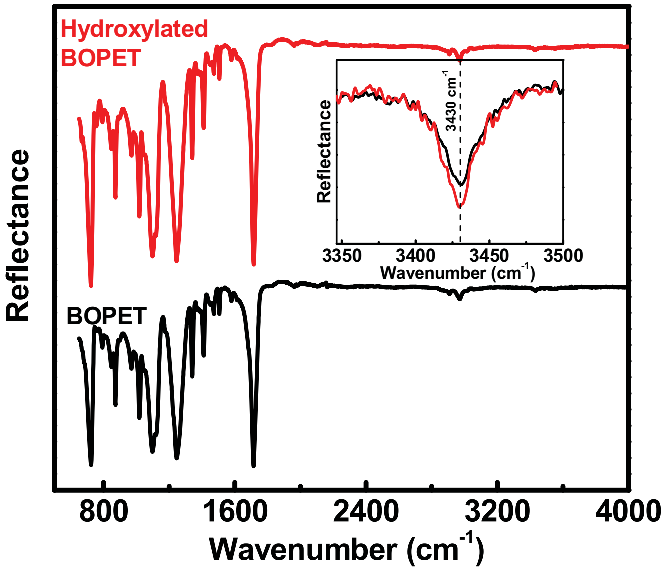

Fig. 4.1: ATR-FTIR spectra of the pristine and hydroxylated BOPET substrates.

The presence of OH groups at the surface was confirmed by the contact angle and FTIR data. For our clean BOPET surface the experimentally observed contact angle for distilled water was found to be 70°, while after hydroxylation the contact angle was reduced to 30° [174-176]. Fig. 4.1 shows the ATR-FTIR spectra of the pure and KOH treated BOPET substrate in the wavenumber region from 600 to 4000 cm^{-1}. The spectra have the characteristic absorption peaks at 1712 cm^{-1} (C=O bonds), 1410, 1018, and 872 cm^{-1} (vibration of aromatic ring), 1340 and 1177 cm^{-1} (bending vibration of $–CH_2$ groups), 1244 and 964 cm^{-1} (stretching vibration of C–O bonds), 1124 and 1100 cm^{-1} (stretching vibration of C–O bonds due to the amorphous and crystalline structures of BOPET, respectively) [177]. The absorption bands at 3430 and 2970 cm^{-1} correspond to the O–H and C–H (antisymmetric) stretching modes of BOPET, respectively. As seen from the inset of Fig. 4.1, on hydroxylation of BOPET, there is a particular enhancement in the O–H intensity (when normalized with respect to C–H intensity) [174-176]. It confirms that after KOH treatment of BOPET, there is a substantial increase in the number of OH groups at its surface.

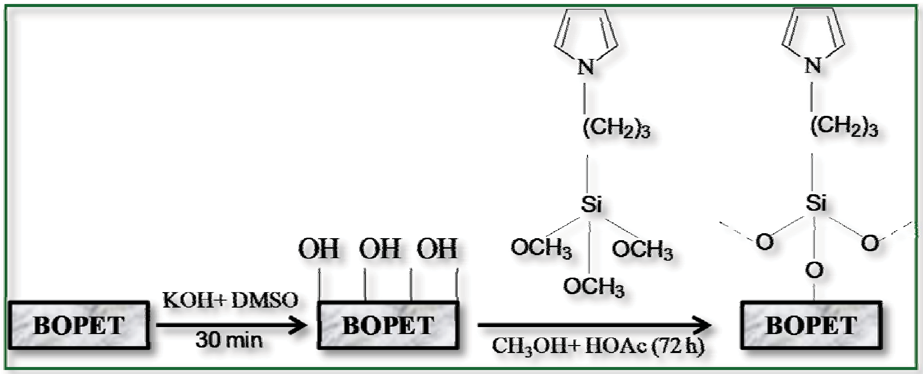

Fig. 4.2: Scheme showing the surface modification of BOPET substrate by N-(3-trimthoxysilylpropyl)pyrrole.

4.2.2 Silanization of OH-terminated BOPET surface by self-assembly

Surface modification of BOPET substrate was carried out by grafting of N- (3-trimethoxysilylpropyl)pyrroleusing self-assembly. For this purpose, hydroxylated BOPET sheets (as prepared in the first step) were dipped into a silanisedpyrrole solution (115 mg in 25 ml ethanol and 1 ml acetic acid) and left to react for 72 hr. After this the substrates were thoroughly cleaned using ethanol and dried for 2 hr at 70 °C in an oven.

The scheme for grafting of the silanisedpyrrole layer at the hydroxylated BOPET surface is shown in Fig. 4.2 [178]. The actual mechanism of the general silanisation process takes place in four steps. The first step is physisorption, in which the silanisedpyrrole molecules get physisorbed at the hydroxylated BOPET surface. In the second step the silane head-groups arriving close to the substrate hydrolyse—in the presence of the adsorbed water layer (inherently present) on the surface—into highly polar trihydroxysilane ($Si(OH)_3$). These polar $Si(OH)_3$ groups form covalent bonds with the hydroxyl groups on the BOPET surface (third step), after which the condensation reaction takes place between the silanol functions of neighbouring molecules. Self-assembly is driven by lipophilic interactions between the linear alkane moieties. During the initial period, only a few molecules will adsorb (by steps 1–3) onto the surface and the monolayer will definitely be in a disordered state. However, at longer times, the surface coverage eventually reaches the point where a well-ordered and compact (or crystalline) layer is obtained (step 4).

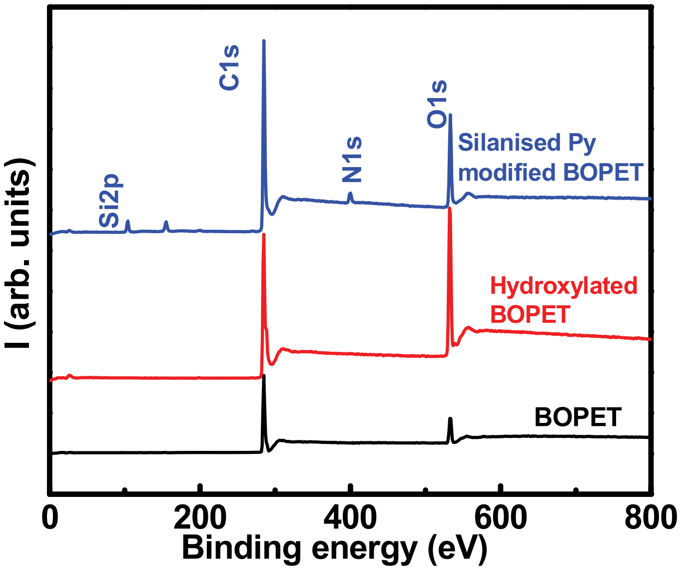

Fig. 4.3: XPS spectrums of the pristine, hydroxylated and silanisedPy modified BOPET substrates.

The pristine and silanised-Py modified BOPET substrates were further characterized by X-ray photoelectron spectroscopy (XPS) and the results are shown in Fig. 4.3. From this figure, it can be seen that the pristine and hydroxylated BOPET substrates show the presence of only C1s and O1s, whereas the survey region of the silanizedPy modified BOPET shows two additional peaks, i.e. N1s peak at 399.6 eV and Si2p peak at 103.6 eV; which confirms the presence of the silanised-Py layer at the surface of BOPET. The contact angle for a drop of pure distilled water on BOPET with a silanised-Py layer grafted at the surface was found to be ~85°, which is in agreement with the reported value [179].

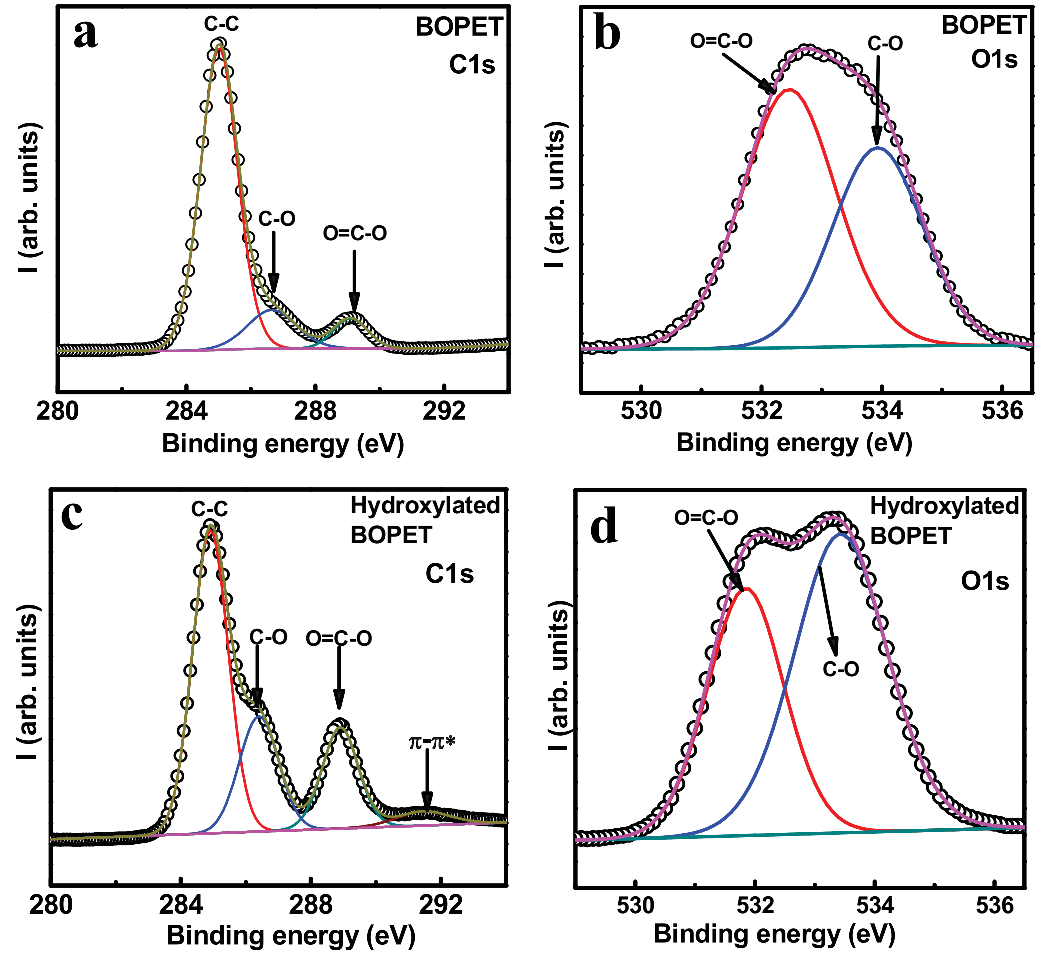

Fig. 4.4: XPS C1s and O1s spectrum for pure BOPET (a and b) and hydroxylated BOPET substrate (c, d).

In order gain further insight into the surface treatment given to the BOPET substrate, the high resolution XPS spectra for pure and hydroxylated BOPET is shown in Fig. 4.4. The C1s spectra for pure BOPET substrate consists of three main peaks at 285, 286.7 and 288.9 eV corresponding to three carbon environments namely C-C or C-H, C-O and O=C-O (ester group), respectively [174-176, 180].Similarly the deconvolution of the O1s spectra of BOPET substrate shows two separated peaks at 531.8 and 533.4 eV corresponding to O=C-O (ester group) and C-O respectively [174-176, 180]. In a similar manner, high resolution C1s and O1s spectrum for the hydroxylated BOPET was analyzed. It is important to note that after hydroxylation process, BOPET surface show the C1s region with a π-π* shake-up satellite, shown in Fig.4.4(c), due to the aromatic rings. The absence of π-π* shake-up satellite and very high C (at%) for the pristine BOPET sheets suggest a superficial protective layer on its surface, which gets cleaved on hydroxylation and then imparts OH groups to the surface. It may be noted that for pristine BOPET the C/O ratio was found to be very high (~6.7), which does not matches with the chemical formula $(C_{10}H_8O_4)_n$ for BOPET. On the hydroxylation of BOPET the C/O ratio was found to be ~2.7, indicating that BOPET surface is regaining its intrinsic composition on hydroxylation.

Table 4.1 shows the chemical composition of the pristine and hydroxylated BOPET surface, as obtained from the analysis of XPS spectra of Fig. 4.4.

Table 4.1: Chemical composition of the pristine and hydroxylated BOPET surface determined from the analysis of the XPS data.

Sample	**C (at%) for C-C or C-H**	**C (at%) for C-O**	**C (at%) for O=C-O**	**O (at%) for C-O**	**O (at%) for O=C-O**
Pristine BOPET	79.5	13.4	7.2	42.1	57.9
Hydroxylated BOPET	54.7	22.8	18.7	59.7	40.3

From Table 4.1 it can be seen that on hydroxylation of pristine BOPET surface the C1s component corresponding to (C-C or C-H) decreased from 79.5% to 54.7%, while the C-O and O=C-O components showed an increase from 13.4 and 7.2 to 22.8 and 18.7 respectively. Similarly on hydroxylation of BOPET; the O1s component corresponding to C-O group shows an increase from 42.1 to 59.7; while corresponding to O=C-O shows a decrease from 57.90 to 40.28. Interestingly on hydroxylation, the full width at half maximum of the O1s component for O=C-O bonds decreases from 1.9 to 1.6 eV, while the FWHM for C-O increases from 1.8 to 1.9. According to Beamson& Briggs C-OH groups (e.g. for poly(hydroxyethyl methacrylate)) yield O1s positions in the 532.7-533.1 eV binding energy (BE) range, lower than the 533.1-533.2 eV and 533.2-533.9 eV ranges reported for C-O-C chemical environments of aromatic polyesters and polymethacrylates, respectively [181].These XPS results also show that in the process of KOH treatment of the BOPET substrate, some of the O=C-O groups (corresponding to the ester group in the BOPET chains) undergoe saponification that leads to fragmentation of the chains and contributes to the formation of–OH species groups. These results also confirm the incorporation of large amounts of oxygen containing polar functional groups in the BOPET films after treatment with KOH [174-176]. These XPS results are in agreement with the enhanced intensity ratio I_{O-H}/I_{C-H} FTIR absorption bands; and low water contact angle on the surface of hydroxylated BOPET.

4.2.3 Formation of polypyrrole-silver composite films

In the present work, PPy-Ag nanocomposite films were prepared on the silanisedPy modified BOPET substrates by the photo-polymerisation approach. Control experiments were also carried out by depositing the PPy-Ag films on pristine (unmodified) BOPET substrates. The photo-polymerization of pyrrole in the presence of $AgNO_3$ photo-initiator has recently been investigated to form core-shell like structures. In this process, at first stage of reaction is the excitation of Ag^+ on UV irradiation, making it an electron acceptor (reduction) to receive electrons from Py monomer [182]. This eventually results in the formation of pyrrole radical and Ag in the metallic state. The pyrrole radicals then undergo the polymerization process such as dimerization and chain growth [27].

In the present study, we have utilized the silanised-Py terminated BOPET surfaces to control the photo-polymerization of pyrrole in the plane of the substrate, as schematically shown in Fig. 4.5. Hereafter, we discuss the experimental results on the morphological evaluation of PPy-Ag composite films as a function of concentration of $AgNO_3$ and UV irradiation time.

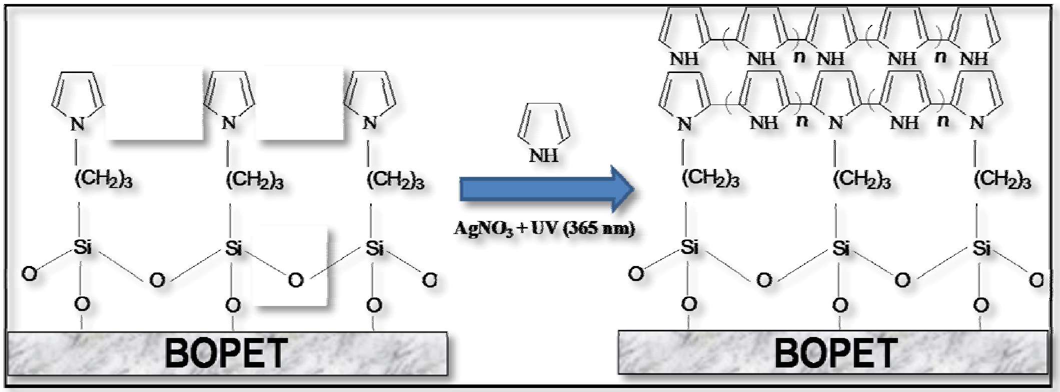

Fig. 4.5: Scheme showing the synthesis of PPy-Ag nanocomposite films on the silanisedPy modified BOPET substrate using photo-polymerisation approach.

4.3 Characterization of composite films

4.3.1 Microstructure evolution

In order to prepare PPy-Ag films on silanisedpyrrole modified BOPET substrate, two different set of experiments were carried out: (i) The ratio of pyrrole/$AgNO_3$ was fixed at 0.5 M/0.5 M and UV exposure time was varied from 15 min to 180 min; and (ii) Pyrrole concentration (0.5 M) / UV exposure time (120 min) were fixed and $AgNO_3$ concentration was varied from 0.05 M to 0.7 M.

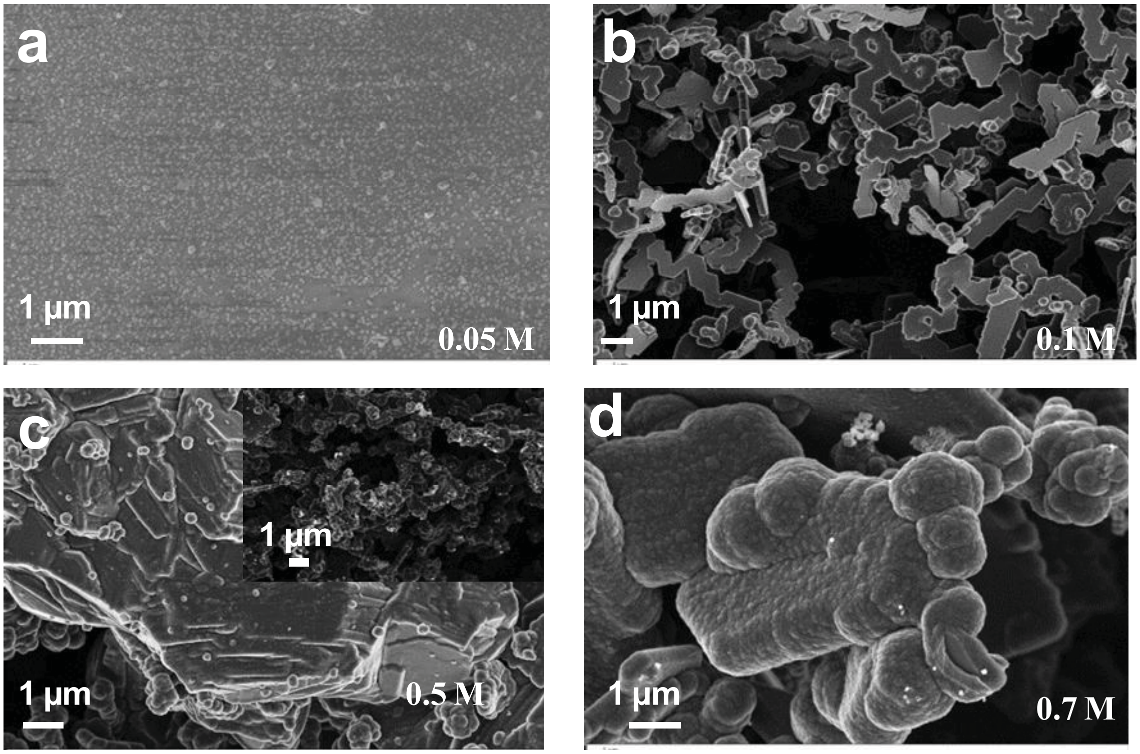

Fig. 4.6: Morphology (SEM images) of PPy-Ag nanocomposite films grown in silanisedPy modified BOPET substrate for (a, b, c, d) different $AgNO_3$ concentration (Py ~ 0.5 M) and for fixed UV exposure of 120 min. Inset of image c, show the PPy-Ag films prepared under identical experimental condition on pristine BOPET substrate.

Fig. 4.6 (a to d) shows the SEM images of PPy-Ag films prepared on surface modified BOPET substrate for different $AgNO_3$ concentration for fixed UV exposure time of 120 min. At very low concentration of $AgNO_3$ (0.05M), the obtained films are very thin and show very small and well separated grains of PPy, shown in Fig.4.6(a). With increase in $AgNO_3$ concentration to 0.1M, the films grow in two dimensional lamellar structures in the substrate plane, shown in Fig. 4.6(b), which are well interconnected. Increasing further the $AgNO_3$ concentrations to 0.5 M, leads to almost full coalescence of the lamellar structures, giving rise to the plate-like PPy crystals in the plane of the BOPET substrates. These results clearly indicate that the silanized Py has directed the growth of polypyrrole in the plane of the substrate. The control experiment, that is, PPy-Ag films under identical conditions (Py/$AgNO_3$ ~ 0.5M/0.5M, UV exposure time ~120 min) on pristine BOPET substrate, exhibit a granular morphology, as shown in the inset of Fig.4.6(c). This result indicates that silanizedPy layer acts like a template for the growth of polypyrrole film. However, for higher concentration of $AgNO_3$ (0.7 M), the morphology turns into the granular one, which grow on top of the plate-like structures. In addition, we also observe bright spots, which are later confirmed as the precipitates of metallic Ag.

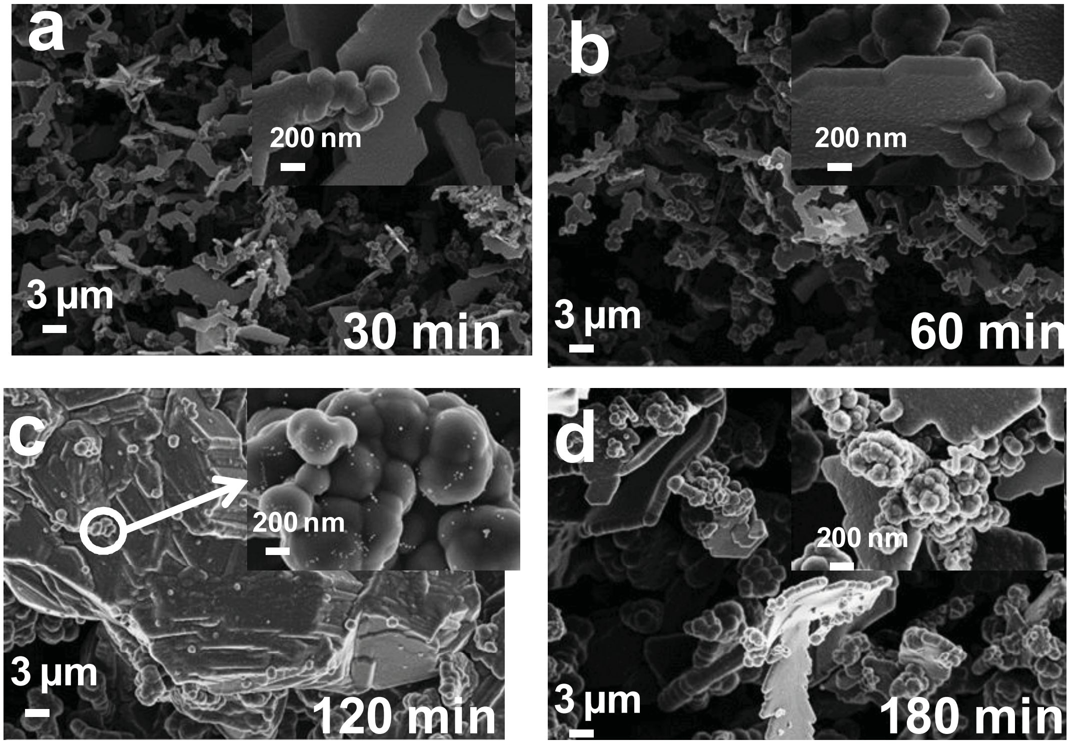

Fig. 4.7: Morphology (SEM images) of PPy-Ag nanocomposite films grown in silanisedpyrrole modified BOPET substrate for (a, b, c, d) different UV exposure time for fixed Py/$AgNO_3$ (0.5M/0.5M) ratio. Inset images are obtained at high magnifications

Fig. 4.7 (a to d) shows the SEM images of PPy-Ag films prepared on surface modified BOPET substrate for different UV exposure time (15 min to 180 min). The films prepared for UV exposure time of 15 min are very thin and inhomogeneous (similar to the films prepared at low $AgNO_3$ concentration ~ 0.05M). As seen from Fig. 4.7 (a) to (c), for UV exposure time of 30 min, PPy-Ag film consists of two dimensional lamellar structures, on these lamellar structure the nucleation of granular structure starts at UV exposure time of

120 min. However with increasing the UV exposure time to 180 min (Figure 7(d)), PPy-Ag film consists of granular morphology.

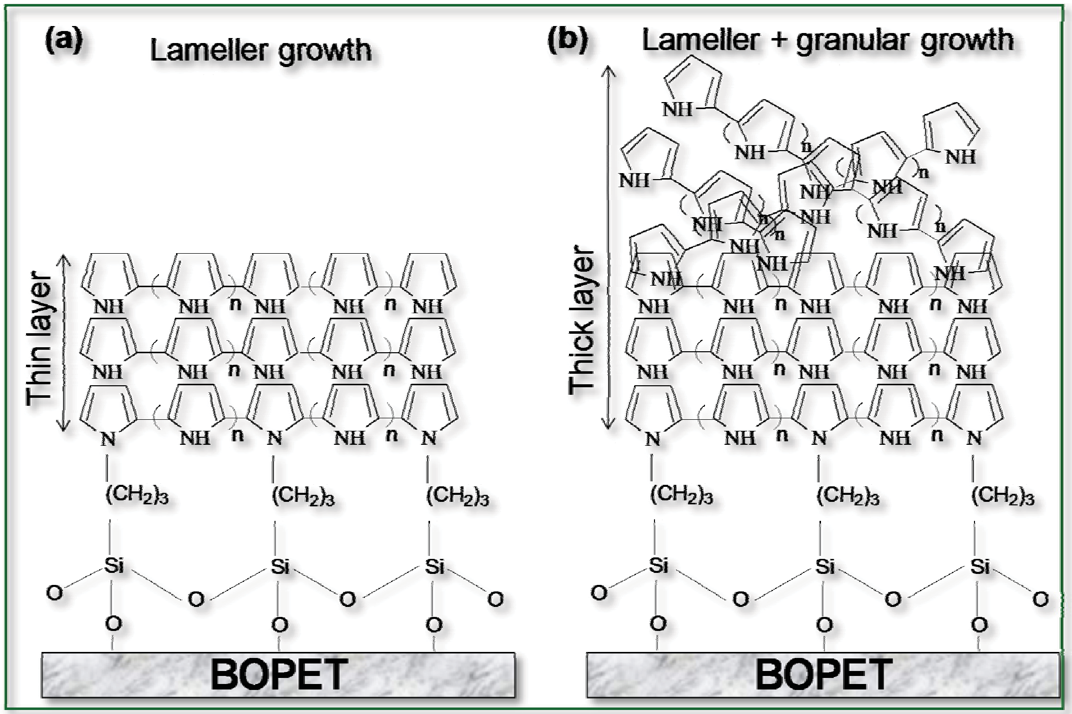

Fig. 4.8: The schematic diagram showing the growth of PPy-Ag nanocomposite films grown on silanisedPy modified BOPET substrate (a) for thinner films i.e. at low concentration of $AgNO_3$ or at low UV exposure time (lamellar growth) (b) for thicker films i.e. at high concentration of $AgNO_3$ or at low UV exposure time (lamellar growth and granular growth).

These UV exposure time or $AgNO_3$ concentration dependent films morphologies i.e. a transition from two dimensional lamellar to the granular morphologies can be explained by variation of films thickness on silanised-Py modified BOPET. For short exposure time (~ 30 min) / or at low $AgNO_3$ concentration the obtained films are very thin (~ 100nm); hence the films tries to grow in the substrate plane (i.e. two dimensional lamellar structure) due to anchoring of PPy-Ag layer on the grafted silanised-Py layer on BOPET surface, as shown schematically in Fig. 4.8 (a). With increasing UV exposure time / or at high $AgNO_3$ concentration; the thickness of grown PPy-Ag film increases. As shown schematically in Fig 4.8 (b), for the thicker films initial few monolayer growth is lamellar due to interaction with the substrate and layer afterwards adopt granular morphology (i.e. inherent to polypyrrole) due to weaker polymer substrate interaction.

In order to determine the role of silanized-Py layer grafted on BOPET in the crystallinity of the photopolymerised PPy-Ag films (concerning only PPy characteristics), the grazing incidence X-ray diffraction data for the films prepared on silanized and pristine BOPET substrate was recorded, and results are shown in Fig. 4.9. The high intensity and sharper peak (located at 26^0) of the PPy-Ag films prepared on silanised-Py modified at BOPET confirms their better structural ordering of PPy chains [183]. The inter-chain separation (*d*) as obtained from the GIXRD data is ~3.4 Å; this *d* spacing matches well with the highly conjugated and ordered PPy films prepared using interfacial chemical polymerization [26].

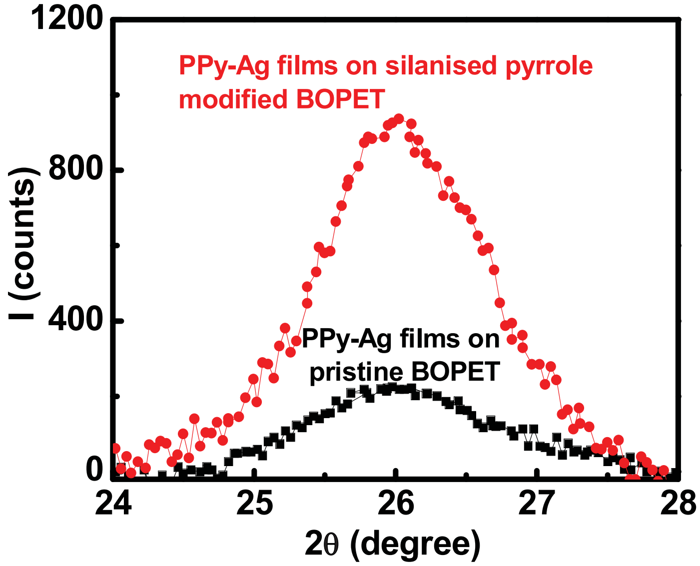

Fig. 4.9: GIXRD spectra of the PPy-Ag films ($AgNO_3$ ~ 0.5 M, 120 min) prepared on the silanisedPy grafted and pristine BOPET substrates

As discussed in earlier, the photopolymerization process leads the precipitation of metallic Ag.In order to see the how metallic Ag is distributed in the PPy films, the X-ray elemental mapping of Ag and C in the were recorded and the results are shown in Fig.

4.10 (a) and (b), respectively for the films prepared at different UV exposure time and for different $AgNO_3$ concentration.

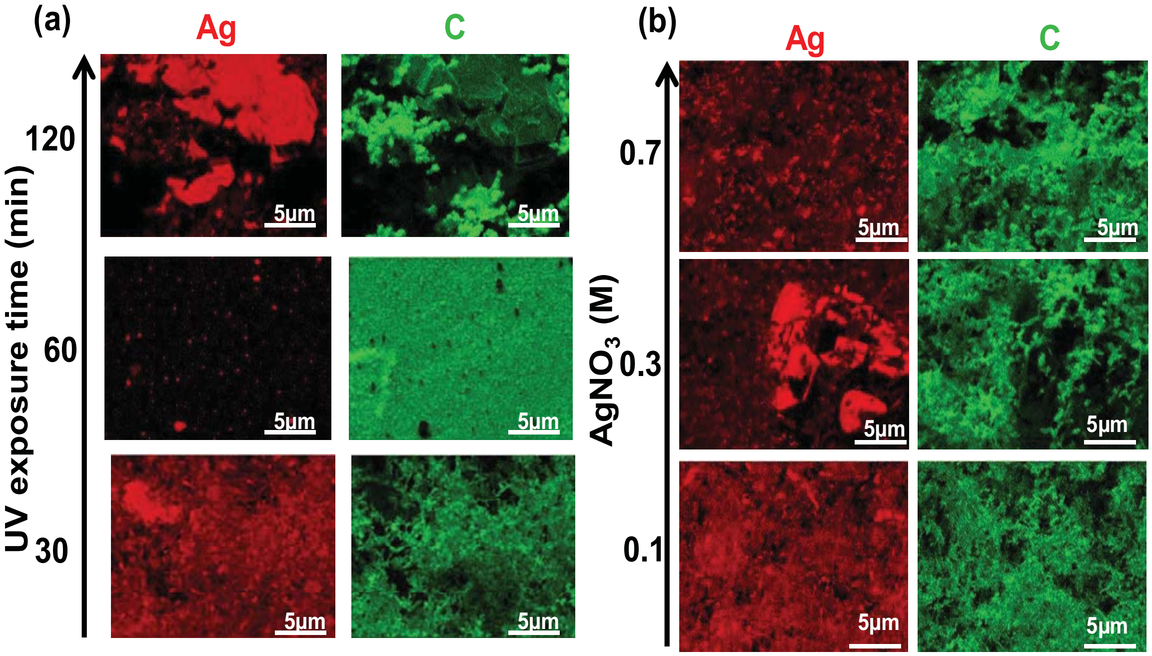

Fig. 4.10: X-ray elemental mapping (Ag shown by red and C shown by green colours) of PPy-Ag nanocomposite films grown on silanisedpyrrole modified BOPET substrate for (a) different UV exposure time for fixed Py/$AgNO_3$ (0.5M/0.5M) ratio (b) for different $AgNO_3$ concentration and for fixed UV exposure of 120 min.

Fig. 4.10(a) reveals that at very low UV exposure time of 30 min; there is a fairly uniform distribution of Ag (red colour) and C (green colour) in the films. From Fig. 4.10 (a) it can also be seen that on increase of UV exposure time to 60 min; in addition to Ag nanoparticles, Ag precipitates of micron size are also formed. Probably at this stage the more uniform coating of PPy on the Ag nanoparticles mask the signal from Ag, hence the contrast between signal from Ag (micron size particles) and C is very high in this case. At the highest UV exposure time ~ 120 min, the big precipitates (few μm in size) are observed. From Fig. 4.10 (b) it can be seen that with increasing $AgNO_3$ concentration, Ag also precipitates out of the PPy matrix; however at very high concentration of 0.7 M, Ag again distributes more evenly in the films. This result suggests that at high concentration of $AgNO_3$, due to a larger number of Ag nucleation centers, many Ag particulates of smaller size are formed. These results also show immiscibility of Ag in the PPy matrix. At low concentration of Ag, it might occupy the inter-chain space and hence facilitates the easy transfer of charge between the polymer chains, however at higher concentration of Ag, Ag precipitates out of the PPy matrix and form big particulates. Such a precipitation of Ag in the PPy matrix also inhibits the grain growth of PPy, as a result the grown PPy-Ag films are more granular in nature, particularly at high $AgNO_3$ concentration or higher UV exposure times.

Fig. 4.11 (a-c) shows the work function mapping (image size 2 mm×2mm) of PPy-Ag films prepared on silanised-Py modified BOPET substrate for different $AgNO_3$ concentration of 0.1, 0.3 and 0.7M. These images reveal the variation of work function from 4.7 eV (i.e. for silver) to 5.1 eV (i.e. for polypyrrole) [184, 185]. At low concentration of $AgNO_3$ ~0.1 M, one can notice (Fig. 4.11(a)) more of polypyrrole feature (i.e. Green-yellow mixed region) and at $AgNO_3$ concentration of 0.3 M, spatial extent of Ag (i.e. blue region) becomes more. Further increase of $AgNO_3$ concentration to 0.7 M, the features from PPy dominates the image. These results are in agreement with the X-ray elemental mapping of PPy-Ag films shown in Fig. 4.10 (b).

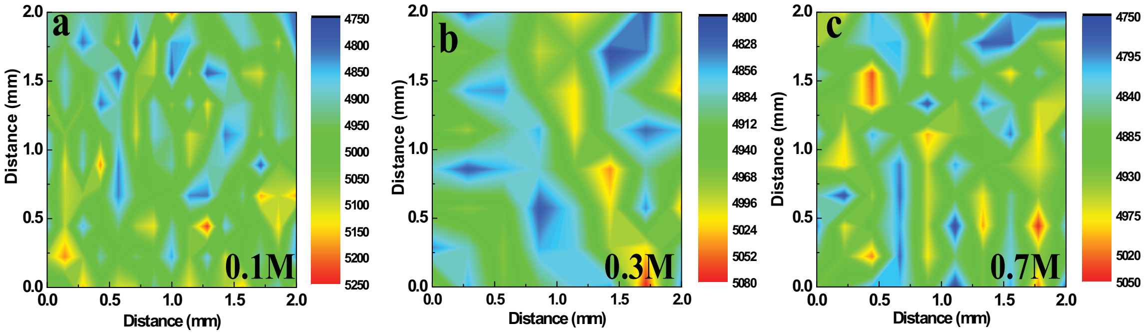

Fig. 4.11: Work function images (obtained from Kelvin probe) of PPy-Ag nanocomposite films grown on silanised BOPET substrate for different $AgNO_3$ concentration of 0.1M (a), 0.3M (b), 0.7M (c) for fixed UV exposure of 120 min. The right hand side colour bar of each image shows the work function value in meV.

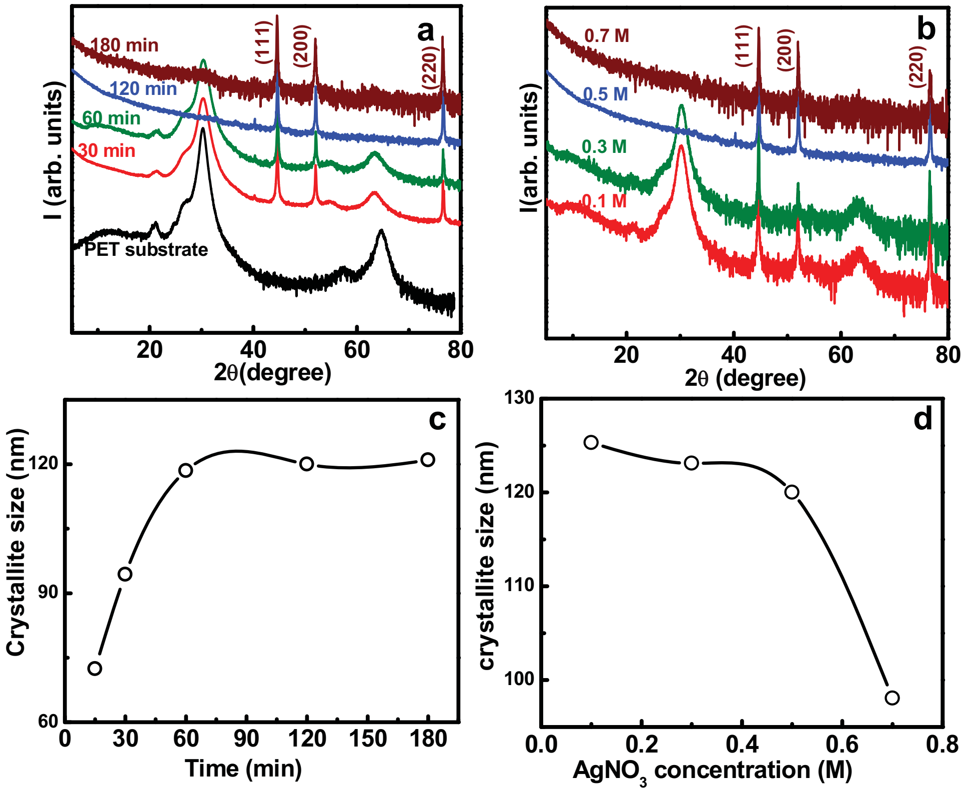

Fig. 4.12: XRD for of PPy-Ag films grown on silanisedpyrrole modified BOPET substrate for (a) different UV exposure time for fixed Py/AgNO$_3$ (0.5M/0.5M) ratio and (b) different AgNO$_3$ concentration and for fixed UV exposure of 120 min. Ag crystallite size as obtained from width of (111) diffraction peak and using Scherrer formula for different UV exposure time (c) and different AgNO$_3$ concentration (d).

4.3.2 Structural characterization

(a) X-ray diffraction

Fig. 4.12 shows the XRD pattern of the PPy-Ag films for different UV exposure time and for different AgNO$_3$ concentration. The XRD pattern of the pristine BOPET substrate, shown in Figure 4.12(a) indicates the presence of broad diffraction peak at 30 and 65 degrees, which confirms the semi-crystalline nature of the substrate. In general the polyethylene terephthalate (PET) substrate are amorphous in nature and the manufacturing process of BOPET involves formation of a sheet from molten PET, which is then biaxially oriented by drawing and, subsequently followed by "heat set" under tension at temperatures >200°C [186]. The heat setting step prevents the sheet from shrinking back to its original un-stretched shape and locks-in the molecular orientation in the sheet plane. The molecular orientation also induces the formation of many crystal nuclei and from the XRD data we have estimated the crystallite size of ~ 6.35 nm for BOPET. It may be noted that PPy-Ag films prepared for short UV exposure time of 30 - 60 min or at lower $AgNO_3$ concentration (< 0.5M) shows the presence of substrate peak due to the low thickness of the films.

Concerning crystallinity of the silver present in the film, three peaks centered at 44.3, 51.7, and 76.8 were observed in the XRD spectrum, and are assigned to (111), (200), and (220) diffraction planes respectively. These patterns are in agreement with JCPDS files No 00-001-1164; and confirms metallic nature of silver particles produced by UV-induced reaction of Py and $AgNO_3$ [187, 188]. From the full width half maximum (FWHM) of the highest intensity (*111*) peak of Ag, the size of the crystallites (D_p) was estimated by Scherrer formula as [189]:

$$D_p = (0.94\lambda)/(\beta_{1/2}\cos\theta) \qquad 4.1$$

Whereλ is radiation wavelength of cobalt X-rays, $\beta_{1/2}$ the full width at half maximum (FWHM) of diffraction peak and θ is the peak position. It is to noted that applicability of the equation (3) is only for crystallites having size in the range ~ 130 nm. The analysis of the XRD peak boarding for all samples, gives the sizes of the Ag crystallite in range of 70 to 120 nm. It is important to mention that although the X-ray elemental mapping of the PPy-Ag films prepared for long UV exposure time / for high $AgNO_3$ concentration shows the presence of few micron size Ag crystallites, but there is also nano-size Ag crystallite distributed in the PPy matrix, which contributes to the XRD peak broadening. As seen from Fig. 4.12(c), the size of Ag crystallites initially increases with UV exposure time and after 120 min the crystallite size become constant at ~ 120 nm. This result is expected as for fixed $AgNO_3$ concentration, with increase of UV exposure time initially more and more silver be available hence the size of Ag nanoparticle will grow, after some time entire $AgNO_3$ in the solution will get consumed and there will be no further growth of the Ag crystallites. Figure 4.12(d) reveals the variation of Ag crystallite size as a function of $AgNO_3$ concentration for fixed UV exposure time of 120 min. It can be seen that for $AgNO_3$ concentration of 0.1 to 0.5M the crystallite size is nearly constant ~ 120 nm. However for higher concentration of $AgNO_3$, the crystallite size reduces to 90 nm due to more numbers of nucleation centers of Ag, this result is also supported by the X-ray elemental mapping and work function mapping data's as discussed earlier.

(b) X-ray photoelectron spectroscopy

Fig.4.13 (a) and (b) respectively shows the XPS survey spectra and N1s high resolution for PPy-Ag-1, PPy-Ag-2 and PPy-Ag-3 films, which shows the four prominent peaks: C1s (~285eV), Ag 3d doublet centered at 368.3-374.4eV, N1s (399.5eV) and O1s (~533eV) [173, 180]. It is very interesting to note that the Ag $3d_{5/2}$ peak is centered at 368.2 eV, which suggest the metallic nature of Ag. The relative intensity of the Ag3d doublet (e.g. to N1s) intimately depends on both polymerization time and initial concentration of silver nitrate. The analysis of high resolution XPS spectra of C1s, Ag3d doublet, N1s and O1s elements gives the surface chemical composition as shown in Table 4.3. Particularly, the peak-fitted N1s regions permitted to determine the N^+/N atomic ratios as reported in Table 4.3.

Table-4.3: Surface chemical composition (in at. %) as determined by XPS

Sample	**C/N**	**Ag/N**	**N^+/N**	**NO_3/N**
PPy-Ag-1	5.89	0.123	0.17	0.21
PPy-Ag-2	5.36	0.053	0.17	0.17
PPy-Ag-3	5.68	0.024	0.14	0.11

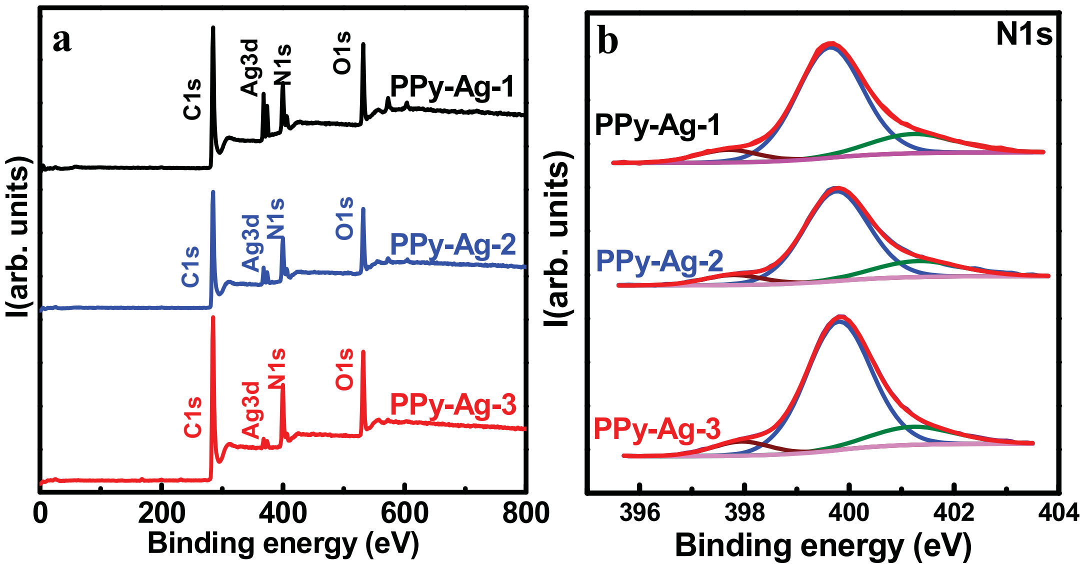

Fig. 4.13: (a) XPS survey scan for sample PPy-Ag-1 ($AgNO_3$~0.5M, 120 min), PPy-Ag-2 ($AgNO_3$~0.5M, 30 min), PPy-Ag-3 ($AgNO_3$~0.1M, 120 min) (b) N1s high resolution XPS spectrum for PPy-1, PPy-2 and PPy-3 films.

From Table- 4.3 it can be seen that ratio (in %) of N^+ (oxidized pyrrole i.e. at 401.2 eV)/N (neutral pyrrole i.e. at 399.8 eV), as determined from N1s peak fitting (shown in Figure 17(b)), is close to 0.17, indicating that these films have lower doping level than standard doped PPy films. It may be noted that, for highly conducting pyrrole the typical value of N^+/N~0.36 [87, 137, 173]. The ratio of C/N for all sample is close to 5, indicates the contribution for C and N comes from pyrrole only. It can also be seen that for same concentration of $AgNO_3$ (~ 0.5 M), the amount of Ag incorporated in the films (PPy-Ag-1, and PPy-Ag-2) is less for small UV exposure time.

(c) Fourier transform infrared spectroscopy

In order to further probe the insight of PPy-Ag nanocomposite films; the FTIR spectrum of all prepared samples was recorded. Fig.4.14 (a) and 4.14(c) respectively shows the FTIR spectra of the PPy-Ag nanocomposite films synthesized for different UV exposure time and different $AgNO_3$ concentration. These FTIR spectra exhibit all characteristic peaks of polypyrrole as reported in the literature i.e. anti-symmetric (1567 cm^{-1}) and symmetric (1483 cm^{-1}) ring stretching modes, C–N (1313 cm^{-1}), C–C (1408 cm^{-1}), C–H in-plane bending (1196 cm^{-1}), polypyrrole main chain (1040 cm^{-1}) and ring bending vibrations (778 cm^{-1} and 924 cm^{-1}) [134-136]. It has been shown that the intensity ratio (I_{1567}/I_{1483}) is inversely proportional to the conjugation length [26, 135]. The data presented in the inset of Fig. 4.14(a) and 4.14(c), the linear relationship of electrical conductivity with I_{1567}/I_{1483} for different UV exposure time (shown in Fig.4.14(b)) and for different $AgNO_3$ concentration (shown in Fig. 4.14(d)), therefore, clearly show an enhanced conjugation with increasing UV exposure time and with increasing concentration of $AgNO_3$.

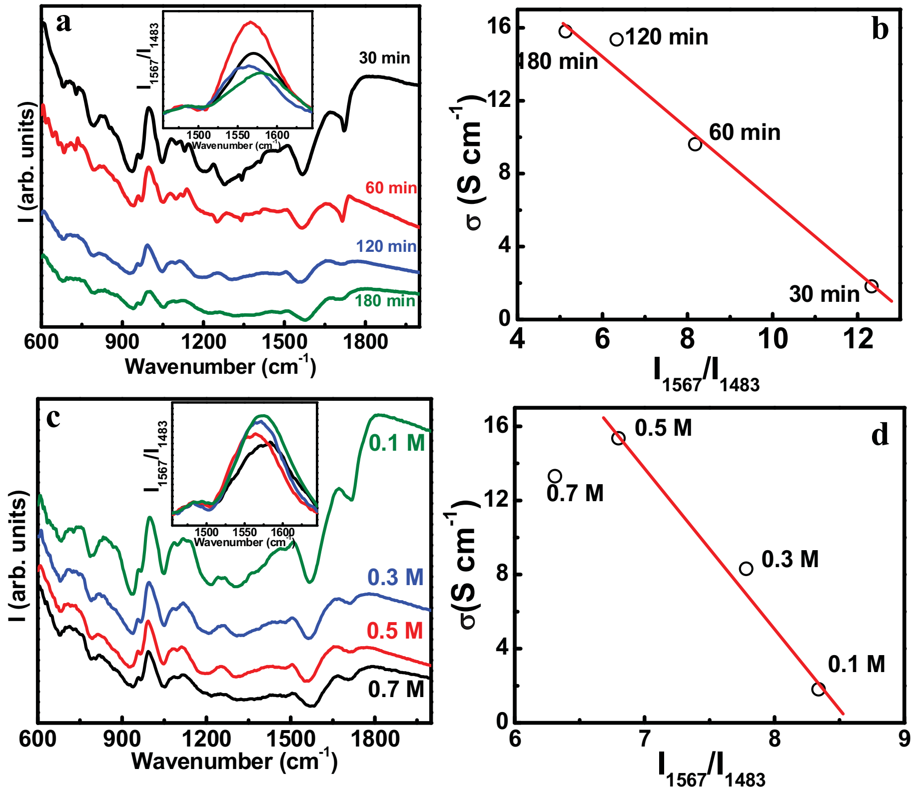

Fig. 4.14: (a) and (c) shows the typical FTIR spectra of the PPy-Ag nanocomposite films synthesized for different UV exposure time and different $AgNO_3$ concentration. Inset shows the FTIR spectra in the region 1450-1650 cm^{-1} with intensity normalized to the 1483cm^{-1}peak.(b) and (d) shows the plot of σ versus I_{1567}/I_{1483} for different UV exposure time and different $AgNO_3$ concentration.

(d) Raman spectroscopy

The Raman spectrum of the PPy-Ag nanocomposites samples was recorded and the results are shown in Fig. 4.15(a) and Fig. 4.15(b) respectively for different UV exposure time and different $AgNO_3$ concentrations. The Raman spectra of all the samples exhibited broad peaks at 1332 (correspond to ring stretching mode) and 1576 cm^{-1} (symmetric C=C stretching, this band is very sensitive to the oxidation) [190]. It is important to note that the most commonly reported Raman peak at 928 cm^{-1} i.e. associated with the bipolaron, and 1045 cm^{-1} i.e. assigned to the C-H in plane deformation are absent in all the sample except for $AgNO_3$ concentration of 0.7M. The absence of bipolaron peak in the Raman spectrum confirms the PPy-Ag nanocomposite films are undoped, which is in agreement with the XPS result [190].

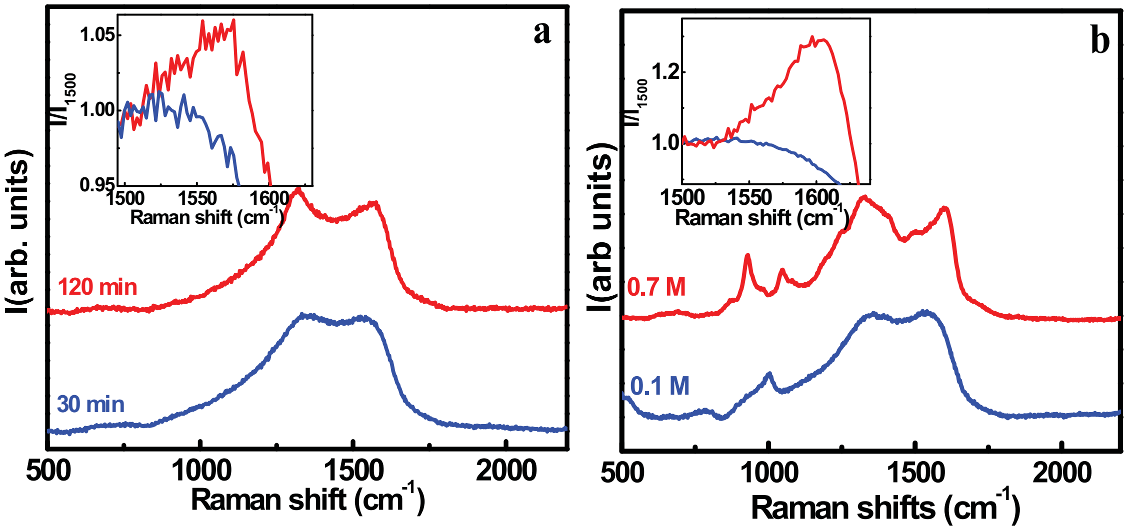

Fig. 4.15: (a) and (b) shows the typical Raman spectra of the PPy-Ag nanocomposite films synthesized for different UV exposure time and different $AgNO_3$ concentration. Inset shows the Raman spectra in the region 1500-1620 cm^{-1} with intensity normalized to the 1500 cm^{-1}peak (skeletal band of PPy).

The intensity ratio of Raman band of the symmetric C=C stretching mode at 1576 cm^{-1} to the skeletal band at 1500 cm^{-1} can also reflect the relative conjugation length [26, 190]. In the inset of Fig. 4.15(a) and Fig.4.15(b) it can be seen that the intensity ratio (I_{1576}/I_{1500}) with increasing UV exposure time and with increasing concentration of $AgNO_3$; confirming the enhanced conjugation with increasing UV exposure time and with increasing concentration of $AgNO_3$ as also supported by FTIR data.

4.4 Electrical conductivity and electron transport mechanism

The effect of different UV exposure time on electrical conductivity of the resulting PPy-Ag films is shown in Fig. 4.16 (a). For increasing UV exposure time (30 min to 180 min) and for a fixed Py/$AgNO_3$ (0.5M/0.5M), thickness of synthesized films increases from 100 nm to 10 µm. It can be seen that after UV exposure of 120 min, the conductivity of films saturates at ~ 15 Scm^{-1}. This result is also supported by the fact that films thickness (~ 10 µm) as well as Ag crystallite size (~120 nm) effectively saturates after 120 min of UV exposure. It is also important to mention that PPy-Ag films prepared on pristine BOPET substrate for a fixed Py/$AgNO_3$ (0.5M/0.5M) and UV exposure time 120 min shows the electrical conductivity of 0.5 Scm^{-1} i.e. 30 times smaller than the films prepared under identical experimental condition on silanised BOPET substrate. This result is suggest that silanisedPy layer grafted on BOPET provides better polymer chain ordering, and hence improves the conductivity of PPy-Ag films.

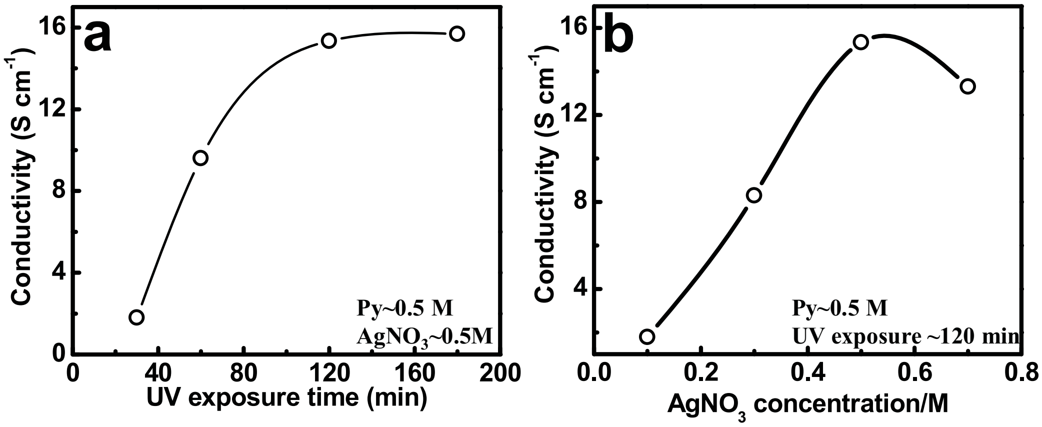

Fig. 4.16: Effect of UV exposure time (a) and $AgNO_3$ concentration (b) on the electrical conductivity of PPy-Ag nanocomposite films

The variation of conductivity for a fixed UV exposure time of 120 min and different $AgNO_3$ concentration (0.1M to 0.7M) is shown in Fig. 4.16 (b). It is important to note that conductivity increases with increasing $AgNO_3$ concentration from 0.1M to 0.5M. At very high concentration of $AgNO_3$~0.7 the conductivity of the films drops down, which may be attributed to the fast and random photopolymerisation process (also supported by the random granular morphology of films).

The variation of conductivity with UV exposure time and with $AgNO_3$ concentration can be explained by reviewing the SEM and X-ray elemental results discussed earlier. The morphology of the PPy-Ag films (as shown in Fig .4.6 and 4.7) indicate that the conductivity (σ) of these films can be expressed as $\sigma = \sigma_{\text{Intra}}+\sigma_{\text{Inter}}+\sigma_{\text{Ionic}}$ [87], where σ_{Intra} is the contribution from the intragrain region and depends on the conjugation lengths (l) over which charge carriers are localized. In the case of unoriented polymer, the σ_{Intra} varies as $1/ln$ (n = 3.2–3.5), indicating that shorter is the conjugation length lower is the conductivity. If l is too short, then the charge transport is limited by interchain hopping. In fact, l can be altered by improving crystallinity and changing doping levels of conducting polymer. σ_{Inter} is the inter-grain conductance and depends on the height of the potential barrier formed at the grain boundaries. In general, smaller is the grain size; lower is the value of σ_{Inter}. σ_{Ionic} is controlled by mobility of the counter ions. The variation of electrical conductivity for PPy-Ag nanocomposite films with increasing UV exposure time/ increasing $AgNO_3$ concentration (till 0.5M) is attributed to the ordered PPy chain in the lamellar structure as well as incorporation of Ag nanoparticles (which are immobilized between the PPy chains) which helps in the inter-chain hopping of charge carriers.

Since the electrical properties of the PPy-Ag nanocomposites films are very much dependent on the structural aspects like the orientation, conformation, conjugation length and interchain connectivity; therefore we studied the low temperature charge transport properties of PPy-Ag nanocomposite films in the details. For this study the three samples were chosen; which are designated as PPy-Ag-1 (sample with highest conductivity ~ 15 S cm^{-1}, Py/$AgNO_3$ ~ 0.5M/0.5M, UV exposure time ~120 min), PPy-Ag-2 (sample with least polymerization time of 30 min, low conductivity~1.8 S cm^{-1}), PPy-Ag-3 (sample with least $AgNO_3$ concentration ~ 0.1M, low conductivity ~ 1.7 S cm^{-1}). The temperature dependence of d. c. electrical conductivity $\sigma(T)$ of the PPy-Ag nanocomposite films as shown in Fig. 4.17 (a), revealed that the conductivity decreases with temperature exhibiting a semiconducting behaviour in the whole range of investigation. It is also important to note that for sample PPy-Ag-2 and PPy-Ag-3 conductivity drops faster with lowering of temperature as compared to the PPy-Ag-1; which suggest that sample PPy-1 is more structurally ordered. A decrease in σ with lowering temperature indicates critical or insulating behaviour of the films.

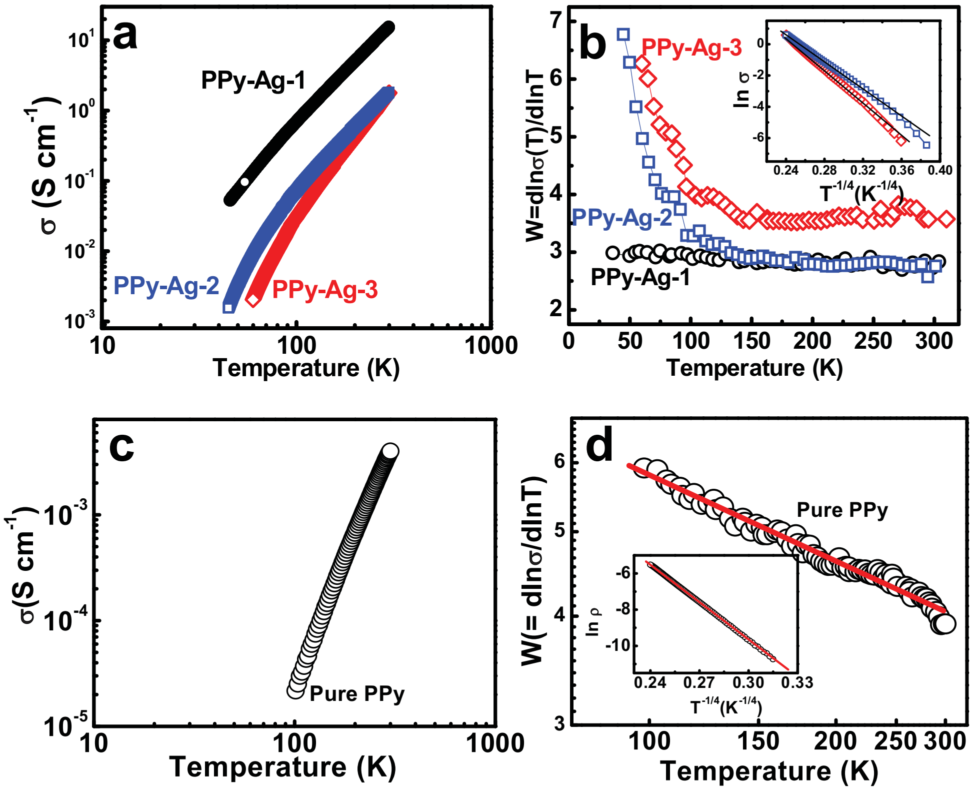

Fig. 4.17: (a) Temperature dependence of the electrical conductivity (σ) for sample PPy-Ag-1 ($AgNO_3$~0.5M, 120 min), PPy-Ag-2 ($AgNO_3$~0.5M, 30 min), PPy-Ag-3($AgNO_3$~0.1M, 120 min) (b)Temperature dependence of reduced activation energy ($W =$ dln[$\sigma(T)$]/dln$T$) for sample PPy-1, PPy-2 and PPy-3.Inset shows the linear fit of lnσversus $T^{-1/4}$ for sample PPy-Ag-2 and PPy-Ag-3, confirming the 3-D VRH conduction. (c) Temperature dependence of the electrical conductivity (σ) for pure PPy films prepared by chemical polymerization (d) Temperature dependence of reduced activation energy (W) for pure PPy films. Inset shows the linear fit of lnρversus $T^{-1/4}$ for PPy films.

The temperature dependence of the reduced activation energy, described as: W= dln[σ(T)]/dlnT, is plotted in Fig. 4.17(b). Positive, zero and negative slopes of W vs T corresponds to the metallic, critical and insulating regimes, respectively [87, 139]. A zero slope for PPy-1 sample shows that it is in the critical regime, while the negative slope for PPy-2 and PPy-3 suggest they are in the insulating regime of metal-insulator (M-I) transition. As seen from inset of Figure 14(b), for PPy-Ag-2 and PPy-Ag-3 samples the temperature dependence of resistivity is best described by Motts 3 dimensional-VRH. Using equations 3.4 to 3.6 and considering the typical value of N (E_F) for moderately doped PPy is 2 x 10^{18} $eV^{-1}cm^{-3}$, the average hopping distance R_{hop}, and R_{hop}/L_c are calculated as shown in Table 4.3. The ratio R_{hop} / Lc >>1 indicates that in these films charge carriers are strongly localized, making it close to the insulating behavior of M-I transition.

For comparison purpose pure PPy samples were prepared on silanised-Py modified BOPET substrate using chemical oxidative polymerization (Py/$FeCl_3$~ 0.5 M/0.5 M Py, polymerization time ~ 120 min). It is to be noted that pure PPy samples cannot be synthesized using the photopolymerisation approach due to the need of $AgNO_3$ as photo-initiators and this process unintentionally incorporates Ag particles in the PPy matrix. The temperature dependence of electrical conductivity for pure PPy films is shown in Fig. 4.17(c). Due to very low conductivity of PPy films at low temperature, conductivity data were taken up to 100 K only. The room temperature conductivity of pure PPy films was found to be 3.4x10^{-3} S cm^{-1} i.e. nearly three order of magnitude lower than the PPy-Ag films. The low conductivity of the pure PPy films is attributed to (i) more disordered nature due to fast chemical polymerization process and (ii) absence of Ag particles in PPy matrix. Negative slope of the reduced activation energy for pure PPy films (shown in Fig. 4.17 (d)) indicates that these films are in the insulating regime of metal-insulator (M-I) transition. The summary of various derived parameters for PPy-Ag and pure PPy films is given in Table 4.3.

Table 4.3: Summary of the various parameters obtained from the 3D- VRH conduction fit of the conductivity versus temperature data

Sample name	**Mott characteristics temperature (T_0) in K**	**Localization length (L_c) in Å**	**Hopping distance (R_{hop}) in Å**	**R_{hop}/L_c**
PPy-Ag-2	*$3.3 x10^6$*	*31.6*	*109.4*	*3.5*
PPy-Ag-3	*$8.1 x10^6$*	*23.4*	*112.4*	*4.8*
Pure PPy	*$2.4 x10^7$*	*16.5*	*103.4*	*6.2*

4.5 Flexibility and adhesion

In order to demonstrate the mechanical flexibility of the PPy-Ag nanocomposites films synthesized on silanised Py modified BOPET sheet, they were bent to various radius of curvatures (*r*) at room temperature. A photograph showing the flexible nature of PPy-Ag nanocomposite films (Py/$AgNO_3$ ~ 0.5 M/0.5 M, 120 min) is shown in Fig. 4.18 (a). In order to measure the electrical resistance (*R*) of the samples, few pairs of gold electrodes were deposited on the PPy-Ag films (photograph shown in right side of Fig. 4.18 (b)). Left side of Fig. 4.18(b) shows the schematic of our bending set up along with resistance measurement circuit. The variation of room temperature resistance of the flexible PPy-Ag films as a function of *r* is plotted in Fig.4.18(c). It is seen that under flat condition (without bending i.e. $r \rightarrow \propto$) the films exhibit a resistance of 0.1 MΩ. On increasing the film bending, i.e. a decrease in *r*, results in a monotonous increase in the resistance. Increase in resistance under bent conditions is not surprising as the strain in the film causes an increase in separation between PPy chains, which in turn reduces the π-π interaction responsible for the charge transport. It is important to note that this strain induced increase in resistance reverts back when the film is brought to flat condition, which is independent of both are i.e. bending at different *r* and the number of bending times. The reversible change of resistance on bending is only possible if the films are adherent to the substrate and does not create any defect state or cracks on bending. Thus, a highly reversible resistance change with bending implies that these PPy-Ag films are suitable for the flexible organic devices.

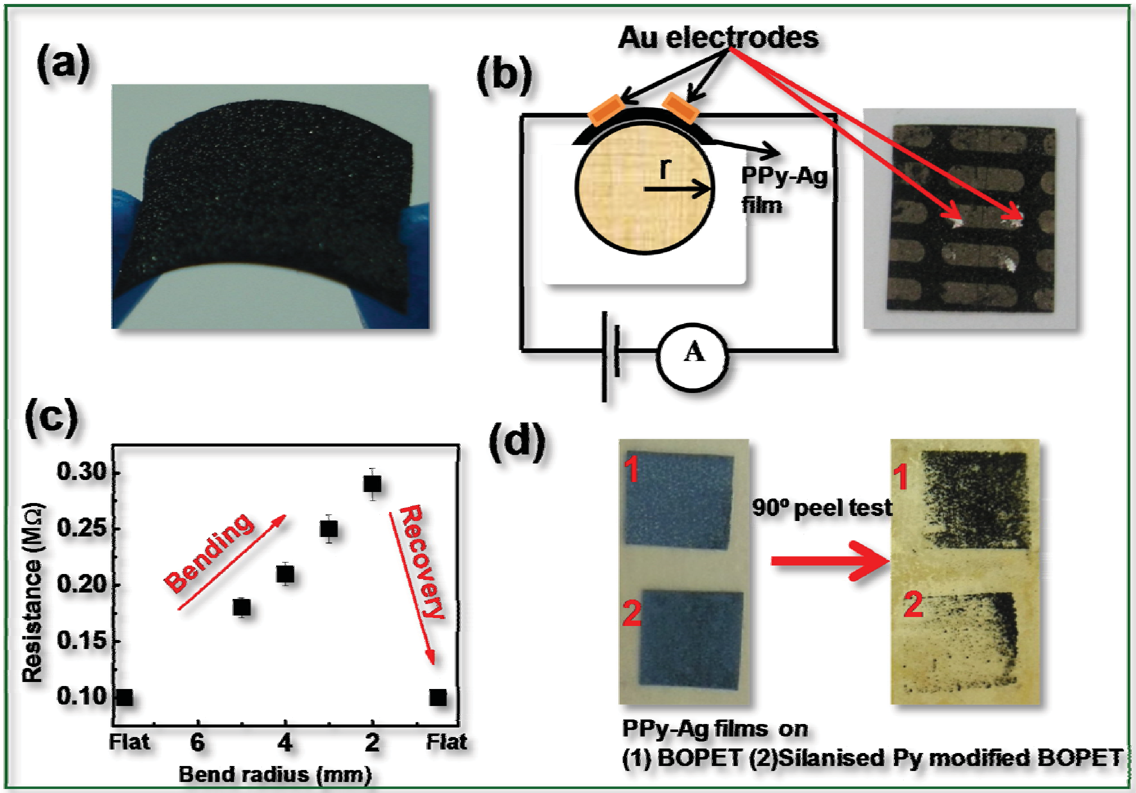

Fig. 4.18: (a) Digital photograph of PPy-Ag films (Py/$AgNO_3$ ~ 0.5 M/0.5M, 120 min) deposited on silanisedPy modified BOPET substrate. (b) Left side shows the schematic of the bending arrangement along with resistance measurement circuit. Right side shows the photograph of few pairs of gold electrodes (gap ~ 12 µm) deposited on the PPy-Ag films (c) Variation in resistance of PPy-Ag films for different bend radius (d) Left side photograph showing PPy-Ag film prepared on pristine BOPET (1) silanisedPy modified BOPET substrate (2). The films are glued on adhesive tape under similar load. Right side photograph shows the material detached from the films by the adhesive tape after 90º peel test.

Qualitative adhesion test (90° peel test) were carried out on PPy-Ag films prepared under identical experimental condition on pristine and silanised Py layer modified BOPET. The results of adhesion test are shown in Fig. 4.18(d). The left side of Fig. 4.18(d) shows the photograph of the PPy-Ag films (1 correspond to films on pristine BOPET and 2 correspond to films on silanised Py modified BOPET) glued with adhesive tap after application of uniform weight (~ 3 Kg) for 10 minutes. Right side photograph of Fig. 4.18 (d) shows the material detached from the films by the adhesive tape after 90º peel test. It can be seen that adhesive tape removes most of PPy-Ag layer from the pristine BOPET surface, while for the films prepared on silanised Py modified BOPET, negligible material gets detached from the surface. These results qualitatively suggest that stronger adhesion of PPy-Ag film on silanised Py modified BOPET substrates.

4.6 Chemiresistive gas sensing characteristics

All the prepared samples (for different $AgNO_3$ concentration and for different UV exposure time) were investigated for their chemiresistive gas sensing properties for the exposure of 20 ppm of each test gas such as NH_3, H_2S, Cl_2, NO, NO_2, CO, CH_4, and C_2H_5OH. Out of all samples only PPy-Ag-3 (i.e. with least amount of Ag ~ .0.1 M) films showed the chemiresistive response for NH_3 and H_2S. The typical response curves recorded of PPy-Ag-3 films for NH_3 and H_2S (for exposure of 30 ppm) are shown in Fig. 4.19(a) and Fig. 4.19(b) respectively. Fig. 4.19(a) reveals that there is a decrease in conductance on exposure to NH_3. A typical response and recovery times towards 30 ppm of NH_3 exposure are 8 sec and 130 min, respectively. However the response of PPy-Ag-3 films for H_2S gas is quite surprising, it shows increase of conductance instead of expected decrease. This contrast response for NH_3 and H_2S is quite consistent, as seen from Fig. 4.19(c), where the films first exposed to 5ppm of H_2S and after recovery it is again exposed to 5 ppm of NH_3. Fig. 4.19(d) shows the plot of sensitivity as a function of NH_3 and H_2S concentration for PPy-3 films, which shows the linear dependence of *S* on the gas concentrations.

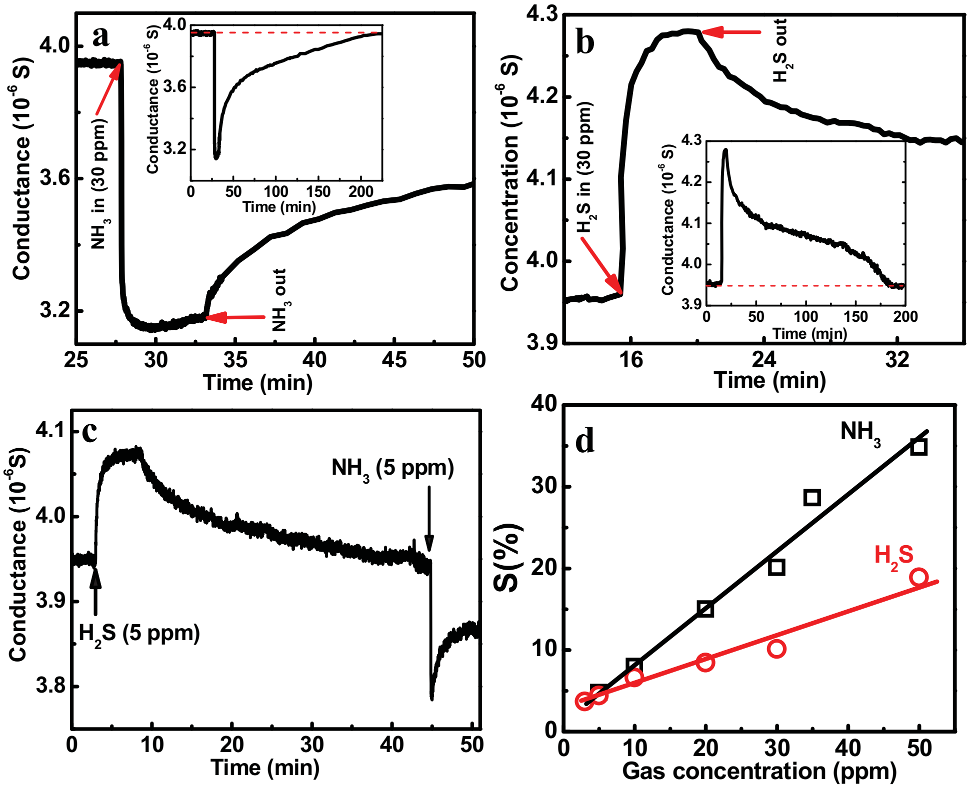

Fig. 4.19: Response curve for PPy-Ag-3 films (synthesis conditions: Py/$AgNO_3$~ 0.5M/ 0.1 M, UV exposure time ~120 min) for NH_3 (exposure of 30 ppm) (a) and H_2S gas (exposure of 30 ppm) (b) exposure at room temperature. Insets shows the full recovery of the sample and dotted red line is base conductance (C_a) of the samples (c) Response curve for PPy-Ag films for successive 5 ppm of H_2S and NH_3 gas at room temperature (d) Sensitivity (S) as a function of H_2S and NH_3 concentration

Now we discuss the mechanism of NH_3 and H_2S sensing and their antagonistic response behavior for PPy-Ag-3 films. Since NH_3 can donate electron to the initially oxidized PPy-Ag-3 film, it results in the decrease in the conductance of films due to partial compensation of the + ve charge of oxidized polypyrrole [144, 191]. As is evident from the response curves in the present case (Fig. 4.19 (a)) the interaction of NH_3 with the films takes place reversibly. The reversible changes have been assigned to compensation effects involving electron or proton transfer, as discussed in Chapter 3 (equations 3.7 and 3.8).

Similarly for the interaction of H_2S with the PPy films, conductance should decrease by considering the electron donating nature of H_2S, but it is not observed is the response data [192]. To explain the conductance rise on H_2S exposure, it is proposed that there is partial dissociation of H_2S on the PPy surface as:

$$H_2S \leftrightarrow H^+ + HS^- \qquad 4.2$$

After the process of dissociation, the HS^- anion compensates for the positive charges in the PPy chains but there is also proton liberation in the films. Since the mobility of cation (H^+) is much larger than the anion (HS^-), therefore the overall effect is conductance rise (expected to be smaller than NH_3) on exposure to H_2S.

In order to rule out the possibility that response to the test gases are from Au or BOPET, the electrodes were prepared on Au coated BOPET and pristine BOPET surface. For Au coated BOPET, The conductivity was found to be very high due to metallic layer of Au, while for pristine BOPET the high resistivity is observed due to the insulating nature of PET chains. These samples did not respond to any of the test gases, confirming the fact that interaction of the test gases with PPy-Ag nanocomposites is responsible for the response.

Now we discuss why only PPy-Ag-3 films i.e. with least $AgNO_3$ concentration (~0.1 M) exhibits the response for reducing gases only. From gas sensing application point of view pure PPy films were widely investigated by different groups. One of the main problem with pure PPy films with moderate electrical conductivity (10^{-2} Scm^{-1}) is the absence of selectivity for oxidizing or reducing gases, this is due to the fact that their conductivity can be either lowered (toward the insulator side) by interaction with reducing gases or can be enhanced (towards metallic side) by interaction with oxidizing gases. This fact gives us a clue that PPy films can be made selective to reducing and oxidizing gases by making them either highly oxidized or highly reduced form. Actually, in our earlier work we have demonstrated that by making a highly reduced PPy films (by incorporation of ZnO nanowires), it can be made selective for highly oxidizing gases (such as Cl_2) [87]. In the present work, highly conducting nature of PPy-Ag composite films supports their response to only reducing gases (such as H_2S and NH_3). In the samples with higher concentration of Ag (even though having highest conductivity ~ 15 Scm^{-1}), the absence of any response for reducing gases suggest that in these samples the gas response properties of PPy films are masked by highly conducting Ag particles. In the samples prepared using high concentration of $AgNO_3$ the major contribution to the electrical conductivity is from the embedded Ag particles. However on interaction with test gases although the conductivity of PPy changes (due to reduction) but this change will not be reflected in the overall high conductivity of PPy-Ag samples. Similar finding were reported on the polyanniline—carbon nanotube composites, where the incorporation of the metallic carbon nano-tubes lowers the performance of the polyanniline films for ammonia [193].

Table 4.4: Comparison of the sensing properties of PPy-Ag films (of this work) with other reported PPy and their nanocomposites.

Support	**Active layer**	**Fabrication method**	**Detection limit**	**Sensitivity (at 20 ppm)**	**Response time (at 20 ppm)**	**Refer ences**
BOPET	PPy-Ag	Photopolymerisation	5 ppm	15	6 sec	This work
Resin	PPy-Ag	Chemical polymerization followed by Drop casting	10 ppm	38	20 sec	[166]
Pellet	$ZnSnO_3$ nanoparticle coated withPPy	Chemical polymerisation	50 ppm	40 (at 50 ppm)	20 sec	[194]
Glass	Carbon nanofiber coated with PPy	Vapor deposition and chemical polymerisation	10 ppm	150	10 sec	[195]
Ceramic	PPy-Pd composites	Vapor phase polymerisation	50 ppm	13 (at 50 ppm)	14 sec	[196]
Glass	PPy	Chemical polymerisation	5 ppm	8	15 sec	[191]
Silicon	PPy	Electrodeposited	10 ppm	8	150 sec	[197]

The gas sensing results obtained in this work is compared with the reported literature for other PPy based nanocomposites in Table 4.4. From this table it can be seen that PPy-Ag nanocomposite films based sensor shows the lowest detection limit of 5 ppm with a reasonably good sensitivity and very low response time ~ 6 sec (at 20 ppm). The recovery time of these films is high (~ 80 min at 20 ppm) and the possible reason could be the porous morphology (shown in Figure 4.6(b)) of these particular films, because of which the gas molecules can easily penetrates deep in films. The slow desorption of the gas molecule from these deep interaction sites is responsible for slow response. In fact this is reflected in the recovery part (inset of Fig. 4.19 (a)), which has two components one is initial fast rise of conductance (i.e. related to desorption of NH_3 from the surface) and next is slow rise of conductance (i.e. related with desorption of NH_3 from the bulk). The recovery time of these PPy- Ag films can be improved by increasing their density so that NH_3 interacts only at surface and does not penetrate into the bulk. From application point of view the faster response of these PPy-Ag films can have an advantage in case of any gas leakage accident. To the best of our knowledge, this is first ever report on H_2S detection using PPy based conducting polymer films. Earlier polyaniline and its nanocomposites samples were widely reported for detection of H_2S [198]. Since the toxicity limit of NH_3 and H_2S gas are 25 ppm and 10 ppm respectively, therefore reliable detection of these gases in ppm level using flexible PPy-Ag films makes them attractive candidates for gas sensing application. More important, these PPy-Ag films are highly adherent and flexible in nature, therefore can have longer operating life.

4.7 Conclusions

In summary, we have modified the surface of BOPET substrates by silanisedpyrrole for the anchoring of PPy-Ag nanocomposite films via photopolymerization. The effect of UV exposure time and $AgNO_3$ concentration on morphology, electrical conductivity, and gas sensing properties of PPy-Ag nano-composite films were studied in detail. The XPS and XRD measurement confirms the presence of metallic Ag crystallite of size ~ 80-120 nm in the films. The XPS results show that these films are undoped. The increase in conductivity with UV exposure time or with increasing $AgNO_3$ concentration is attributed to increasing conjugation length, incorporation of Ag at grain/grain boundaries, which is confirmed by FTIR and RAMAN spectroscopy. GIXRD measurements confirm the role of silanised-pyrrole layer in improving the structural ordering of PPy-Ag nanocomposites. The films with least amount of Ag (0.1M) only shows a reversible conductivity change in opposite manner on exposure to ppm level of H_2S and NH_3 gases. We have conclusively shown that UV induced polymerization is a simple and efficient route towards synthesis of polymer-metal nanocomposite films with controlled physicochemical (*e.g.* structural ordering) and gas sensing properties.

Chapter -5

Flexible OFETs based on PCDTBT

In this Chapter we demonstrate fabrication of flexible field-effect transistors (FETs) using poly[N-9'-heptadecanyl-2,7-carbazole-alt-5,5-(4',7'-di-2-thienyl-2',1',3'-benzothiadiazole)], PCDTBT, as an active channel, poly(methyl methacrylate) (PMMA) as gate dielectric and biaxially oriented polyethyleneterephthalate (BOPET) as supporting substrate. The output and transfer characteristics of the devices were measured as a function of channel length. It has been observed that various OFET parameters viz. on-off ratio ($\sim 10^5$*), mobility (*$\mu \sim 10^{-4}$ $cm^2V^{-1}s^{-1}$*), threshold voltage (*$V_{th} \sim$ -14 V*), switch-on voltage (*$V_{so} \sim -6$ V*), subthreshold slope (S ~7 V/decade) and trap density (*$N_{it} \sim 10^{12}$ $cm^{-2}V^{-1}$*) are almost independent of the channel length, which suggested a very high uniformity of the PCDTBT active layer. These devices were highly stable under atmospheric conditions (temperature: 20-35*^oC* and relative humidity: 70-85%), as no change in mobility was observed on a continuous exposure for 70 days. The studies on the effect of strain on mobility revealed that devices are stable up to a compressive or tensile strain of 1.2%. These results indicate that PCDTBT is a very promising active layer for the air stable and flexible FETs.In addition, we demonstrate the gas sensing characteristics of OFETs.*

5.1 Overview of current research on OFETs

Recently, a significant amount of research has been reported on the flexible organic field-effect transistors (OFETs), which are based on both small molecules as well as conducting polymers. The current research on flexible OFETs, as summarized in Table 5.1, is mainly focused on following issues: (i) Enhancement of charge carrier mobility of the active layer; (ii) Long-term stability against the environmental exposures; and (iii) Enhanced electro-mechanical stability i.e. flexible OFET's must exhibit mechanical flexibility without any degradation of its electrical properties. As is evident from Table 5.1, OFETs have been fabricated using a combination of different active layers, dielectric, substrates and device geometries i.e. bottom gate bottom contact (BGBC), top gate bottom contact (TGBC), bottom gate top contact (BGTC) and 3-dimensional [47, 60, 199-210]. It has been found that the small molecules based p-channel OFETs exhibit better mobility as compare to n-channel OFETs. A highest hole mobility of 23.2 cm^2/Vs has been obtained using pentacene based OFET fabricated in BGTC configuration [207]. On the other hand, the highest mobility in conducting polymer based flexible OFETs has been 5.3 cm^2/Vs [60]. As seen from Table 5.1, there have been few studies pertaining to the air stability of the flexible OFETs. In general, the TGBC configuration should yield better air stability as the active layer is not exposed to the atmosphere [208]. On small molecules based OFETs, significant research has been done on the electro-mechanical studies and a bending radius upto 0.1 mm without degrading the charge carrier mobility has been reported [205]. However, in the case of conducting polymer based OFETs no studies on the electro-mechanical properties has been reported. Among various conducting polymers, poly[N-9'-heptadecanyl-2,7-carbazole-alt-5,5-(4',7'-di-2-thienyl-2',1',3'-benzothiadiazole)] (PCDTBT) based OFETs fabricated on rigid SiO_2 have exhibited a maximum air stability of 31-days [32]. However, the only report on the PCDTBT based flexible OFETs using ITO coated PEN substrates had low on/off ratio (~10^2) and their air stability and electromechanical properties were not investigated [202].

Table 5.1 Summary of the recently reported flexible organic field effect transistors and their mobility, air stability and bending properties.

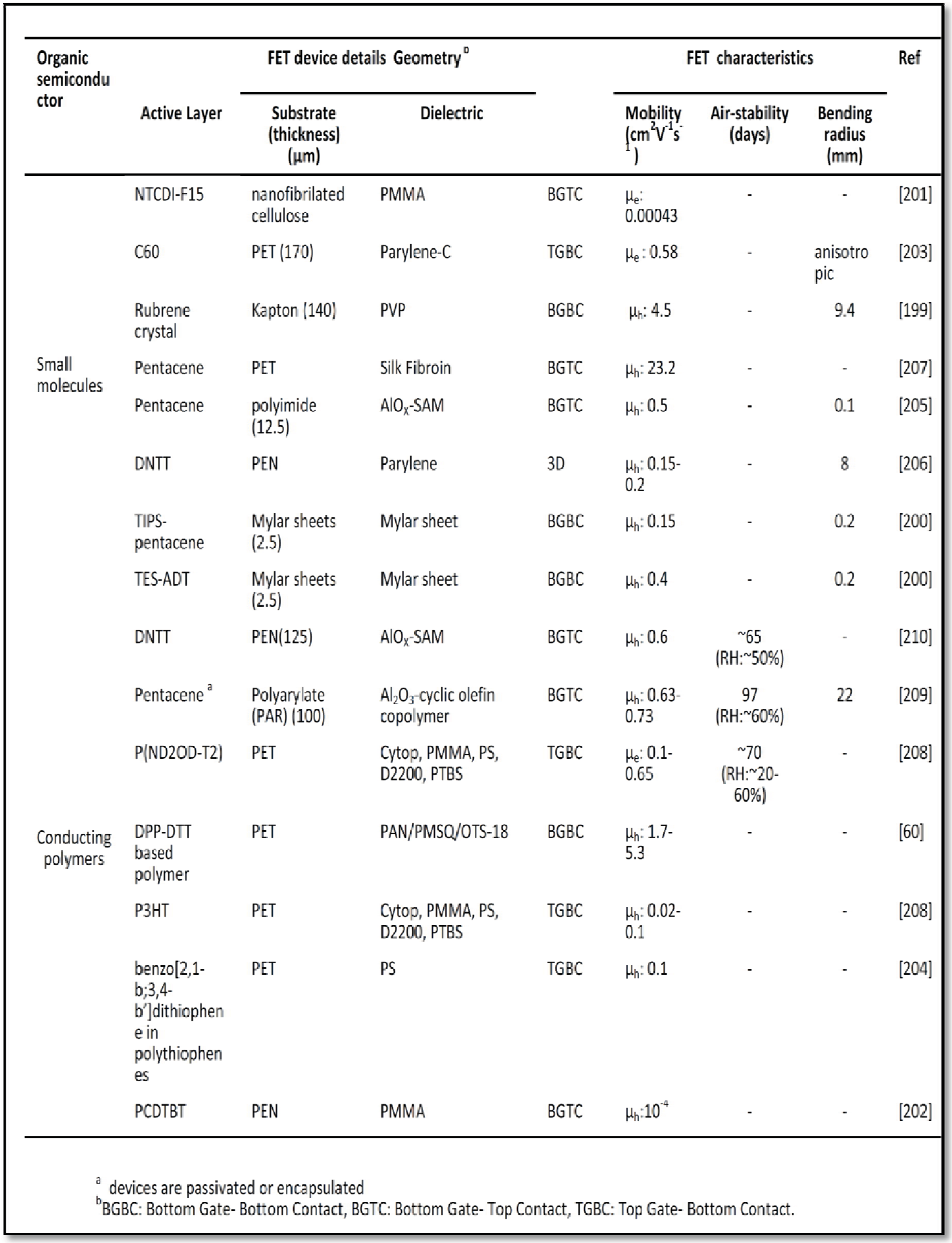

Organic semiconductor	FET device details			Geometry [b]	FET characteristics			Ref
	Active Layer	Substrate (thickness) (μm)	Dielectric		Mobility (cm^{2}V^{-1}s^{-1})	Air-stability (days)	Bending radius (mm)	
Small molecules	NTCDI-F15	nanofibrilated cellulose	PMMA	BGTC	μ_e: 0.00043	-	-	[201]
	C60	PET (170)	Parylene-C	TGBC	μ_e : 0.58	-	anisotropic	[203]
	Rubrene crystal	Kapton (140)	PVP	BGBC	μ_h: 4.5	-	9.4	[199]
	Pentacene	PET	Silk Fibroin	BGTC	μ_h: 23.2	-	-	[207]
	Pentacene	polyimide (12.5)	AlO$_x$-SAM	BGTC	μ_h: 0.5	-	0.1	[205]
	DNTT	PEN	Parylene	3D	μ_h: 0.15-0.2	-	8	[206]
	TIPS-pentacene	Mylar sheets (2.5)	Mylar sheet	BGBC	μ_h: 0.15	-	0.2	[200]
	TES-ADT	Mylar sheets (2.5)	Mylar sheet	BGBC	μ_h: 0.4	-	0.2	[200]
	DNTT	PEN(125)	AlO$_x$-SAM	BGTC	μ_h: 0.6	~65 (RH:~50%)	-	[210]
	Pentacene [a]	Polyarylate (PAR) (100)	Al$_2$O$_3$-cyclic olefin copolymer	BGTC	μ_h: 0.63-0.73	97 (RH:~60%)	22	[209]
Conducting polymers	P(ND2OD-T2)	PET	Cytop, PMMA, PS, D2200, PTBS	TGBC	μ_e: 0.1-0.65	~70 (RH:~20-60%)	-	[208]
	DPP-DTT based polymer	PET	PAN/PMSQ/OTS-18	BGBC	μ_h: 1.7-5.3	-	-	[60]
	P3HT	PET	Cytop, PMMA, PS, D2200, PTBS	TGBC	μ_h: 0.02-0.1	-	-	[208]
	benzo[2,1-b;3,4-b']dithiophene in polythiophenes	PET	PS	TGBC	μ_h: 0.1	-	-	[204]
	PCDTBT	PEN	PMMA	BGTC	μ_h:10^{-4}	-	-	[202]

[a] devices are passivated or encapsulated

[b] BGBC: Bottom Gate- Bottom Contact, BGTC: Bottom Gate- Top Contact, TGBC: Top Gate- Bottom Contact.

In this Chapter, for the first time we demonstrate the long term stability and electro-mechanical properties (strains applied perpendicular as well as parallel) of PCDTBT based flexible OFETs fabricated using biaxially oriented polyethyleneterephthalate (BOPET) flexible substrates. The on-off ratio of the PCDTBT based OFETs were ~10^5. These devices were stable under atmospheric conditions upto 70 days. In addition, the electro-mechanical studies show that the mobility remains unchanged up to a compressive or tensile strain of 1.2%.

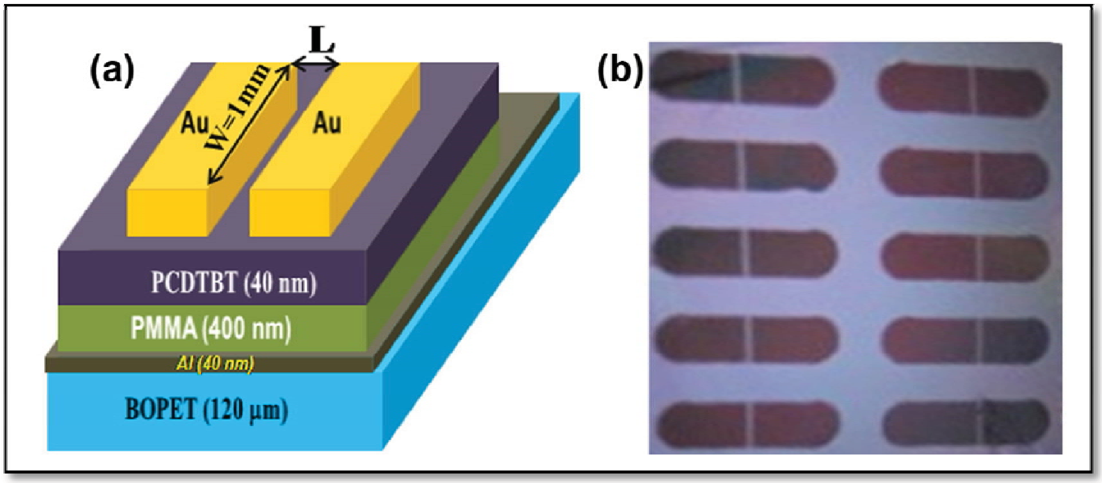

Fig. 5.1 (a)Schematic showing the bottom-gate top-contact configuration used for the fabrication of all polymer flexible PCDTBT based FETs. (b) Photograph of a typical 2×5 array of the fabricated flexible OFETs. In this particular case, the channel width (W) is 1 mm and channel length (L) is 50 μm.

5.2 Fabrication process of OFET

Fig.5.1 (a) shows the schematic structure employed for the fabrication of OFETs in the present work, which essentially is a bottom-gate top-contact configuration. The fabrication process of OFETs is shown in Fig. 2.4 and discussed in Chapter 2. The low rms roughness (~1 nm) of the BOPET substrate is useful in making good dielectric and active layer films [107]. The entire device fabrication was carried out under Ar atmosphere using

MBraun glove box having oxygen and moisture levels of <1ppm. First, the gate electrode was deposited by depositing aluminium (thickness: ~40nm) layer onto BOPET substrates by thermal evaporation. The PMMA dielectric layer (thickness: ~400 nm) was spin coated onto Al/BOPET using 80mg/ml PMMA solution (prepared in PGMEA) at 1000 rpm for 80 s followed by an annealing at 140^{o}C for 30min. The PCDTBT (Mw = 36.5 kDa; PDI = 2.16) active layer (thickness: ~40 nm) was spin-coated onto PMMA/Al/BOPET using a 10 mg/ml PCDTBT solution (prepared in 1,2-dichlorobenzene and filtered using 0.45 micron filters) at 4000 rpm for 60 s followed by an annealing at 140^{o}C for 30min.The device structure was completed by thermally depositing several pairs of source(S)-drain(D) gold electrodes using a stainless steel shadow mask. The channel length (L) of the devices varied between 12 and 100 µm while the channel width (W) was kept constant at 1mm. For each channel length, minimum of 8-10 devices were fabricated. The photograph of the fabricated devices is shown in Fig. 5.1(b). In order to measure the capacitance of the dielectric layer, an Al/PMMA/Al(BOPET) sandwich structure was fabricated by depositing Al electrode (area: 0.025 cm^{2}) onto PMMA coated Al(BOPET).

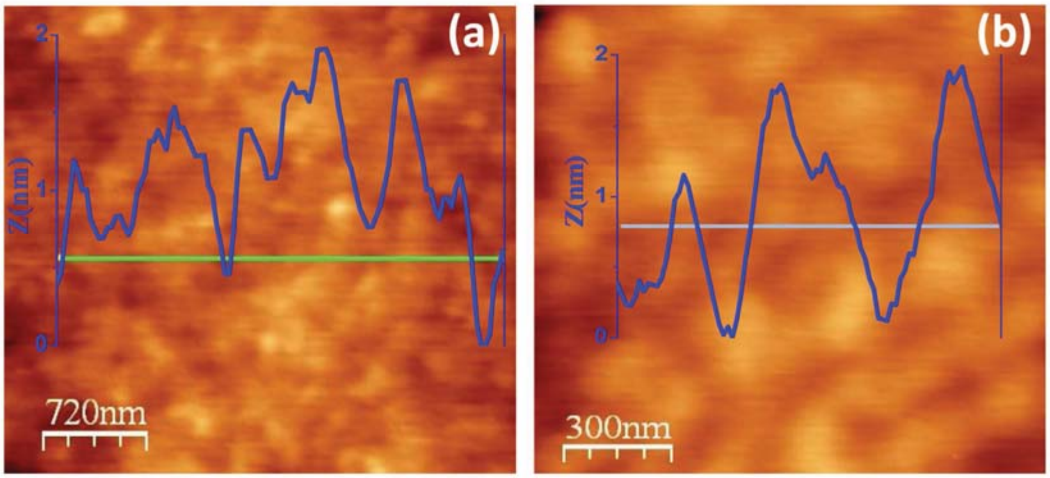

Fig. 5.2: AFM images recorded at (a) higher and (b) lower magnifications for the active PCDTBT layer, which was spin coated on PMMA/Al/BOPET and at annealed 140^{o}C for 30min.

5.3 Characteristics of active PCDTBT layer

5.3.1 AFM studies

Fig. 5.2 shows AFM images recorded at different magnifications for the active PCDTBT layer that was spin-coated on PMMA/Al/BOPET and annealed at 140°C for 30 min. The image recorded at lower magnification, as shown in Fig. 5.2 (a), revealed that there are no pinholes in the layer, indicating that the deposited PCDTBT layer is suitable for the FET fabrication. The image recorded at higher magnification, as shown in Fig. 5.2(b), shows the granular morphology of the layer with an average grain size of ~150 nm. The analysis of the height profiles revealed that the rms roughness of the layer is ~1.2 nm.

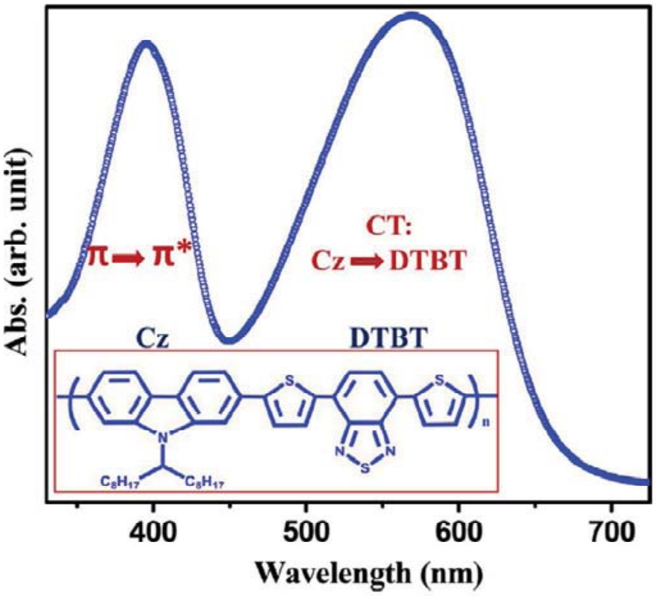

Fig. 5.3 UV-Vis absorption spectrum recorded for the PCDTBT layer. The inset shows the molecular structure of PCDTBT.

5.3.2 UV/Vis and Raman studies

Fig. 5.3 shows the UV-Vis absorption spectrum of the active PCDTBT layer and its inset shows the molecular structure of PCDTBT that consists of two parts: donor carbazole

(Cz) and acceptor dithienylbenzothiadiazole (DTBT). The UV/Vis spectrum clearly shows two absorption bands at 395 and 570 nm. The absorption at 395 nm is attributed to π-π* transition, whereas absorption at 570 nm is known to be due to a charge transfer from donor Cz unit to acceptor DTBT unit [211].

The Raman spectrum of the PCDTBT layer is shown in Fig. 5.4. Several peaks at 841, 871,884(sh), 1062, 1136, 1270, 1349, 1373, 1444, 1541, 1529(sh) cm^{-1} have been observed. The origin of the important peaks is as follows: the 1541 cm^{-1} mode corresponds to the benzothiadiazole ring stretching mode, and the 1444 cm^{-1} mode assigned to a broad ring stretch focused on the DTBT acceptor unit that is delocalized across the benzothiadiazole and the two thiophenes. Peaks at 1349 and 1373 cm^{-1} are attributed to the C–C stretching mode of the carbazole and DTBT unit, respectively [211].

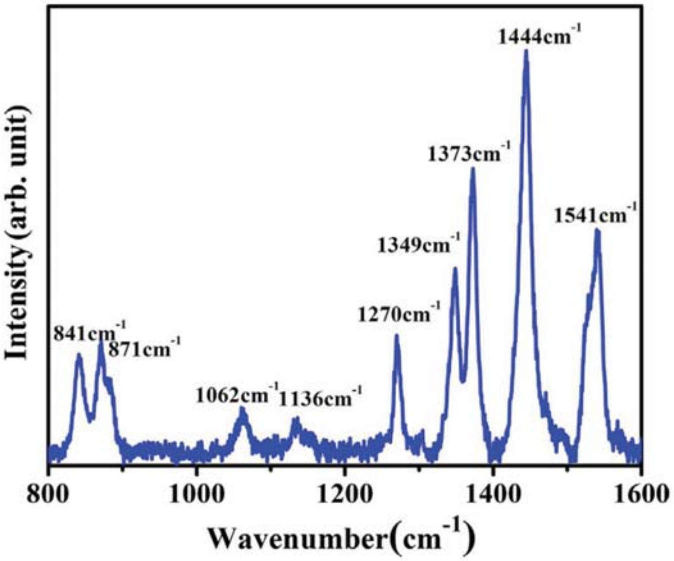

Fig. 5.4: Raman spectrum of the active PCDTBT layer.

5.3.3 XPS studies

Typical N 1s, C 1s and S 2p spectra recorded for the PCDTBT active layer is shown in Fig. 5.5. The N 1s spectrum could be resolved into two components at 399.9 and

400.7eV, which are attributed to the N in benzothiadiazole and carbazole units, respectively [32, 212, 213]. The core level C 1s spectrum reveals presence of three peaks at 284.9, 285.5 and 286.4 eV, which can be assigned respectively to C-C bonds, C-H bonds (e.g., CH_2 chains, hydrocarbons and aromatic carbons) and C-N and/or C-S bonds 34. For S 2p spectrum, presence of four peaks is attributed to two different sulfur species: the first doublet i.e. 164.5 eV (S $2p_{3/2}$) and 165.6 eV (S $2p_{1/2}$) due to thiophene and the second doublet 165.9 eV (S $2p_{3/2}$) and 167.1 eV (S $2p_{1/2}$) due to benzothiadiazole [32]. These assignments are consistent with the binding energies reported for S $2p_{3/2}$ in unbound thiophene (~164 eV) and benzothiadiazole (~166 eV) [214-216].

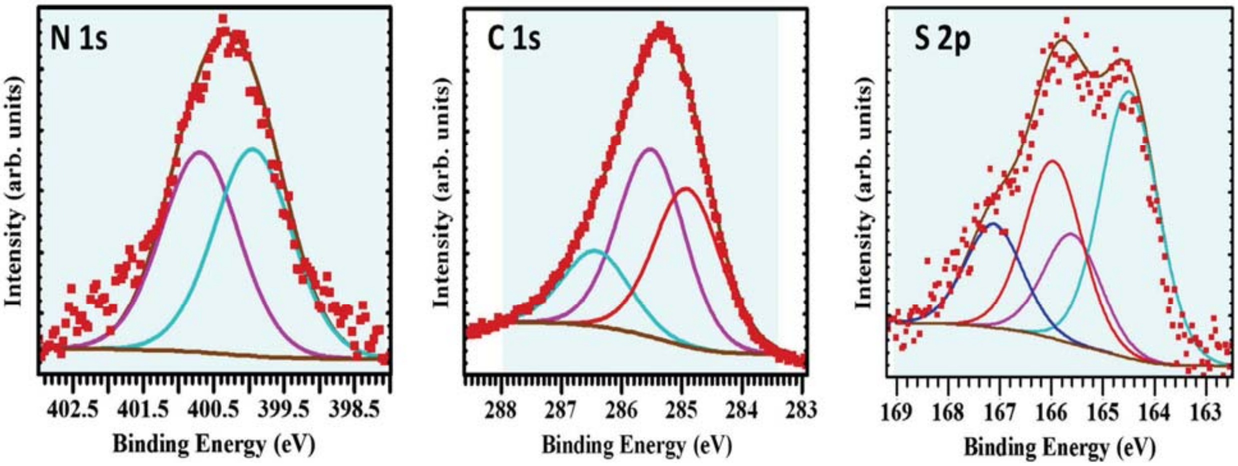

Fig. 5.5: XPS spectra of the active PCDTBT layer showing core level N 1s, C 1s and S 2p peaks with resolved components.

From the results of the AFM, UV/Vis, Raman and XPS studies it is evident that the active PCTDBT layer deposited on the PMMA/Al/BOPET is pinholes free, smooth and does not show any signature of the chemical modification even after annealing at 140^{o}C for 30min. This inference is in agreement with the literature report that the electronic structure of PCDTBT is stable after exposure to temperatures as high as 150^{o}C in air [32].

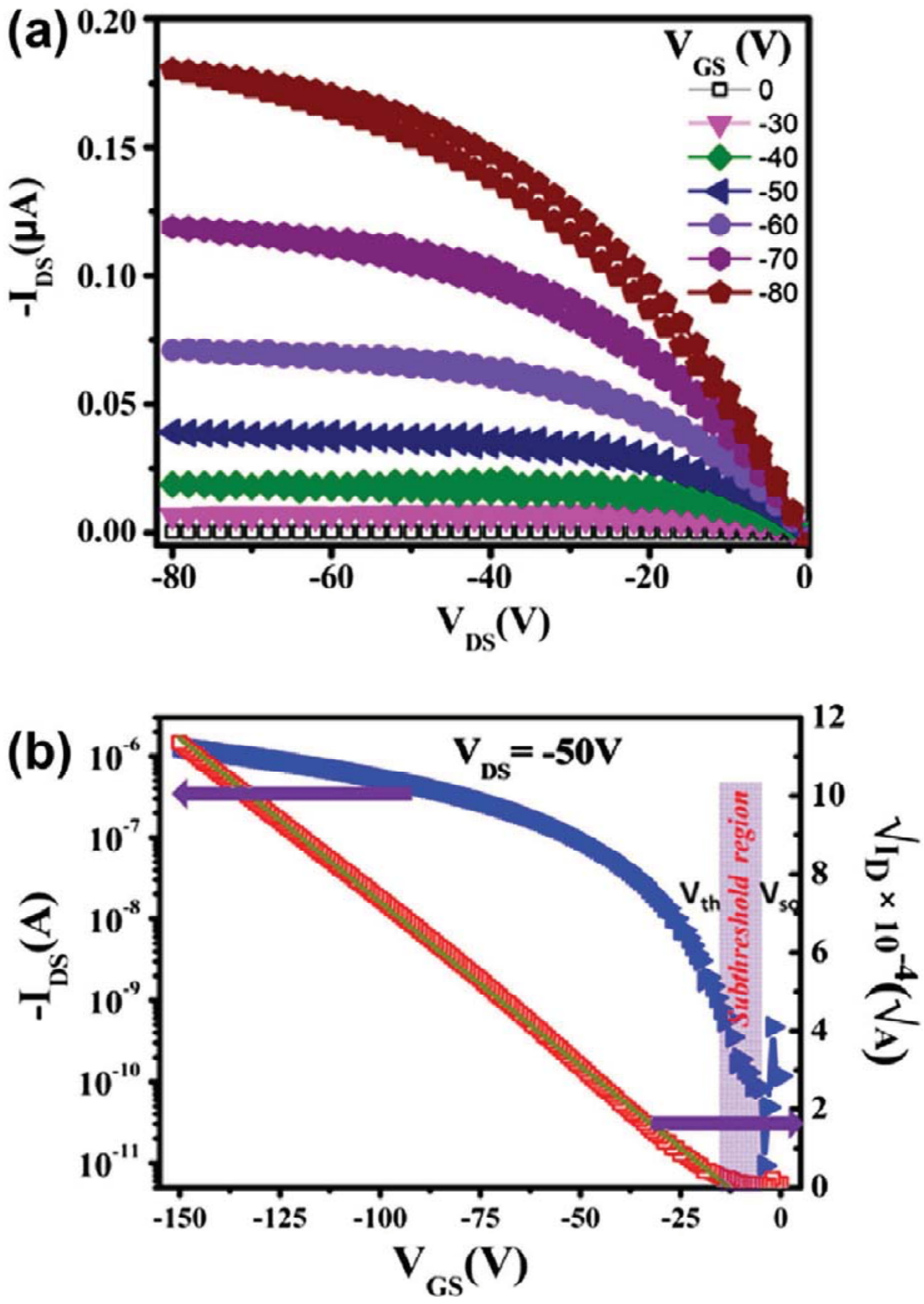

Fig.5.6: Device characteristics of a typical OFET with channel length of 12µm and channel width of 1mm. (a) Output characteristics i.e. variation of drain source current (I_{DS}) with the drain-source voltage (V_{DS}) from 0 to -80 V at different gate-source voltages (V_{GS}); (b) Left scale: Transfer characteristics in saturation region measured by varying the V_{GS} from 0 to -150 V while keeping V_{DS} constant at -50V. Right scale: $\sqrt{|I_{DS}|}$ vs. V_{GS} plot. The shaded area shows subthreshold region that lies between threshold voltage (V_{th}) and switch-on voltage (V_{so}).

5.4 OFET characteristics

5.4.1 Output and transfer characteristics

Fig. 5.6 shows the typical output and transfer characteristics of the fabricated PCDTBT based flexible FET devices having a channel length of 12 µm. The measurements were carried out at room temperature under ambient conditions. The output characteristics i.e. drain source current for the drain-source voltage (V_{DS}) range 0 to -80 V at different gate-source voltages (V_{GS}) (i.e. 0, -30, -40, -50, -60, -70 and -80V) is shown in Fig. 5.6 (a). The output characteristics show almost no or very little hysteresis, suggesting very low density of deep traps [217]. It has been reported that the chemisorbed oxygen in the organic semiconductors acts as deep traps, which is reflected in strong hysteresis in the current-voltage characteristics [217]. Near absence of hysteresis in the present case indicate that PCDTBT does not react with ambient oxygen, which is a good sign from the view point of its application in air stable OFETs. The output characteristics correspond to p-type behaviour i.e. accumulation of holes at the interface of active layer and dielectric on application of a negative gate-source voltage.

Typical transfer characteristics measured for a FET with L=12 µm are shown in Fig. 5.6(b), which was measured by varying the V_{GS} from 0 to -150 V while keeping V_{DS} constant at -50V (i.e. in saturation region). It is seen from this figure that the drain current varies between -10^{-11} and -10^{-6} A (for V_{DS}= -50V). The on-off ratio (average of 8-10 devices) – a ratio between the maximum drain current (on-state of the transistor) and the minimum drain current (off-state) - for the OFETs of different channel length is summarized in Table 5.2. It is seen that the on-off ratio is almost independent of the channel length and is of the order of 10^5, which is higher by three orders in magnitude as compared to those OFETs fabricated on ITO-coated PEN substrates [202]. The improved on-off ratio in the present case can be attributed to the use of Al as gate electrode and the low rms roughness of the BOPET substrate.

Table 5.2: Summary of various FET parameters e.g. mobility (μ), on-off ratio, threshold voltage (V_{th}), switch-on voltage (V_{so}), subthreshold slope (S), and trap density (N_{it}) measured as a function of channel length (L). The reported values are an average of 8-10 devices.

L (μm)	**On-off ratio**	**μ** ($cm^2V^{-1}s^{-1}$)	**V_{th}** (V)	**V_{so}** (V)	**S** (V/decade)	**N_{it}** ($cm^{-2}V^{-1}$)
12	$1.4\pm0.2\times10^{5}$	$2.1\pm0.1\times10^{-4}$	-13.2±0.8	-4±1	8.8±0.3	$7.0\pm0.3\times10^{12}$
25	$9.2\pm0.3\times10^{4}$	$2.3\pm0.1\times10^{-4}$	-14.1±0.7	-6±1	7.9±0.3	$6.3\pm0.3\times10^{12}$
50	$1.5\pm0.2\times10^{5}$	$2.5\pm0.2\times10^{-4}$	-14.9±0.6	-5±1	8.6±0.2	$6.9\pm0.4\times10^{12}$
100	$9.5\pm0.3\times10^{4}$	$2.4\pm0.2\times10^{-4}$	-14.8±0.7	-7±1	6.6±0.4	$5.3\pm0.4\times10^{12}$

5.4.2 Field effect mobility, subthreshold voltage and density of trap states

The field-effect μ in the saturation region was calculated from the slope of the square root of the drain-source current as a function of the gate-source voltage i.e. $\sqrt{|I_{DS}|}$ vs. V_{GS} plot, as shown in Fig. 5.6(b), using the equation:

$$\mu_{sat} = \frac{2L}{WC_i}\left(\frac{\partial\sqrt{I_{DS}}}{\partial V_{GS}}\right)^2 \qquad 5.1$$

where C_i is the gate dielectric capacitance per unit area. In the present case, the value of C_i for PMMA dielectric was measured to be ~8±1 nF/cm^2. The calculated μ values for different channel length OFETs are summarised in Table 5.2. It is seen that the μ value lies in range between 2.1×10^{-4} and 2.5×10^{-4} $cm^2V^{-1}s^{-1}$. The values, though low, are independent of the channel length. For the PCDTBT based OFETs fabricated on SiO_2 dielectric, Cho et al. have found that the μ increases with increasing the molecular weight of PCDTBT. In addition, the annealing temperatures of the devices had a strong influence on μ. For the device fabricated using PCDTBT of 62 kDa molecular weight and annealed at 170°C, they obtained a μ value of ~2×10^{-2} $cm^2V^{-1}s^{-1}$ [32]. Low values of μ in our case can be attributed to: (i) low molecular weight PCDTBT (i.e. 37 kDa); (ii) amorphous and disordered nature of PCDTBT active layer, and therefore, the obtained μ value in our case is same as that typically reported for other amorphous conjugated polymers, such as, polythiophene or polyacetylene [20, 47]; and (iii) a poor quality of PMMA/PCDTBT interface, which can lead to a large trap density (and this is described below).

As shown in Fig. 5.6(b), the extrapolation of fitted straight line of $\sqrt{|I_{DS}|}$ vs. V_{GS} plot to I_{DS}=0 gives the threshold voltage (V_{th}). The switch-on voltage (V_{so}) was determined from log I_{DS} vs. V_{GS} plot, where the I_{DS} attains a minimum. The values for V_{th} and V_{so} measured for FETs of different channel lengths are summarized in Table 2, which are found to be in the range -13.2 to -14.9 V and -4 to -7 V, respectively. Interestingly, both V_{th} and V_{so} are almost independent of the channel length. These values are on higher side, which can be attributed to low dielectric constant of PMMA dielectrics (*k* ~3.5) [218]. It has been reported that the V_{th} can be increased if the thickness of PMMA gate dielectric is decreased [218, 219]. Unfortunately, we observed a high gate leakage through the PMMA dielectric at lower thicknesses. It may be mentioned here that PMMA contains hydrophobic methyl radical groups, which can play a role as moisture inhibitors, and therefore the air stability of the OFETs.

The region between V_{so} and V_{th} is known as subthreshold region, whereby I_{DS} is mainly governed by the carriers that have sufficient thermal energy to overcome the V_{GS}-controlled energy barrier at the source contact, which eventually diffuse to the drain contact [47]. In this region, I_{DS} depends exponentially on the V_{GS} via equation [47]:

$$I_{DS} = I_0 e^{\left(\frac{q|V_{GS}-V_{FB}|}{nkT}\right)} \qquad 5.2$$

The slope of the log (I_{DS}) versus V_{GS} plot is usually quantified as the inverse subthreshold slope (S) (known as subthreshold swing) and is expressed as:

$$S = \frac{\partial V_{GS}}{\partial(\log_{10} I_{DS})} = \frac{nkT}{q}\ln 10 \qquad 5.3$$

where *n* is ideality factor, *T* is temperature, *q* is electronic charge and *k* is Boltzmann's constant [47]. The *n* is determined by the density of trap states at the semiconductor/dielectric interface (N_{it}), and C_i via equation

$$n = 1 + \frac{qN_{it}}{C_i} \qquad 5.4$$

Thus, S can be written as:

$$S = \frac{kT}{q}\ln 10\left(1 + \frac{qN_{it}}{C_i}\right) \qquad 5.5$$

The calculated values of *S*, extracted from the slope of the log(I_{DS}) versus V_{GS} plot (equation 2), and N_{it} (calculated using equation 5) are summarized in Table 5.2. The obtained values of S (6.6 to 8.8 V/decade) and N_{it} (5.3×10^{12} to 7×10^{12} $cm^{-2}V^{-1}$) are relatively high, which can be attributed to a poor quality of PMMA/PCDTBT interface as the device fabrication was done at room temperature. Also both S and N_{it} are found to be independent of the channel length.

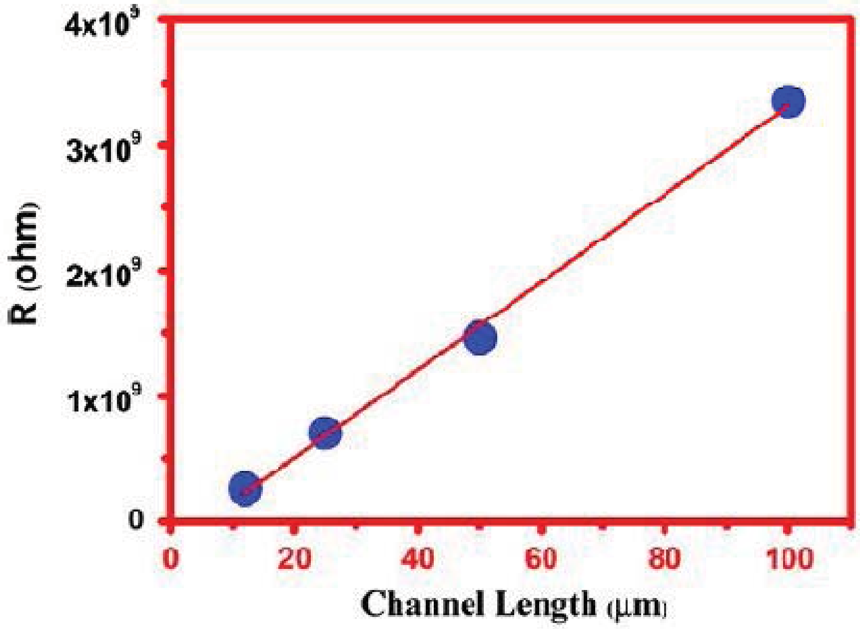

Fig. 5.7: Plot of channel resistance (R) of the FETs in the linear region i.e. for a constant V_{DS}= -10V, as function of channel length (L) at a constant V_{GS}= -60V.

The above discussion and data of Table 5.2 clearly demonstrate that the PCDTBT based flexible FETs exhibit very reproducible device parameters. The independence of almost all the device parameters (i.e. on/off ratio, μ, V_{th}, V_{so}, S and N_{it}) on the channel length indicates the active PCDTBT layers exhibit uniform morphological, structural and electrical properties over a large area. To confirm this, we have measured the resistance of the PCDTBT channel in the linear region (i.e. for a constant V_{DS}= -10V) as function of its length (for a constant V_{GS}= -60V) and the result is shown in Fig. 5.7. It is evident that the resistance linearly increases with channel length, which confirms the high uniformity of the sample.

5.5. Environmental stability of OFETs

Apart from stable device parameters, long term stability of FETs under ambient conditions is another key issue from application point of view. It is known that many organic semiconductors are prone to redox reactions with oxygen and moisture present in ambient atmosphere. These redox reactions generate defects in organic semiconductors, which are responsible for the degradation of the device properties [220]. We have investigated the long term air stability of the PCDTBT based flexible FET devices by measuring output and transfer characteristics as a function of time, while continuously exposing the devices to the ambient conditions (temperature: 20-35^{0}C and relative humidity: 70-85%). From these data the relative mobility (μ_t/μ_0, where μ_t and μ_0 are the mobility at time t and that of the fresh sample, respectively) was calculated as a function of time for which the devices were exposed to ambient conditions and the obtained results are plotted in Fig. 5.8.

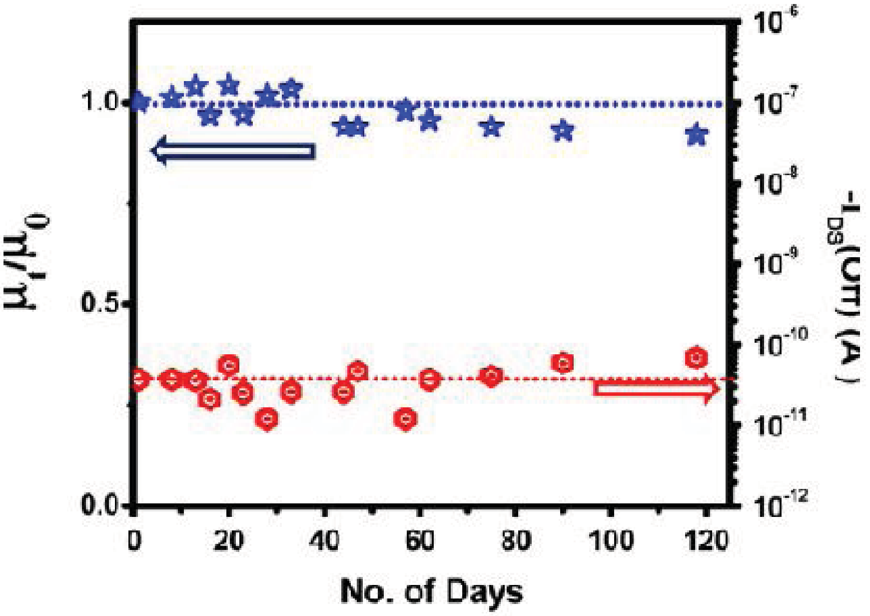

Fig.5.8: Plots of the relative mobility (μ_t/μ_0, where μ_t and μ_0 are the mobility at time t and that of the fresh sample, respectively) and I_{DS}(off) as a function of air exposure time in days (temperature: 20-35ºC and relative humidity: 70-85%).

It was found that up to 70 days there was no effect on the μ_t/μ_0, which marginally decreased to a value of 0.92 after 118 days. Similarly, as shown in Fig. 8, the I_{DS} in the off state remains nearly constant at 3.7×10^{-11} A for 70 days, which marginally increased to 7.75×10^{-11} A after 118 days. This indicates that doping of PCDTBT by ambient oxygen or moisture is almost negligible. Moreover, the trends for μ_t/μ_0 and I_{DS}(off) as a function of time remained more or less same for the devices of different channel lengths. These results show that PCDTBT based flexible FET devices are quite stable under the atmospheric conditions.

The good environmental stability of the devices is attributed to following two factors.

(i) *Amorphous morphology of the active PCDTBT layer*. Amorphous morphology, though leading to poor mobility, provides a uniform path for charge transport along which charge carriers experience a minimum degree of site-energy fluctuations, which in turn is responsible for the improved environmental stability. In literature, as discussed in the Introduction, very high mobility has been obtained for the crystalline conducting polymers [20]. However the improved crystallinity often leads to charge trapping (mainly due to the chemisorbed oxygen and moisture when operated under ambient conditions) in the organic semiconductor and/or at the active interface, which is mainly responsible for their poor stability. It may be noted here that the PCDTBT based OFETs fabricated on SiO_2 dielectric by Cho et al. exhibited a decrease in mobility by a factor of 2-3 over 31 days of exposure to air, which is far inferior as compared to our devices. Since the devices on SiO_2 dielectric were fabricated using high molecular weight PCDTBT at high annealing temperatures, it is quite possible that the active layer might have some crystallization, which resulted in high mobility values, but at the same time, exhibited relatively poor environmental stability [32].

(ii) *Large ionization potential PCDTBT* i.e. the energy of the highest occupied molecular orbital (HOMO) is relatively low (~5.5 eV below the vacuum), which indicates that this material is inherently stable against the oxidation. This is also supported by the no-hysteretic output characteristics of the FETs shown in Fig. 5.6 (a).

5.6 Electromechanical properties of OFETs

The electromechanical properties of PCDTBT based flexible OFET devices were investigated under both compressive as well tensile strain conditions. The strains were applied parallel as well as perpendicular to the channel length. For this purpose, devices were bent to various radius of curvatures (*r*) at room temperature, as schematically shown in the inset of the Fig. 5.9, and the mobility was measured as a function of bending radius or strain. For calculation of strain (ε) the following approximated formula was used:

$$\varepsilon(\%) = \left\{\left(\frac{d}{2r}\right) \times 100\right\} \qquad 5.6$$

where d is the thickness of flexible substrate (120 µm in the present case) and r is the radius of curvature [203].

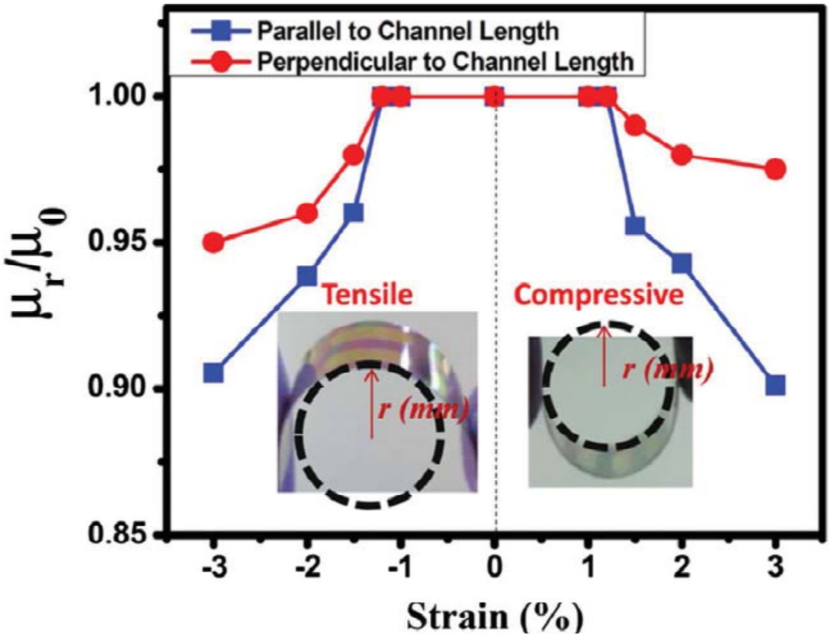

Fig. 5.9: Plot showing the variation in relative mobility (μ_r/μ_0, where μ_r and μ_0 are the mobility at bending radius r and under the flat condition, respectively) as a function of compressive and tensile strains, which were applied parallel and perpendicular to the channel length.

Fig. 5.9 shows the variation in relative mobility (μ_r/μ_0, where μ_r and μ_0 are the mobility at bending radius *r* and under the flat condition, respectively) as a function of tensile/compressive strains, which were applied parallel and perpendicular to the channel length. It is seen that both compressive and tensile strains lead to almost similar behaviour. For tensile/compressive strains applied parallel to the channel length, no change in relative mobility was obtained up to 5 mm bending (i.e. strain of 1.2%); however, at higher strains, the relative mobility start decreasing and reaches to a value of 0.9 for a strain of 3% (r=2mm), which is quite respectable. A decrease in mobility on both compressive as well tensile strain conditions is quite unique to the PCDTBT active layer. This is because, for small molecule based OFETs, mobility increases for compressive strain while it decreases for tensile strain [203, 221]. This phenomenon for small molecules based OFETs is explainable as the molecules in the active layer are bounded via weak van der Waals forces as under compression the molecules come closer and under tensile molecules get far apart [221].

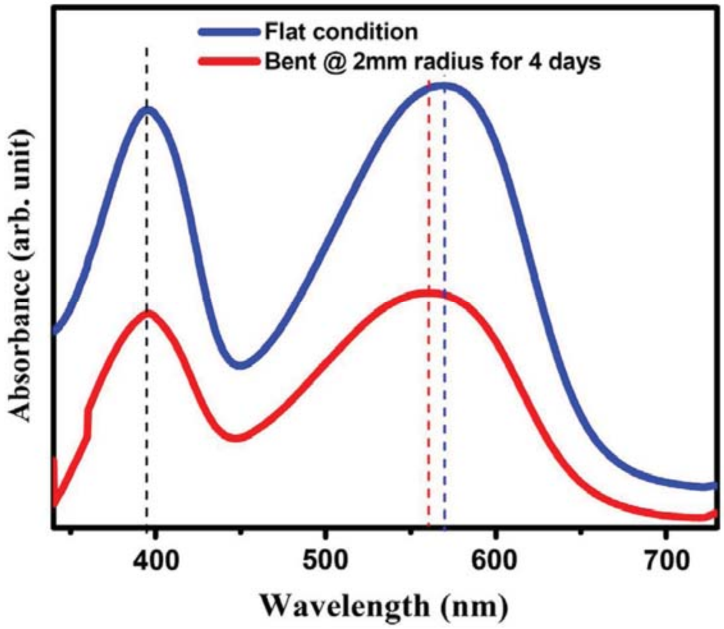

Fig.5.10: The UV-Vis spectra of PCDTBT film under the flat and tensile bend condition (at *r* = 2 mm for 4 days).

In order to investigate the decrease in mobility of PCDTBT based FET under both tensile and compressive strains, we have measured the UV/Vis spectrum under the flat and tensile bend condition (at r =2 mm for 4 days). The obtained results are shown in Fig. 5.10. It is seen that the absorption at 395 nm (π-π* transition) remains unaffected while the absorption at 570 nm (due to a charge transfer from donor Cz unit to acceptor DTBT unit) exhibit a blue shift. This indicates that under a prolonged strain (compressive or tensile), some conformational changes have occurred in the PCDTBT chains. These changes are found to be irreversible i.e. mobility does not revert back once the FET is bent for more than 5 mm. However, for bending radius ≤5 mm (i.e. strain of 1.2%), no degradation in mobility occurs, which would be sufficient for many flexible applications. However, as shown in Fig. 5.9, for tensile/compressive strains applied perpendicular to the channel length, the effect is less significant, which is due to the fact that the strain induced conformational changes in PCDTBT are not in the direction of the source-drain current.

5.7 Gas sensing characteristics of OFETs

To study the gas sensing properties of PCDTBT-FET devices with 50µm channel length and 1mm channel width were used. Operational stability of device under constant gate and drain bias is required for sensor fabrication. For this purpose drain current at -50V gate bias and -50V drain bias was measured as a function of time, as shown in Fig.5.11. Initially drain current decreases and then attained a constant value with no change up to ~4.5hours. This shows the suitability of the PCDTBT-FET for gas sensing applications.

PCDTBT-FET shows the maximum response for H_2S among various reducing gases and so H_2S sensing properties of PCDTBT-FET have been studied. The sensing properties were measured in saturation region. Fig. 5.12 shows the typical response-recovery curve of PCDTBT-FET for 100ppm of H_2S at constant gate and drain voltage of -50V. The response time is ~2 min while recovery time is ~7min. The sensitivity was found to be 430.

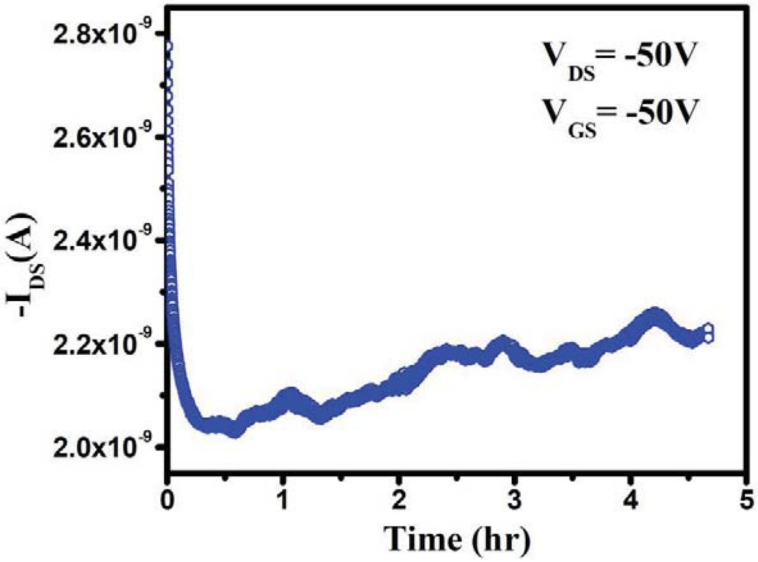

Fig.5.11:Stability of drain-source current at constant gate and drain-source bias.

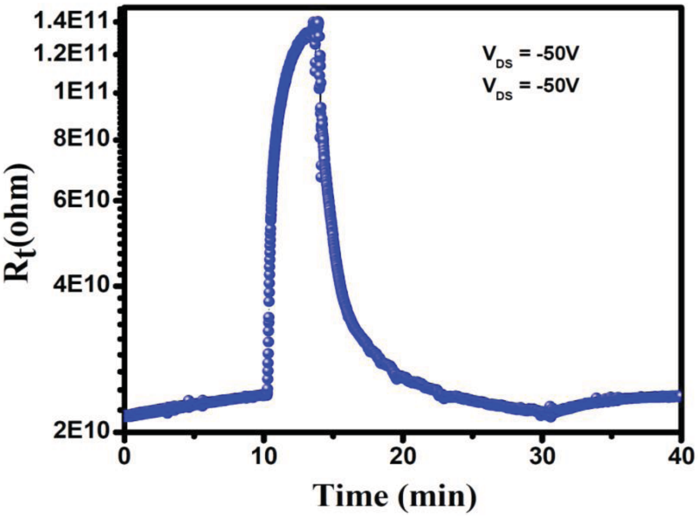

Fig.5.1: Response characteristics of PCDTBT-FET for 100ppm of H_2S

5.8 Conclusions

We have demonstrated fabrication of flexible PCDTBT based OFETs using BOPET substrates with high on-off ratio of 10^5. These devices were highly reproducible and the OFET parameters were found to be independent of the channel length, suggesting a very high uniformity of the PCDTBT layer. These devices were highly stable under the atmospheric conditions, as no change in mobility was observed on continuous exposure of the devices to atmosphere for 70 days. The studies on the effect of strain on mobility revealed that devices are stable upto a bending of 5 mm radius of curvature (both compressive as well as tensile). These results clearly indicate that PCDTBT is a very promising material for the air stable and flexible OFETs. We have also demonstrated the sensing characteristics of the fabricated OFETs.

Chapter -6

Summary

The semiconducting properties of conducting polymers has opened up a new area of applications in electronics, solar cells, chemical and bio-sensors, radiofrequency identifications tags, actuators etc. Conducting polymers differ from non-conducting polymers by the fact that they possess a conjugated backbone, i.e. alternating single and double bonds. The conjugation allows electrons and holes in the π-molecular orbitals to be delocalized along the conjugated segments of the molecule. However, since the conjugation is often broken by defects and twisting of the polymer chain, the charge carriers are localized within the conjugated segments. From this disorder in conjugation length, the HOMO and LUMO levels in organic semiconductors are not well defined but they have a Gaussian spread. The main transport mechanism in semiconducting polymers is dominated by hopping transport, which is strongly dependent on the energetic and structural disorder in the polymer. Due to disordered nature of conducting polymers, they have poor charge carrier motilities. Therefore it is almost certain that polymer electronics will probably never be able to compete with inorganic semiconductor electronics in terms of operation speed and miniaturization, until we discover a methodology to improve the ordering and charge carrier mobility in conducting polymers. Nevertheless, conducting polymers are currently in position to provide cheap, easy processable, flexible devices for low-end applications in electronics, such as, white light illumination, flexible displays, solar cells, RFID-tags and sensors.

Most of the conducting polymer electronic devices reported so far are fabricated on inorganic substrates that are rigid in nature, e.g. glass sheets and silicon wafers etc. Use of these rigid substrates has restricted the intrinsic flexibility of conducting polymers. Therefore, this thesis was aimed at the preparation and characterization of flexible thin films of conducting polymers. For this purpose we selected two conducting polymers: (i) polypyrrole, a widely studied one and (ii) PCDTBT, a new conducting polymer and not been fully investigated.

In order to prepare flexible thin films of PPy we have adopted two different strategies:

(a) synthesis of flexible freestanding PPy films by interfacial polymerization at liquid/air interface and

(b) Deposition of PPy films as well as nanocomposite films on flexible biaxially oriented bi-axially oriented polyethylene teraphthalate (BOPET) substrate.

In addition, we have investigated the charge transport of the flexible conducting polymer films, by measuring the temperature dependence of resistivity and current-voltage characteristics. These flexible polypyrrole and PCDTBT films were used as active channel for the fabrication of field effect transistors and chemiresistive sensors.

A summary of the main results is given below.

- A novel interfacial polymerization at liquid/air interface has been realized for the synthesis of freestanding polypyrrole films. In this method a solution consisting of 1mM porphyrin-derivative (TPPOH) and 0.01-1M pyrrole (Py) is dropped onto 0.1M aqueous $FeCl_3$ solution kept in a beaker. TPPOH/PPy bilayer forms spontaneously at the air/$FeCl_3$ interface, which after washing in dichloromethane yielded in free-standing PPy nanosheets. Detailed investigation revealed that TPPOH quickly forms J-aggregate films at air/$FeCl_3$ interface, which acts as an in-situ template for the growth of PPy nanosheets. The nanosheets were found to have a very dense morphology. These nanosheets are typically 100-150 nm thick and the diameter is of the size of the beaker containing $FeCl_3$. This method therefore allows formation of very large diameter PPy nanosheets.
- The room temperature conductivity of polypyrrole sheets synthesized without and with TPPOH template were respectively, 5×10^{-6} and 3×10^{-5} Scm^{-1}. Lower conductivity of the polypyrrole nanosheets prepared using TPPOH template indicate the improved conjugation compared to that synthesized without template.
- The charge carrier mobility (μ) at 300K was found to be $5.34x10^{-5}$ $m^2V^{-1}s^{-1}$. The low mobility indicates presence of disorder in the polypyrrole nanosheets. The

temperature dependence of is found to obey the Arrhenius behaviour i.e. $\ln \mu \sim 1/T$.

- The low temperature resistivity measurements indicated that charge transport occurs via variable range hopping conduction (VRH). The ratio of average hopping distance to localization length (R_{hop}/L_c) is found to be ~ 6, which indicated that carriers are strongly localized therefore making it close to the insulating region of M-I transition.
- Polypyrrole nanosheets exhibited an enhanced response towards NH_3 with typical response and recovery times (for 50 ppm) of 240 s and 50 min, respectively. This result suggests that these sheets can be used in ammonia sensors.
- We have fabricated first ever field effect transistors in top contact top gate geometry were fabricated using freestanding polypyrrole nanosheets as an active channel. The on-off ratio of the device was found to be ~20. However, there are still some issues pertaining to the mechanical strength of the device, which need to be improved.
- Freestanding polypyrrole films were also synthesized using another innovative method at air/liquid interface via acidic oxidation of terpyrrole. In this process, the non-conjugated chains get incorporated into the pyrrole matrix.
- The conductivity of these polypyrrole films is found to be ~10^{-7} Scm^{-1}, which are almost two orders of magnitude lower than those synthesized using TPPOH template. This is expected owing to the presence of non-conjugated chains in the polypyrrole matrix.
- Presence of non-conjugated chains in the polypyrrole matrix causes large hysteresis in current-voltage characteristics along with negative differential resistance region, which is unique to these freestanding polypyrrole films.
- The hysteretic current-voltage characteristics were gainfully used for demonstration of resistive memory devices. The memory devices exhibited an on/off ratio of ~50. The memory effect has been attributed to the conformational

changes of non-conjugated polymer chains in the polypyrrole matrix. Our results are the first free-standing film based polymer memory devices.

- The flexible polypyrrole-silver nanocomposite films have been prepared on N-(3-trimethoxysilylpropyl)pyrrole modified biaxially oriented polyethylene terephthalate (BOPET) substrate by photopolymerisation of pyrrole using $AgNO_3$ as a photo-initiator.
- These nanocomposite films are well adherent, flexible and mechanical very strong. The room temperature electrical conductivity of these films is ~15 Scm^{-1}, which is attributed to the high conjugation length, incorporation of Ag nanoparticles and ordered structure due to the template effect of the silanised pyrrole layer.
- The polypyrrole-silver nanocomposite films show a reversible conductivity change in the opposite manner on exposure to ppm levels of H_2S and NH_3 gases. A mechanism has been proposed to explain these antagonistic responses for reducing gases.
- We have demonstrated fabrication of flexible field-effect transistors (FETs) using poly[N-9'-heptadecanyl-2,7-carbazole-alt-5,5-(4',7'-di-2-thienyl-2',1',3'-benzothiadiazole)], PCDTBT, as an active channel, poly(methyl methacrylate) (PMMA) as gate dielectric and biaxially oriented polyethyleneterephthalate (BOPET) as supporting substrate.
- The devices exhibit on-off ratio of ~10^5 and mobility of ~10^{-4} $cm^2V^{-1}s^{-1}$, which can be further improved.
- These devices were highly stable under atmospheric conditions (temperature: 20-35°C and relative humidity: 70-85%), as no change in mobility was observed on a continuous exposure for 70 days.
- The studies on the effect of strain on mobility revealed that devices are stable up to a compressive or tensile strain of 1.2%, indicating that PCDTBT is a very promising active layer for the air stable and flexible FETs.

The results of the present thesis clearly demonstrate the two types of flexible polypyrrole films i.e. free-standing polypyrrole and polypyrrole on flexible BOPET substrates have very interesting properties and can be used for various flexible applications, such as, memory devices, gas sensors, field affect transistors etc. The thesis also opens up several issues that can be carried out in the future.

(i) The mechanical strength of freestanding polypyrrole needs to be further improved. This can be achieved by enhancing the conjugation in the polypyrrole sheets via appropriate doping. Once the conjugation improves, the conductivity of the free-standing polypyrrole films will also improve.

(ii) The freestanding poly-pyrrole films can be used as a counter-electrode in the dye-sensitized solar cells (DSSC) as a replacement of expansive Pt electrode. In fact the initial results carried out in our group indicated that indeed freestanding polypyrrole are good counter-electrodes that yielded ~3.5% efficiency in DSSC [222].

(iii) The flexible polypyrrole films on BOPET substrates are mechanically very strong and the quality of the devices fabricated using them, such as, field-effect transistors, gas sensors etc. can be further improved by optimizing the growth parameters.

Bibliography

[1] J.G. Drobny, Polymers for Electricity and Electronics: Materials, Properties, and Applications, Wiley (2011).

[2] S. Ramakrishnan, Conducting polymers, Reson, 2 (1997) 48-58.

[3] H. Letheby, XXIX.-On the production of a blue substance by the electrolysis of sulphate of aniline, Journal of the Chemical Society, 15 (1862) 161-163.

[4] Hideo Akamatu, H. Inokuchi, Y. Matsunaga, Electrical Conductivity of the Perylene–Bromine Complex, Nature, 173 (1954) 168-169.

[5] P. W. Anderson, P. A. Lee, M. Saitoh, Remarks on giant conductivity in TTF-TCNQ, Solid State Communications, 13 (1973) 595-598.

[6] J. Ferraris, D. O. Cowan, V. Walatka, J. H. Perlstein, Electron transfer in a new highly conducting donor-acceptor complex, Journal of the American Chemical Society, 95 (1973) 948-949.

[7] D. Jérome, A. Mazaud, M. Ribault, K. Bechgaard, Superconductivity in a synthetic organic conductor $(TMTSF)_2PF_6$, J. Physique Lett., 41 (1980) 95-98.

[8] B. Bolto, R. McNeill, D. Weiss, Electronic Conduction in Polymers. III. Electronic Properties of Polypyrrole, Australian Journal of Chemistry, 16 (1963) 1090-1103.

[9] R. McNeill, R. Siudak, J. Wardlaw, D. Weiss, Electronic Conduction in Polymers. I. The Chemical Structure of Polypyrrole, Australian Journal of Chemistry, 16 (1963) 1056-1075.

[10] R. De Surville, M. Jozefowicz, L. T. Yu, J. Pepichon, R. Buvet, Electrochemical chains using protolytic organic semiconductors, Electrochimica Acta, 13 (1968) 1451-1458.

[11] A. F. Diaz, J. A. Logan, Electroactive polyaniline films, Journal of Electroanalytical Chemistry and Interfacial Electrochemistry, 111 (1980) 111-114.

[12] H. Shirakawa, E. J. Louis, A. G. MacDiarmid, C. K. Chiang, A. J. Heeger, Synthesis of electrically conducting organic polymers: halogen derivatives of polyacetylene, (CH), Journal of the Chemical Society, Chemical Communications,16 (1977) 578-580.

[13] K.-J. Baeg, M. Caironi, Y.-Y. Noh, Toward Printed Integrated Circuits based on Unipolar or Ambipolar Polymer Semiconductors, Advanced Materials, 25 (2013) 4210-4244.

[14] Y.-J. Cheng, S.-H. Yang, C.-S. Hsu, Synthesis of Conjugated Polymers for Organic Solar Cell Applications, Chemical Reviews, 109 (2009) 5868-5923.

[15] F. Cicoira, C. Santato, Organic Light Emitting Field Effect Transistors: Advances and Perspectives, Advanced Functional Materials, 17 (2007) 3421-3434.

[16] V. Coropceanu, J. Cornil, D. A. da Silva Filho, Y. Olivier, R. Silbey, J.-L. Brédas, Charge Transport in Organic Semiconductors, Chemical Reviews, 107 (2007) 926-952.

[17] A. Facchetti, π-Conjugated Polymers for Organic Electronics and Photovoltaic Cell Applications, Chemistry of Materials, 23 (2010) 733-758.

[18] S. Günes, H. Neugebauer, N. S. Sariciftci, Conjugated Polymer-Based Organic Solar Cells, Chemical Reviews, 107 (2007) 1324-1338.

[19] H. Sirringhaus, N. Tessler, R. H. Friend, Integrated Optoelectronic Devices Based on Conjugated Polymers, Science, 280 (1998) 1741-1744.

[20] C. Wang, H. Dong, W. Hu, Y. Liu, D. Zhu, Semiconducting π-Conjugated Systems in Field-Effect Transistors: A Material Odyssey of Organic Electronics, Chemical Reviews, 112 (2011) 2208-2267.

[21] J. Zaumseil, H. Sirringhaus, Electron and Ambipolar Transport in Organic Field-Effect Transistors, Chemical Reviews, 107 (2007) 1296-1323.

[22] S. Sadki, P. Schottland, N. Brodie, G. Sabouraud, The mechanisms of pyrrole electropolymerization, Chemical Society Reviews, 29 (2000) 283-293.

[23] T. H. Chao, J. March, A study of polypyrrole synthesized with oxidative transition metal ions, Journal of Polymer Science Part A: Polymer Chemistry, 26 (1988) 743-753.

[24] S. Machida, S. Miyata, A. Techagumpuch, Chemical synthesis of highly electrically conductive polypyrrole, Synthetic Metals, 31 (1989) 311-318.

[25] N. Puanglek, A. Sittattrakul, W. Lerdwijitjarud, Enhancement of Electrical Conductivity of Polypyrrole and Its Derivative, Sci. J. UBU, 1 (2010) 35-42.

[26] G. Qi, L. Huang, H. Wang, Highly conductive free standing polypyrrole films prepared by freezing interfacial polymerization, Chemical Communications, 48 (2012) 8246-8248.

[27] T. V. Vernitskaya, O.N. Efimov, Polypyrrole: a conducting polymer; its synthesis, properties and applications, Russian Chemical Reviews, 66 (1997) 443-457.

[28] L.-X. Wang, X.-G. Li, Y.-L. Yang, Preparation, properties and applications of polypyrroles, Reactive and Functional Polymers, 47 (2001) 125-139.

[29] N. Blouin, A. Michaud, M. Leclerc, A Low-Bandgap Poly(2,7-Carbazole) Derivative for Use in High-Performance Solar Cells, Advanced Materials, 19 (2007) 2295-2300.

[30] Sung Heum Park, Anshuman Roy, Serge Beaupré, Shinuk Cho, Nelson Coates, Ji Sun Moon, Daniel Moses, Mario Leclerc, Kwanghee Lee, A. J. Heeger, Bulk Heterojunction Solar Cells with Internal Quantum Efficiency Approaching 100%, Nature Photonics, 3 (2009) 297-302.

[31] S. Cho, J. H. Seo, G. -H. Kim, J. Y. Kim, H. Y. Woo, Observation of ambipolar field-effect behavior in donor-acceptor conjugated copolymers, Journal of Materials Chemistry, 22 (2012) 21238-21241.

[32] S. Cho, J. H. Seo, S. H. Park, S. Beaupré, M. Leclerc, A. J. Heeger, A Thermally Stable Semiconducting Polymer, Advanced Materials, 22 (2010) 1253-1257.

[33] J. L. Brédas, J. C. Scott, K. Yakushi, G. B. Street, Polarons and bipolarons in polypyrrole: Evolution of the band structure and optical spectrum upon doing, Physical Review B, 30 (1984) 1023-1025.

[34] J. L. Bredas, G. B. Street, Polarons, bipolarons, and solitons in conducting polymers, Accounts of Chemical Research, 18 (1985) 309-315.

[35] S. Roth, H. Bleier, W. Pukacki, Charge transport in conducting polymers, Faraday Discussions of the Chemical Society, 88 (1989) 223-233.

[36] A. Miller, E. Abrahams, Impurity Conduction at Low Concentrations, Physical Review, 120 (1960) 745-755.

[37] Giuseppe Casalbore-Miceli, Mujie Yang, Yang Li, Nadia Camaioni, Alessandro Martelli, A. Zanelli, Effect of the doping level on the conductance of polymer–salts complexes in the presence of humidity, Sensors and Actuators B: Chemical, 97 (2004) 362-368.

[38] Avanish Pratap Singh, Anoop Kumar S., Amita Chandra, S. K. Dhawan, Conduction mechanism in Polyaniline-flyash composite material for shielding against electromagnetic radiation in X-band & Ku band, AIP Advances, 1 (2011) 022147.

[39] S. Banerjee, A.K. Tyagi, Functional Materials: Preparation, Processing and Applications, Elsevier (2012).

[40] J. Heinze, Electrochemistry of conducting polymers, Synthetic Metals, 43 (1991) 2805-2823.

[41] J. Heinze, B. A. Frontana-Uribe, S. Ludwigs, Electrochemistry of Conducting Polymers—Persistent Models and New Concepts, Chemical Reviews, 110 (2010) 4724-4771.

[42] S. Choudhury, V. Saxena, S. K. Gupta, J. V. Yakhmi, A study on Langmuir–Blodgett films of conducting polycarbazole, Thin Solid Films, 493 (2005) 267-272.

[43] V. Saxena, S. Choudhury, P. Jha, S. P. Koiry, A. K. Debnath, D. K. Aswal, S. K. Gupta, J. V. Yakhmi, In situ spectroscopic studies to investigate uncharacteristic NH3 sensing behavior of polycarbazole Langmuir–Blodgett films, Sensors and Actuators B: Chemical, 150 (2010) 7-11.

[44] B. J. de Gans, P. C. Duineveld, U. S. Schubert, Inkjet Printing of Polymers: State of the Art and Future Developments, Advanced Materials, 16 (2004) 203-213.

[45] U. Sree, Y. Yamamoto, B. Deore, H. Shiigi, T. Nagaoka, Characterisation of polypyrrole nano-films for membrane-based sensors, Synthetic Metals, 131 (2002) 161-165.

[46] M. Gruber, E. Zojer, F. Schürrer, K. Zojer, Impact of Materials versus Geometric Parameters on the Contact Resistance in Organic Thin-Film Transistors, Advanced Functional Materials, 23 (2013) 2941-2952.

[47] H. Klauk, Organic thin-film transistors, Chemical Society Reviews, 39 (2010) 2643-2666.

[48] F. Ebisawa, T. Kurokawa, S. Nara, Electrical properties of polyacetylene/polysiloxane interface, Journal of Applied Physics, 54 (1983) 3255-3259.

[49] A. Tsumura, H. Koezuka, T. Ando, Macromolecular electronic device: Field-effect transistor with a polythiophene thin film, Applied Physics Letters, 49 (1986) 1210-1212.

[50] A. Assadi, C. Svensson, M. Willander, O. Inganas, Field-effect mobility of poly(3-hexylthiophene), Applied Physics Letters, 53 (1988) 195-197.

[51] H. Koezuka, A. Tsumura, H. Fuchigami, K. Kuramoto, Polythiophene field-effect transistor with polypyrrole worked as source and drain electrodes, Applied Physics Letters, 62 (1993) 1794-1796.

[52] Z. Bao, A. Dodabalapur, A. J. Lovinger, Soluble and processable regioregular poly(3-hexylthiophene) for thin film field-effect transistor applications with high mobility, Applied Physics Letters, 69 (1996) 4108-4110.

[53] S. Cho, K. Lee, J. Yuen, G. Wang, D. Moses, A. J. Heeger, M. Surin, R. Lazzaroni, Thermal annealing-induced enhancement of the field-effect mobility of regioregular poly(3-hexylthiophene) films, Journal of Applied Physics, 100 (2006) 114503-114506.

[54] B. S. Ong, Y. Wu, P. Liu, S. Gardner, High-Performance Semiconducting Polythiophenes for Organic Thin-Film Transistors, Journal of the American Chemical Society, 126 (2004) 3378-3379.

[55] I. McCulloch , M. Heeney , C. Bailey , K. Genevicius, M. I. M. Shkunov , D. Sparrowe , S. Tierney, R. Wagner, W. M. Zhang, M. L. Chabinyc, R. J. Kline, M. D. Mcgehee , M.F. Toney, Liquid-crystalline semiconducting polymers with high charge-carrier mobility, Nature Materials, 5 (2006) 328-333.

[56] B. H. Hamadani, D. J. Gundlach, I. McCulloch, M. Heeney, Undoped polythiophene field-effect transistors with mobility of $1cm^2V^{-1}s^{-1}$, Applied Physics Letters, 91 (2007) 243512.

[57] H. N. Tsao, D. M. Cho, I. Park, M. R. Hansen, A. Mavrinskiy, D. Y. Yoon, R. Graf, W. Pisula, H. W. Spiess, K. Müllen, Ultrahigh Mobility in Polymer Field-Effect Transistors by Design, Journal of the American Chemical Society, 133 (2011) 2605-2612.

[58] H.-R. Tseng, L. Ying, B. B. Y. Hsu, L. A. Perez, C. J. Takacs, G. C. Bazan, A. J. Heeger, High Mobility Field Effect Transistors Based on Macroscopically Oriented Regioregular Copolymers, Nano Letters, 12 (2012) 6353-6357.

[59] H. Chen, Y. Guo, G. Yu, Y. Zhao, J. Zhang, D. Gao, H. Liu, Y. Liu, Highly π-Extended Copolymers with Diketopyrrolopyrrole Moieties for High-Performance Field-Effect Transistors, Advanced Materials, 24 (2012) 4618-4622.

[60] Jun Li, Yan Zhao, Huei Shuan Tan, Yunlong Guo, Chong-An Di, Gui Yu, Yunqi Liu, Ming Lin, Suo Hon Lim, Yuhua Zhou, Haibin Su, B.S. Ong, A stable solution-processed polymer semiconductor with record high-mobility for printed transistors, Scientific Reports, 2 (2012) 754.

[61] P. Sonar, T. R. B. Foong, S. P. Singh, Y. Li, A. Dodabalapur, A furan-containing conjugated polymer for high mobility ambipolar organic thin film transistors, Chemical Communications, 48 (2012) 8383-8385.

[62] J. Lee, A. R. Han, J. Kim, Y. Kim, J. H. Oh, C. Yang, Solution-Processable Ambipolar Diketopyrrolopyrrole–Selenophene Polymer with Unprecedentedly High Hole and Electron Mobilities, Journal of the American Chemical Society, 134 (2012) 20713-20721.

[63] M .L. Chabinyc, F. Endicott, B. D. Vogt, D. M. DeLongchamp, E. K. Lin, Y. Wu, P. Liu, B. S. Ong, Effects of humidity on unencapsulated poly(thiophene) thin-film transistors, Applied Physics Letters, 88 (2006) 113514-113513.

[64] D. K. Aswal and S. K. Gupta, Science and Technology of Chemiresistor Gas Sensors, Nova Science Publisher, New York (2007).

[65] D.K. Aswal and J.V. Yakhmi, Molecular and organic devices, Nova Science Publisher, USA (2010).

[66] N. V. Bhat, A. P. Gadre, V. A. Bambole, Investigation of electropolymerized polypyrrole composite film: Characterization and application to gas sensors, Journal of Applied Polymer Science, 88 (2003) 22-29.

[67] S. V. Mello, P. Dynarowicz-Łątka, A. Dhanabalan, R. F. Bianchi, R. Onmori, R. A. J. Janssen, O.N. Oliveira Jr, Langmuir and Langmuir–Blodgett films from the N-hexyl-pyrrole-

thiophene (AB) semi-amphiphilic copolymer, Colloids and Surfaces A: Physicochemical and Engineering Aspects, 198–200 (2002) 45-51.

[68] C. Nguyen Van, K. Potje-Kamloth, Electrical and NOx gas sensing properties of metallophthalocyanine-doped polypyrrole/silicon heterojunctions, Thin Solid Films, 392 (2001) 113-121.

[69] V. C. Nguyen, K. Potje-Kamloth, Electrical and chemical sensing properties of doped polypyrrole/gold Schottky barrier diodes, Thin Solid Films, 338 (1999) 142-148.

[70] D. Xie, Y. Jiang, W. Pan, D. Li, Z. Wu, Y. Li, Fabrication and characterization of polyaniline-based gas sensor by ultra-thin film technology, Sensors and Actuators B: Chemical, 81 (2002) 158-164.

[71] E. Bekyarova, M. Davis, T. Burch, M. E. Itkis, B. Zhao, S. Sunshine, R. C. Haddon, Chemically Functionalized Single-Walled Carbon Nanotubes as Ammonia Sensors, The Journal of Physical Chemistry B, 108 (2004) 19717-19720.

[72] Benjamin P. J. de Lacy Costello, Norman M Ratcliffe, Pennadam S. Sivanand, The synthesis of novel 3-substituted pyrrole monomers possessing chiral side groups: a study of their chemical polymerisation and the assessment of their chiral discrimination properties, Synthetic Metals, 139 (2003) 43-55.

[73] Z. Deng, D. C. Stone, Characterization of Polymer Films of Pyrrole Derivatives for Chemical Sensing by Cyclic Voltammetry, X-ray Photoelectron Spectroscopy and Vapour Sorption Studies, Analyst, 122 (1997) 1129-1138.

[74] N. Guernion, B. P. J. de Lacy Costello, N. M. Ratcliffe, The synthesis of 3-octadecyl- and 3-docosylpyrrole, their polymerisation and incorporation into novel composite gas sensitive resistors, Synthetic Metals, 128 (2002) 139-147.

[75] M. Krondak, G. Broncová, S. Anikin, A. Merz, V. Mirsky, Chemosensitive properties of poly-4,4′-dialkoxy-2,2′-bipyrroles, J Solid State Electrochem, 10 (2006) 185-191.

[76] B. Vercelli, S. Zecchin, N. Comisso, G. Zotti, A. Berlin, E. Dalcanale, L.B. Groenendaal, Solvoconductivity of Polyconjugated Polymers: The Roles of Polymer Oxidation Degree and Solvent Electrical Permittivity, Chemistry of Materials, 14 (2002) 4768-4774.

[77] B. Li, G. Sauvé, M. C. Iovu, M. Jeffries-El, R. Zhang, J. Cooper, S. Santhanam, L. Schultz, J. C. Revelli, A.G. Kusne, T. Kowalewski, J. L. Snyder, L. E. Weiss, G. K. Fedder, R.D. McCullough, D. N. Lambeth, Volatile Organic Compound Detection Using Nanostructured Copolymers, Nano Letters, 6 (2006) 1598-1602.

[78] L. Torsi, M.C. Tanese, N. Cioffi, M. C. Gallazzi, L. Sabbatini, P.G. Zambonin, G. Raos, S.V. Meille, M.M. Giangregorio, Side-Chain Role in Chemically Sensing Conducting Polymer Field-Effect Transistors, The Journal of Physical Chemistry B, 107 (2003) 7589-7594.

[79] V. V. Chabukswar, S. Pethkar, A.A. Athawale, Acrylic acid doped polyaniline as an ammonia sensor, Sensors and Actuators B: Chemical, 77 (2001) 657-663.

[80] J. E. G. de Souza, F.L. dos Santos, B. Barros-Neto, C.G. dos Santos, C. P. de Melo, Polypyrrole thin films gas sensors, Synthetic Metals, 119 (2001) 383-384.

[81] K. H. An, S. Y. Jeong, H. R. Hwang, Y. H. Lee, Enhanced Sensitivity of a Gas Sensor Incorporating Single-Walled Carbon Nanotube–Polypyrrole Nanocomposites, Advanced Materials, 16 (2004) 1005-1009.

[82] N. Bhat, P. Geetha, S. Pawde, Preparation and characterization of composites of polypyrrole, Polymer Engineering & Science, 39 (1999) 1517-1524.

[83] S. Bouchtalla, L. Auret, J. M. Janot, A. Deronzier, J. C. Moutet, P. Seta, [60]Fullerene immobilized in a thin functionalized polypyrrole film. Basic principles for the elaboration of an oxygen sensor, Materials Science and Engineering: C, 21 (2002) 125-129.

[84] H. Fukuda, M. Ise, T. Kogure, N. Takano, Gas sensors based on poly-3-hexylthiophene thin-film transistors, Thin Solid Films, 464–465 (2004) 441-444.

[85] L. Geng, X. Huang, Y. Zhao, P. Li, S. Wang, S. Zhang, S. Wu, H2S sensitivity study of polypyrrole/WO3 materials, Solid-State Electronics, 50 (2006) 723-726.

[86] S. H. Hosseini, A. A. Entezami, Conducting polymer blends of polypyrrole with polyvinyl acetate, polystyrene, and polyvinyl chloride based toxic gas sensors, Journal of Applied Polymer Science, 90 (2003) 49-62.

[87] A. Joshi, D. K. Aswal, S.K. Gupta, J. V. Yakhmi, S. A. Gangal, ZnO-nanowires modified polypyrrole films as highly selective and sensitive chlorine sensors, Applied Physics Letters, 94 (2009) 103115.

[88] V. Saxena, D.K. Aswal, M. Kaur, S.P. Koiry, S.K. Gupta, J.V. Yakhmi, R.J. Kshirsagar, S.K. Deshpande, Enhanced NO2 selectivity of hybrid poly(3-hexylthiophene): ZnO-nanowire thin films, Applied Physics Letters, 90 (2007) -.

[89] K. Suri, S. Annapoorni, A.K. Sarkar, R.P. Tandon, Gas and humidity sensors based on iron oxide–polypyrrole nanocomposites, Sensors and Actuators B: Chemical, 81 (2002) 277-282.

[90] L. Torsi, M. Pezzuto, P. Siciliano, R. Rella, L. Sabbatini, L. Valli, P.G. Zambonin, Conducting polymers doped with metallic inclusions: New materials for gas sensors, Sensors and Actuators B: Chemical, 48 (1998) 362-367.

[91] Jiri Janata, Mira Josowicz, Conducting polymers in electronic chemical sensors, Nature materials, 2 (2003) 19-24.

[92] J. Mabeck, G. Malliaras, Chemical and biological sensors based on organic thin-film transistors, Anal Bioanal Chem, 384 (2006) 343-353.

[93] P.S. Barker, A.P. Monkman, M.C. Petty, R. Pride, A polyaniline/sllicon hybrid field effect transistor humidity sensor, Synthetic Metals, 85 (1997) 1365-1366.

[94] J.A. Covington, J.W. Gardner, D. Briand, N.F. de Rooij, A polymer gate FET sensor array for detecting organic vapours, Sensors and Actuators B: Chemical, 77 (2001) 155-162.

[95] K. Domanský, D.L. Baldwin, J.W. Grate, T.B. Hall, J. Li, M. Josowicz, J. Janata, Development and Calibration of Field-Effect Transistor-Based Sensor Array for Measurement of Hydrogen and Ammonia Gas Mixtures in Humid Air, Analytical Chemistry, 70 (1998) 473-481.

[96] M.G.H. Meijerink, M. Koudelka-Hep, N.F. de Rooij, D.J. Strike, J. Hendrikse, W. Olthuis, P. Bergveld, Gas-Dependent Field Effect Transistor with an Electrodeposited Conducting Polymer Gate Contact, Electrochemical and Solid-State Letters, 2 (1999) 138-139.

[97] A. Assadi, G. Gustafsson, M. Willander, C. Svensson, O. Inganäs, Determination of field-effect mobility of poly(3-hexylthiophene) upon exposure to NH3 gas, Synthetic Metals, 37 (1990) 123-130.

[98] Y. Ohmori , H. Takahashi , K. Muro , M. Uchida, T. Kawai , K. Yoshino, Gas-Sensitive Schottky Gated Field Effect Transistors Utilizing Poly(3-alkylthiophene) Films, Japanese Journal of Applied Physics, 30 (1991) L1247-L1249.

[99] B. Crone, A. Dodabalapur, A. Gelperin, L. Torsi, H.E. Katz, A.J. Lovinger, Z. Bao, Electronic sensing of vapors with organic transistors, Applied Physics Letters, 78 (2001) 2229-2231.

[100] L. Torsi, A. Tafuri, N. Cioffi, M.C. Gallazzi, A. Sassella, L. Sabbatini, P.G. Zambonin, Regioregular polythiophene field-effect transistors employed as chemical sensors, Sensors and Actuators B: Chemical, 93 (2003) 257-262.

[101] M.C. Tanese, L. Torsi, N. Cioffi, L.A. Zotti, D. Colangiuli, G.M. Farinola, F. Babudri, F. Naso, M.M. Giangregorio, L. Sabbatini, P.G. Zambonin, Poly(phenyleneethynylene) polymers

bearing glucose substituents as promising active layers in enantioselective chemiresistors, Sensors and Actuators B: Chemical, 100 (2004) 17-21.

[102] H.S. Kang, J.K. Lee, J.W. Lee, J. Joo, J.M. Ko, M.S. Kim, J.Y. Lee, Humidity-dependent characteristics of thin film poly(3,4-ethylenedioxythiophene) field-effect transistor, Synthetic Metals, 155 (2005) 176-179.

[103] J.W. Jeong, Y.D. Lee, Y.M. Kim, Y.W. Park, J.H. Choi, T.H. Park, C.D. Soo, S.M. Won, I.K. Han, B.K. Ju, The response characteristics of a gas sensor based on poly-3-hexylithiophene thin-film transistors, Sensors and Actuators B: Chemical, 146 (2010) 40-45.

[104] S. Tiwari, A.K. Singh, L. Joshi, P. Chakrabarti, W. Takashima, K. Kaneto, R. Prakash, Poly-3-hexylthiophene based organic field-effect transistor: Detection of low concentration of ammonia, Sensors and Actuators B: Chemical, 171–172 (2012) 962-968.

[105] C.C. Bof Bufon, T. Heinzel, Polypyrrole thin-film field-effect transistor, Applied Physics Letters, 89 (2006) 012104

[106] S.P. Koiry, D.K. Aswal, A.K. Chauhan, V. Saxena, S.K. Nayak, S.K. Gupta, J.V. Yakhmi, Electrical bistability in electrografted 5-(4-undecenyloxyphenyl)-10,15,20-triphenylporphyrin monolayer on Si, Chemical Physics Letters, 453 (2008) 68-72.

[107] A. Singh, A. Kumar, A. Kumar, S. Samanta, A.K. Debnath, P. Jha, R. Prasad, Z. Salmi, S. Nowak, M.M. Chehimi, D.K. Aswal, S.K. Gupta, Flexible cobalt-phthalocyanine thin films with high charge carrier mobility, Applied Physics Letters, 101 (2012) 222102.

[108] W. Kemp, organic spectroscopy, Palgrave Macmillan Limited (1991).

[109] Skoog, Holler, Nieman, Principles of instrumental analysis, Brooks Cole (1998).

[110] D. Briggs, M.P. Seah, Practical Surface Analysis by Auger and X-ray Photoelectron Spectroscopy, Wiley (1983).

[111] J. F. Moulder, W.F. Stickle, P.E. Sobol , K.D. Bomben, Handbook of X-ray Photoelectron Spectroscopy, Physical electronics, USA (1995).

[112] John F. Watts, J. Wolstenholme, An Introduction to Surface Analysis by XPS and AES, John Wiley and Sons (2003).

[113] D.K. Aswal, K.P. Muthe, S. Tawde, S. Chodhury, N. Bagkar, A. Singh, S.K. Gupta, J.V. Yakhmi, XPS and AFM investigations of annealing induced surface modifications of MgO single crystals, Journal of Crystal Growth, 236 (2002) 661-666.

[114] Instruction Manual, SPM Solver P47, NT-MDT Co., Zelenograd Research Institute of Physical Problems, Moscow, Russia.

[115] Instruction Manual, Multiview 4000SPM/AFM, Nanonics Imaging Pvt. Ltd, Israel.

[116] I. Horcas, R. Fernández, J.M. Gómez-Rodríguez, J. Colchero, J. Gómez-Herrero, A.M. Baro, WSXM: A software for scanning probe microscopy and a tool for nanotechnology, Review of Scientific Instruments, 78 (2007) -.

[117] P. J. Goodhew, F.J. Humphreys, Electron Microscopy and Analysis, Taylor and Francis (1988).

[118] I.M. Watt, The Principles and practice of electron microscopy, Cambridge University Press (1985).

[119] Y. Berdichevsky, Y.H. Lo, Polypyrrole Nanowire Actuators, Advanced Materials, 18 (2006) 122-125.

[120] W. Cheng, M.J. Campolongo, S.J. Tan, D. Luo, Freestanding ultrathin nano-membranes via self-assembly, Nano Today, 4 (2009) 482-493.

[121] K. Ramanathan, M.A. Bangar, M. Yun, W. Chen, N.V. Myung, A. Mulchandani, Bioaffinity Sensing Using Biologically Functionalized Conducting-Polymer Nanowire, Journal of the American Chemical Society, 127 (2004) 496-497.

[122] Y. Uozumi, Y.M.A. Yamada, T. Beppu, N. Fukuyama, M. Ueno, T. Kitamori, Instantaneous Carbon−Carbon Bond Formation Using a Microchannel Reactor with a Catalytic Membrane, Journal of the American Chemical Society, 128 (2006) 15994-15995.

[123] H.-H. Yang, S.-Q. Zhang, F. Tan, Z.-X. Zhuang, X.-R. Wang, Surface Molecularly Imprinted Nanowires for Biorecognition, Journal of the American Chemical Society, 127 (2005) 1378-1379.

[124] L.-h. Zhang, R.A. Hendel, P.G. Cozzi, S.L. Regen, A Single Langmuir−Blodgett Monolayer for Gas Separations, Journal of the American Chemical Society, 121 (1999) 1621-1622.

[125] A. Ramanaviciene, A. Ramanavicius, Application of Polypyrrole for the Creation of Immunosensors, Critical Reviews in Analytical Chemistry, 32 (2002) 245-252.

[126] D. Sutar, D. K. Aswal, S. K. Gupta, J. V. Yakhmi, Electrochemical actuator from conductive electroactive polymer polypyrrole deposited on gold, Indian Journal of Pure & Applied Physics, 45 (2007) 354-357.

[127] T.F. Otero, M.J. Ariza, Revisiting the Electrochemical and Polymeric Behavior of a Polypyrrole Free-Standing Electrode in Aqueous Solution, The Journal of Physical Chemistry B, 107 (2003) 13954-13961.

[128] G. Shi, S. Jin, G. Xue, C. Li, A Conducting Polymer Film Stronger Than Aluminum, Science, 267 (1995) 994-996.

[129] Y. Lu, G. Shi, C. Li, Y. Liang, Thin polypyrrole films prepared by chemical oxidative polymerization, Journal of Applied Polymer Science, 70 (1998) 2169-2172.

[130] D. Wang, Y.-X. Li, Z. Shi, H.-L. Qin, L. Wang, X.-F. Pei, J. Jin, Spontaneous Growth of Free-Standing Polypyrrole Films at an Air/Ionic Liquid Interface, Langmuir, 26 (2010) 14405-14408.

[131] M. Shirakawa, N. Fujita, S. Shinkai, A Stable Single Piece of Unimolecularly π-Stacked Porphyrin Aggregate in a Thixotropic Low Molecular Weight Gel: A One-Dimensional Molecular Template for Polydiacetylene Wiring up to Several Tens of Micrometers in Length, Journal of the American Chemical Society, 127 (2005) 4164-4165.

[132] S. Okada, H. Segawa, Substituent-Control Exciton in J-Aggregates of Protonated Water-Insoluble Porphyrins, Journal of the American Chemical Society, 125 (2003) 2792-2796.

[133] H.-L. Ma, W.-J. Jin, Studies on the effects of metal ions and counter anions on the aggregate behaviors of meso-tetrakis(p-sulfonatophenyl)porphyrin by absorption and fluorescence spectroscopy, Spectrochimica Acta Part A: Molecular and Biomolecular Spectroscopy, 71 (2008) 153-160.

[134] G. Cho, B.M. Fung, D.T. Glatzhofer, J.-S. Lee, Y.-G. Shul, Preparation and Characterization of Polypyrrole-Coated Nanosized Novel Ceramics, Langmuir, 17 (2001) 456-461.

[135] R.G. Davidson, T.G. Turner, An IR spectroscopic study of the electrochemical reduction of polypyrrole doped with dodecylsulfate anion, Synthetic Metals, 72 (1995) 121-128.

[136] K.S. Jang, H. Lee, B. Moon, Synthesis and characterization of water soluble polypyrrole doped with functional dopants, Synthetic Metals, 143 (2004) 289-294.

[137] V.P. Menon, J. Lei, C.R. Martin, Investigation of Molecular and Supermolecular Structure in Template-Synthesized Polypyrrole Tubules and Fibrils, Chemistry of Materials, 8 (1996) 2382-2390.

[138] D.Y. Kim, J.Y. Lee, D.K. Moon, C.Y. Kim, Stability of reduced polypyrrole, Synthetic Metals, 69 (1995) 471-474.

[139] T.A. Skotheim, R.L. Elsenbaumer, J.R. Reynolds, Handbook of Conducting Polymers, Marcel Dekker Inc., New York1998.

[140] C.C. Bof Bufon, T. Heinzel, Transport properties of chemically synthesized polypyrrole thin films, Physical Review B, 76 (2007) 245206.

[141] N.F. Mott, Metale-insulator Transition, Taylor-Francis, London1990.

[142] M. Ghosh, A. Barman, A. Das, A.K. Meikap, S.K. De, S. Chatterjee, Electrical transport in paratoluene sulfonate doped polypyrrole films at low temperature, Journal of Applied Physics, 83 (1998) 4230-4235.

[143] N.T. Kemp, A.B. Kaiser, H.J. Trodahl, B. Chapman, R.G. Buckley, A.C. Partridge, P.J.S. Foot, Effect of ammonia on the temperature-dependent conductivity and thermopower of polypyrrole, Journal of Polymer Science Part B: Polymer Physics, 44 (2006) 1331-1338.

[144] Q. Ameer, S.B. Adeloju, Polypyrrole-based electronic noses for environmental and industrial analysis, Sensors and Actuators B: Chemical, 106 (2005) 541-552.

[145] A. Garsuch, R.R. Sattler, P.G. Pickup, Formation of polypyrrole from 2,5-bis(2-pyrrolyl)pyrrolidine, Chemical Communications, (2004) 344-345.

[146] G.B. Street, T.C. Clarke, M. Krounbi, K. Kanazawa, V. Lee, P. Pfluger, J.C. Scott, G. Weiser, Preparation and characterization of neutral and oxidized polypyrrole films, Molecular Crystals and Liquid Crystals, 83 (1982) 253-264.

[147] J.C. Scott, L.D. Bozano, Nonvolatile Memory Elements Based on Organic Materials, Advanced Materials, 19 (2007) 1452-1463.

[148] N.J. Tao, Electron transport in molecular junctions, nature nanotechnology, 1 (2006) 173-181.

[149] M. Cölle, M. Büchel, D.M. de Leeuw, Switching and filamentary conduction in non-volatile organic memories, Organic Electronics, 7 (2006) 305-312.

[150] J.F. Rubinson, Y.P. Kayinamura, Charge transport in conducting polymers: insights from impedance spectroscopy, Chemical Society Reviews, 38 (2009) 3339-3347.

[151] N.-H. Ge, C.M. Wong, R.L. Lingle, J.D. McNeill, K.J. Gaffney, C.B. Harris, Femtosecond Dynamics of Electron Localization at Interfaces, Science, 279 (1998) 202-205.

[152] S. Serra, S. Iarlori, E. Tosatti, S. Scandolo, M.C. Righi, G.E. Santoro, Self-trapping vs. non-trapping of electrons and holes in organic insulators: polyethylene, Chemical Physics Letters, 360 (2002) 487-493.

[153] X. Lu, W. Zhang, C. Wang, T.-C. Wen, Y. Wei, One-dimensional conducting polymer nanocomposites: Synthesis, properties and applications, Progress in Polymer Science, 36 (2011) 671-712.

[154] M. Mumtaz, E. Cloutet, C. Labrugere, G. Hadziioannou, H. Cramail, Synthesis of hybrid semiconducting polymer-metal latexes, Polymer Chemistry, 4 (2013) 615-622.

[155] O. M. Folarin, E. R. Sadiku, A. Maity, Polymer-noble metal nanocomposites: Review, International Journal of the Physical Sciences, 6 (2011) 4869-4882.

[156] Y. Fu, A. Manthiram, Core-shell structured sulfur-polypyrrole composite cathodes for lithium-sulfur batteries, RSC Advances, 2 (2012) 5927-5929.

[157] M. Lahav, E.A. Weiss, Q. Xu, G.M. Whitesides, Core−Shell and Segmented Polymer−Metal Composite Nanostructures, Nano Letters, 6 (2006) 2166-2171.

[158] G.V. Ramesh, S. Porel, T.P. Radhakrishnan, Polymer thin films embedded with in situ grown metal nanoparticles, Chemical Society Reviews, 38 (2009) 2646-2656.

[159] A. Ramanavičius, A. Ramanavičienė, A. Malinauskas, Electrochemical sensors based on conducting polymer—polypyrrole, Electrochimica Acta, 51 (2006) 6025-6037.

[160] K. Bouzek, K.M. Mangold, K. Jüttner, Platinum distribution and electrocatalytic properties of modified polypyrrole films, Electrochimica Acta, 46 (2001) 661-670.

[161] M.A. Breimer, G. Yevgeny, S. Sy, O.A. Sadik, Incorporation of Metal Nanoparticles in Photopolymerized Organic Conducting Polymers: A Mechanistic Insight, Nano Letters, 1 (2001) 305-308.

[162] Y. Liu, Z. Liu, N. Lu, E. Preiss, S. Poyraz, M.J. Kim, X. Zhang, Facile synthesis of polypyrrole coated copper nanowires: a new concept to engineered core-shell structures, Chemical Communications, 48 (2012) 2621-2623.

[163] J. Xu, J. Hu, B. Quan, Z. Wei, Decorating Polypyrrole Nanotubes with Au Nanoparticles by an In Situ Reduction Process, Macromolecular Rapid Communications, 30 (2009) 936-940.

[164] K. Xue, Y. Xu, W. Song, One-step synthesis of 3D dendritic gold@polypyrrole nanocomposites via a simple self-assembly method and their electrocatalysis for H2O2, Electrochimica Acta, 60 (2012) 71-77.

[165] J. Wei, G. Xing, L. Gao, H. Suo, X. He, C. Zhao, S. Li, S. Xing, Nickel foam based polypyrrole-Ag composite film: a new route toward stable electrodes for supercapacitors, New Journal of Chemistry, 37 (2013) 337-341.

[166] X. Yang, L. Li, F. Yan, Polypyrrole/silver composite nanotubes for gas sensors, Sensors and Actuators B: Chemical, 145 (2010) 495-500.

[167] V.S. Ijeri, J.R. Nair, C. Gerbaldi, R.S. Gonnelli, S. Bodoardo, R.M. Bongiovanni, An elegant and facile single-step UV-curing approach to surface nano-silvering of polymer composites, Soft Matter, 6 (2010) 4666-4668.

[168] C.R. Martins, Y.M. Almeida, G.C. Nascimento, W.M. Azevedo, Metal nanoparticles incorporation during the photopolymerization of polypyrrole, J Mater Sci, 41 (2006) 7413-7418.

[169] M.M. Ayad, E. Zaki, Synthesis and characterization of silver–polypyrrole film composite, Applied Surface Science, 256 (2009) 787-791.

[170] S. Fujii, A. Aichi, K. Akamatsu, H. Nawafune, Y. Nakamura, One-step synthesis of polypyrrole-coated silver nanocomposite particles and their application as a coloured particulate emulsifier, Journal of Materials Chemistry, 17 (2007) 3777-3779.

[171] S. Jing, S. Xing, L. Yu, C. Zhao, Synthesis and characterization of Ag/polypyrrole nanocomposites based on silver nanoparticles colloid, Materials Letters, 61 (2007) 4528-4530.

[172] E. Pintér, R. Patakfalvi, T. Fülei, Z. Gingl, I. Dékány, C. Visy, Characterization of Polypyrrole−Silver Nanocomposites Prepared in the Presence of Different Dopants, The Journal of Physical Chemistry B, 109 (2005) 17474-17478.

[173] Y. Wei, L. Li, X. Yang, G. Pan, G.Y. and, X. Yu, One-Step UV-Induced Synthesis of Polypyrrole/Ag Nanocomposites at the Water/Ionic Liquid Interface, Nanoscale Research Letters, 5 (2010) 433–437.

[174] M.K. Lei, Y. Liu, Y.P. Li, Controllable wettability of poly(ethylene terephthlate) film modified by oxygen combined inductively and capacitively coupled radio-frequency plasma, Applied Surface Science, 257 (2011) 7350-7358.

[175] D.O.H. Teare, C. Ton-That, R.H. Bradley, Surface characterization and ageing of ultraviolet–ozone-treated polymers using atomic force microscopy and x-ray photoelectron spectroscopy, Surface and Interface Analysis, 29 (2000) 276-283.

[176] A. Vesel, M. Mozetic, A. Zalar, XPS study of oxygen plasma activated PET, Vacuum, 82 (2007) 248-251.

[177] K.R. Kirov, H.E. Assender, Quantitative ATR-IR Analysis of Anisotropic Polymer Films: Surface Structure of Commercial PET, Macromolecules, 38 (2005) 9258-9265.

[178] R.A. Simon, A.J. Ricco, M.S. Wrighton, Synthesis and characterization of a new surface derivatizing reagent to promote the adhesion of polypyrrole films to N-type silicon photoanodes: N-(3-(trimethoxysilyl)propyl)pyrrole, Journal of the American Chemical Society, 104 (1982) 2031-2034.

[179] D. Cossement, F. Plumier, J. Delhalle, L. Hevesi, Z. Mekhalif, Electrochemical deposition of polypyrrole films on organosilane-modified ITO substrates, Synthetic Metals, 138 (2003) 529-536.

[180] High Resolution XPS of Organic Polymers,The Scienta ESCA300 Database,, in: G. Beamson, D. Briggs (Eds.), John Wiley & Sons, U. K.1992, pp. 174.

[181] High Resolution XPS of Organic Polymers, The Scienta ESCA300 Database, in: G. Beamson, D. Briggs (Eds.), John Wiley & Sons,U. K.1992, pp. 128.

[182] M. Sakamoto, M. Fujistuka, T. Majima, Light as a construction tool of metal nanoparticles: Synthesis and mechanism, Journal of Photochemistry and Photobiology C: Photochemistry Reviews, 10 (2009) 33-56.

[183] C.-G. Wu, C.-Y. Chen, Chemical deposition of ordered conducting polypyrrole films on modified inorganic substrates, Journal of Materials Chemistry, 7 (1997) 1409-1413.

[184] O. Inganäs, T. Skotheim, I. Lundström, Polypyrrole-semiconductor Schottky barriers, Journal of Applied Physics, 54 (1983) 3636-3639.

[185] J.B. Kim, C.S. Kim, Y.S. Kim, Y.-L. Loo, Oxidation of silver electrodes induces transition from conventional to inverted photovoltaic characteristics in polymer solar cells, Applied Physics Letters, 95 (2009) 183301.

[186] W.A. MacDonald, M.K. Looney, D. MacKerron, R. Eveson, R. Adam, K. Hashimoto, K. Rakos, Latest advances in substrates for flexible electronics, Journal of the Society for Information Display, 15 (2007) 1075-1083.

[187] M.F. Attia, T. Azib, Z. Salmi, A. Singh, P. Decorse, N. Battaglini, H. Lecoq, M. Omastová, A.A. Higazy, A.M. Elshafei, M.M. Hashem, M.M. Chehimi, One-step UV-induced modification of cellulose fabrics by polypyrrole/silver nanocomposite films, Journal of Colloid and Interface Science, 393 (2013) 130-137.

[188] http://www.icdd.com/products/, pdf2.htm.

[189] B. D. Cullity, S.R. Stock, Elements of X-ray diffraction, Prentice-Hall Inc.2001.

[190] L. Dauginet-De Pra, S. Demoustier-Champagne, Investigation of the electronic structure and spectroelectrochemical properties of conductive polymer nanotube arrays, Polymer, 46 (2005) 1583-1594.

[191] A. Joshi, S.A. Gangal, S.K. Gupta, Ammonia sensing properties of polypyrrole thin films at room temperature, Sensors and Actuators B: Chemical, 156 (2011) 938-942.

[192] E. Kriván, C. Visy, R. Dobay, G. Harsányi, O. Berkesi, Irregular Response of the Polypyrrole Films to H2S, Electroanalysis, 12 (2000) 1195-1200.

[193] P. Lobotka, P. Kunzo, E. Kovacova, I. Vavra, Z. Krizanova, V. Smatko, J. Stejskal, E.N. Konyushenko, M. Omastova, Z. Spitalsky, M. Micusik, I. Krupa, Thin polyaniline and polyaniline/carbon nanocomposite films for gas sensing, Thin Solid Films, 519 (2011) 4123-4127.

[194] P. Song, Q. Wang, Z. Yang, Ammonia gas sensor based on PPy/ZnSnO3 nanocomposites, Materials Letters, 65 (2011) 430-432.

[195] J. Jang, J. Bae, Carbon nanofiber/polypyrrole nanocable as toxic gas sensor, Sensors and Actuators B: Chemical, 122 (2007) 7-13.

[196] L. Hong, Y. Li, M. Yang, Fabrication and ammonia gas sensing of palladium/polypyrrole nanocomposite, Sensors and Actuators B: Chemical, 145 (2010) 25-31.

[197] T. Patois, J.-B. Sanchez, F. Berger, J.-Y. Rauch, P. Fievet, B. Lakard, Ammonia gas sensors based on polypyrrole films: Influence of electrodeposition parameters, Sensors and Actuators B: Chemical, 171–172 (2012) 431-439.

[198] S.K. Pandey, K.-H. Kim, K.-T. Tang, A review of sensor-based methods for monitoring hydrogen sulfide, Trends in Analytical Chemistry, 32 (2012) 87-99.

[199] A.L. Briseno, R.J. Tseng, M.M. Ling, E.H.L. Falcao, Y. Yang, F. Wudl, Z. Bao, High-Performance Organic Single-Crystal Transistors on Flexible Substrates, Advanced Materials, 18 (2006) 2320-2324.

[200] H.T. Yi, M.M. Payne, J.E. Anthony, V. Podzorov, Ultra-flexible solution-processed organic field-effect transistors, Nature communications, 3 (2012) 1259.

[201] J. Huang, H. Zhu, Y. Chen, C. Preston, K. Rohrbach, J. Cumings, L. Hu, Highly Transparent and Flexible Nanopaper Transistors, ACS Nano, 7 (2013) 2106-2113.

[202] P. Jha, P. Veerender, S.P. Koiry, V. Saxena, A. Gusain, A.K. Chauhan, D.K. Aswal, S.K. Gupta, Poly(2,7-carbazole) derivative based air stable and flexible organic field effect transistor, AIP Conference Proceedings, 1512 (2013) 772-773.

[203] A. Nigam, G. Schwabegger, M. Ullah, R. Ahmed, I.I. Fishchuk, A. Kadashchuk, C. Simbrunner, H. Sitter, M. Premaratne, V. Ramgopal Rao, Strain induced anisotropic effect on electron mobility in C60 based organic field effect transistors, Applied Physics Letters, 101 (2012) -.

[204] R. Rieger, D. Beckmann, W. Pisula, W. Steffen, M. Kastler, K. Müllen, Rational Optimization of Benzo[2,1-b;3,4-b′]dithiophene-Containing Polymers for Organic Field-Effect Transistors, Advanced Materials, 22 (2010) 83-86.

[205] T. Sekitani, U. Zschieschang, H. Klauk, T. Someya, Flexible organic transistors and circuits with extreme bending stability, Nat. Mater., 9 (2010) 1015-1022.

[206] M. Uno, K. Nakayama, J. Soeda, Y. Hirose, K. Miwa, T. Uemura, A. Nakao, K. Takimiya, J. Takeya, High-Speed Flexible Organic Field-Effect Transistors with a 3D Structure, Advanced Materials, 23 (2011) 3047-3051.

[207] C.-H. Wang, C.-Y. Hsieh, J.-C. Hwang, Flexible Organic Thin-Film Transistors with Silk Fibroin as the Gate Dielectric, Advanced Materials, 23 (2011) 1630-1634.

[208] H. Yan, Z. Chen, Y. Zheng, C. Newman, J.R. Quinn, F. Dötz, M. Kastler, A. Facchetti, A high-mobility electron-transporting polymer for printed transistors, Nature, 457 (2009) 679-686.

[209] W. M. Yun, J. Jang, S. Nam, Y. J. Jeong, L.H. Kim, S. Park, S. J. Seo, C. E. Park, Vacuum thermally evaporated polymeric zinc acrylate as an organic interlayer of organic/inorganic multilayer passivation for flexible organic thin-film transistors, Journal of Materials Chemistry, 22 (2012) 25395-25401.

[210] U. Zschieschang, F. Ante, T. Yamamoto, K. Takimiya, H. Kuwabara, M. Ikeda, T. Sekitani, T. Someya, K. Kern, H. Klauk, Flexible Low-Voltage Organic Transistors and Circuits Based on a High-Mobility Organic Semiconductor with Good Air Stability, Advanced Materials, 22 (2010) 982-985.

[211] M.E. Reish, S. Nam, W. Lee, H.Y. Woo, K.C. Gordon, A Spectroscopic and DFT Study of the Electronic Properties of Carbazole-Based D–A Type Copolymers, The Journal of Physical Chemistry C, 116 (2012) 21255-21266.

[212] M.K. Fung, S.L. Lai, S.W. Tong, S.N. Bao, C.S. Lee, W.W. Wu, M. Inbasekaran, J.J. O'Brien, S.T. Lee, Distinct interfaces of poly (9,9-dioctylfluorene-co-benzothiadiazole) with cesium and calcium as observed by photoemission spectroscopy, Journal of Applied Physics, 94 (2003) 5763-5770.

[213] A. J. J. M. van Breemen, P. T. Herwig, C. H. T. Chlon, J. Sweelssen, H. F. M. Schoo, E. M. Benito, D. M. de Leeuw, C. Tanase, J. Wildeman, P. W. M. Blom, High-Performance Solution-Processable Poly(p-phenylene vinylene)s for Air-Stable Organic Field-Effect Transistors, Advanced Functional Materials, 15 (2005) 872-876.

[214] C.M. Björström, S. Nilsson, A. Bernasik, A. Budkowski, M. Andersson, K.O. Magnusson, E. Moons, Vertical phase separation in spin-coated films of a low bandgap polyfluorene/PCBM blend—Effects of specific substrate interaction, Applied Surface Science, 253 (2007) 3906-3912.

[215] D. G. Castner, K. Hinds, D. W. Grainger, X-ray Photoelectron Spectroscopy Sulfur 2p Study of Organic Thiol and Disulfide Binding Interactions with Gold Surfaces, Langmuir, 12 (1996) 5083-5086.

[216] T. Ishida, M. Hara, I. Kojima, S. Tsuneda, N. Nishida, H. Sasabe, W. Knoll, High Resolution X-ray Photoelectron Spectroscopy Measurements of Octadecanethiol Self-Assembled Monolayers on Au(111), Langmuir, 14 (1998) 2092-2096.

[217] S. Samanta, A. Singh, A.K. Debnath, D.K. Aswal, S.K. Gupta, J.V. Yakhmi, S. Singh, S. Basu, S.K. Deshpande, Oxygen induced hysteretic current-voltage characteristics of iron-phthalocyanine thin films, Journal of Applied Physics, 104 (2008) 073717.

[218] Y. Yun, C. Pearson, M.C. Petty, Pentacene thin film transistors with a poly(methyl methacrylate) gate dielectric: Optimization of device performance, Journal of Applied Physics, 105 (2009) 034508.

[219] Y. -Y. Noh, H. Sirringhaus, Ultra-thin polymer gate dielectrics for top-gate polymer field-effect transistors, Organic Electronics, 10 (2009) 174-180.

[220] D. M. de Leeuw, M.M.J. Simenon, A.R. Brown, R.E.F. Einerhand, Stability of n-type doped conducting polymers and consequences for polymeric microelectronic devices, Synthetic Metals, 87 (1997) 53-59.

[221] P. Cosseddu, G. Tiddia, S. Milita, A. Bonfiglio, Continuous tuning of the mechanical sensitivity of Pentacene OTFTs on flexible substrates: From strain sensors to deformable transistors, Organic Electronics, 14 (2013) 206-211.

[222] P. Veerender, V. Saxena, P. Jha, S.P. Koiry, A. Gusain, S. Samanta, A.K. Chauhan, D.K. Aswal, S.K. Gupta, Free-standing polypyrrole films as substrate-free and Pt-free counter electrodes for quasi-solid dye-sensitized solar cells, Organic Electronics, 13 (2012) 3032-3039.